Computational modelling studies of titanium cluster formation in lithium chloride (LiCl) and titanium tetrachloride (TiCl$_4$)

by

Andile Faith Mazibuko

RESEARCH DISSERTATION

Submitted in fulfilment of the requirements for the degree of

MASTER OF SCIENCE

In

Physics

in the

FACULTY OF SCIENCE AND AGRICULTURE

(School of Physical and Mineral Sciences)

at the

UNIVERSITY OF LIMPOPO

SUPERVISOR   : Prof. H.R. Chauke

CO-SUPERVISOR : Prof. P.E. Ngoepe

2021

Declaration

I declare that the dissertation hereby submitted to the University of Limpopo, for the degree of Master of Science in Physics has not previously been submitted by me for a degree at this or any other university; that it is my work both in design and in execution, and that all material contained herein has been duly acknowledged.

Mazibuko A.F (Ms)

<u>**26 October 2020**</u>

Dedication

In memory of my lovely parents, Anna Mookgo Mabena and Elias Elijah Mazibuko, may their souls continue to rest in peace. To my nephew, for always putting a smile on my face, especially on gloomy days. To my lovely sister and grandmother, for your continued support and advice. Ngiyabonga.

Acknowledgements

I want to thank:

Abstract

Titanium is the most abundant element in the earth's crust and can be produced as both a metal and in powder form. It finds applications in various industries such as in medical and aerospace, where the fabrication of components with excellent corrosion and high-temperature performance are significant. This metal also plays a significant role in the titanium production process due to its desirable physical and chemical properties. However, this process occurs in the presence of alkali metal and alkali earth metal salt mediums. In this study, a combination of computational modelling techniques was employed to investigate the LiCl, TiCl, $TiCl_2$ and $TiCl_4$ systems and their interaction with titanium cluster (Ti_7) at various temperatures. The density functional theory-based codes were used to study the structures and stability, while the classical force-fields codes were employed to study the temperature effect on these systems.

Firstly, the LiCl model was validated using Buckingham interatomic potentials from the Catlow-library, employing the GULP code. The selected potential parameters were able to reproduce the LiCl structure to within 1% in agreement with experimental data. Furthermore, the Ti-Cl and Ti-Li interatomic potential parameters from accurate first-principle calculations describe the interaction of LiCl and Ti_7 cluster. The new interatomic potential parameters were deduced as Ti-Cl: D_e= 0.400, a_0= 1.279, r_0=2.680 and Ti-Li: D_e =0.730, a_0=1.717, r_0=2.000.

Secondly, DL_POLY code was used to characterise both the bulk LiCl and Ti$_7$/LiCl structures employing rigid ion and shell models. It was found that the diffusion coefficient of LiCl was 6.26 nm^2/s, which corresponds to the melting temperature range of 700 K – 800 K for the rigid ion model. This agrees well with the experimental melting temperature range of 877 K – 887 K. The shell model predicts a lower melting temperature range of 600 K – 700 K at a diffusion coefficient of 3.74 nm^2/s, compared to rigid ion model. This behaviour was confirmed by the broadness of peaks on the RDF graphs at this temperature. The RDF graphs for the Ti$_7$/LiCl structure in both rigid ion model and shell model depict a change in the morphology of the system for all interactions as the temperature is increased. It was found that the shell model is preferential for the LiCl structure.

Thirdly, the elastic and mechanical properties of the TiCl, TiCl$_2$ and TiCl$_4$ structures were evaluated. It was found that the TiCl$_2$ and TiCl$_4$ structures are elastically unstable. However, the mechanical properties indicated that TiCl$_2$ and TiCl$_4$ are mechanically stable. The TiCl$_n$ structures, namely TiCl and TiCl$_2$, were evaluated for rigid ion model, to check the transferability of potentials. It was found that the diffusion coefficient of TiCl was 32.02 nm^2/s, which corresponds to a melting temperature of 700 K. The diffusion coefficient for TiCl$_2$ was 115.00 nm^2/s at a melting temperature of 800 K.

Lastly, molecular dynamics calculations carried out on the Ti$_7$/TiCl$_n$ structure showed that an increase in temperature results in the broadening of peaks and a decrease in the peak heights. The entropy and Gibbs formation free energy for LiCl (rigid ion and shell models),

TiCl and TiCl$_2$ (rigid ion model) structures were estimated to determine the influence of temperature on the structures. It was found that the LiCl (shell model) structure is stable at all temperatures and that the TiCl and TiCl$_2$ structures are favoured at lower temperatures (< 500 K). These results provided new insight into understanding the reactions and interactions of titanium clusters with salt mediums in titanium production processes. Moreover, the findings may contribute towards developing alternative ways of titanium production in continuous and less expensive processes.

Table of Contents

List of figures

xiv

List of tables

Chapter 1

Introduction

In this introductory chapter, a concise review is given for titanium metal, titanium clusters, titanium production processes and their drawbacks. We briefly summarise the theoretical and experimental contributions towards titanium production. Lastly, the aim, objectives, and outline of the dissertation are given.

1.1. Rationale

South Africa is the second-largest titanium-bearing mineral producer in the world, accounting to about 22% of global titanium mineral production [1]. The Namakwa Sands mines, Richard's Bay minerals' Tisand (Pty) Ltd and Exxaro's hillendale are three mines in which titanium minerals are recovered. Titanium is applicable in various industries such as in medical and aerospace, where the fabrication of components with excellent corrosion and high-temperature performance are significant [2, 3]. The production of titanium metal in both pure and powder form has received much attention in recent studies due to the useful chemical and physical properties of titanium [4, 5]. For decades, titanium powder production processes relied on reducing agents such as lithium, calcium and sodium alkali metals. The commercial production of titanium metal is reportedly achieved through

various processes such as the Kroll process [6, 7] which involves a reduction of titanium tetrachloride in a molten magnesium chloride salt medium.

According to recent literature, the methods of production for reducing titanium ores to titanium metal incorporate three necessary steps: firstly, using the chlorination process to convert oxide ore to titanium tetrachloride [8]. Secondly, using sodium, magnesium or, on a much smaller scale, electrolysis to reduce titanium tetrachloride to titanium metal. Thirdly, purifying titanium by inert gas sweep, by distillation in a vacuum, or by leaching to remove residual salts and unconsumed reactants [6].

The reaction taking place in the Kroll process, proceeds step-wise by reducing titanium tetrachloride, to titanium trichloride, titanium dichloride, titanium chloride and finally to titanium [6, 7]. However, the reduction reaction occurs extremely fast and results in the production of crystalline particles that tend to aggregate [9]. Furthermore, the formation of pure titanium, by the Kroll process in a medium of molten magnesium chloride results in a batch-wise reduction of titanium tetrachloride due to the low solubility of magnesium [10, 11].

The other process of interest is the lithiothermic process [12], which involves using lithium chloride as a reducing agent in titanium production. Despite limited literature work reported on using lithium chloride salt in the titanium production process; lithium chloride has a few disadvantages such as lithium being highly reactive [13, 14]. Caution must be taken in selecting suitable materials of construction to handle molten lithium. However,

understanding the conditions and mechanism of the reaction process as well as the interaction of lithium chloride with titanium may provide hope for enhanced titanium production [15]. A lithiothermic process is advantageous for titanium production, especially with lithium chloride salt having the lowest melting temperature compared to other salts reported in the literature [13]. This low melting temperature makes it possible to minimise pollution of the titanium metal by the reactor materials and to use a simpler, thus less expensive technology [12]. The lithium chloride salt will also ensure that the operating temperature of titanium production is low since the reduction of titanium tetrachloride is a highly exothermic reaction [16].

In other work, Seon and Nataf [12] reported on the production of titanium powder through the lithiothermic reduction of titanium tetrachloride in a molten salt reactor that uses a high-energy mixer. The high energy mixer serves to disperse gaseous titanium tetrachloride and undissolved lithium into the molten salt. This procedure may also break up any lumps of titanium that might form. In recent experimental studies, the CSIR is testing a lithiothermic step-wise reduction of titanium tetrachloride to titanium as part of the titanium formation process, but the small titanium clusters are thermodynamically unstable [17]. Thus, further investigations on the evolution and growth of these clusters in a molten lithium chloride medium are essential to understand the reaction mechanism of the titanium production processes before performing experiments.

In recent work, there have been attempts to design experiments for maximising titanium production, and this has proved to require more resources and time [14]. In the quest to

address the stated shortcomings, a computational modelling approach has been thought of, which is more robust and cost-effective [17]. Thus, the density functional theory-based and classical molecular dynamics approaches have been used to establish suitable salt medium conditions in the shell and rigid ion models. Also, the molecular dynamics technique employed in the General Utility Lattice Program and DL_POLY is used to calculate the mechanical properties, in particular, the mechanical behaviour of the structures and the thermodynamic properties. Such a multi-approach strategy will enable a deeper understanding on reaction mechanisms in the titanium production process. The investigations were carried out as follows.

Firstly, determine and validate the LiCl salt with respect to the lattice parameters and elastic constants. This was followed by the development and validation of the interatomic potential parameters for the Ti_7/LiCl interactions. The temperature dependence of LiCl salt and Ti_7 cluster in LiCl were calculated. Furthermore, the stability of the cluster was evaluated using the different computational codes such as FHI-aims, CASTEP and DMol^3. FHI-aims code is needed to calculate the ground state energies before fitting of interatomic potential parameters can be carried out.

Secondly, the TiCl, $TiCl_2$ and $TiCl_4$ salt mediums were investigated to understand their structure and elastic stability. Moreover, the temperature dependence of the TiCl and $TiCl_2$ structures was carried out. Thirdly, the Ti_7/$TiCl_n$ temperature dependence was investigated. Lastly, the entropy and Gibbs free energy trend were evaluated for the different structures. This analysis and technique used have provided useful information for

understanding the interactions, phase transitions and trends in free energy of the Ti_7 interaction in Li-Cl and Ti-Cl environment, which is crucial in the titanium production process.

1.2. Aim

The aim of the study is to use computational modelling techniques to investigate the interactions of a stable Ti_7 cluster in the Li-Cl and Ti-Cl salt medium in order to understand the growth of titanium metal.

1.3. Objectives

In this dissertation, we investigate the geometry and evolution of selected titanium clusters with magic/stable numbers using first-principle density functional theory (DFT) [18] and classical molecular dynamics (MD) approach [19]. This study will employ various computational techniques such as FHI-aims [20], GULP [21] and DL_POLY [22, 23] codes.

The objectives of the study are to:

I.   determine and validate the LiCl structure with respect to lattice parameters and elastic constants

II.   develop and validate the interatomic potentials for Ti_7/LiCl (Ti-Li and Ti-Cl)

III. investigate the thermodynamic properties of LiCl (rigid ion model and shell model)

IV.   determine the temperature dependence of Ti_7 nanocluster in LiCl (rigid ion model and shell model)

V.   evaluate the thermodynamic properties for TiCl and $TiCl_2$

VI.   investigate the temperature dependence of Ti_7 nanocluster in TiCl and $TiCl_2$ salt mediums

VII.   evaluate the thermodynamic properties, i.e. Gibbs free energy and entropy change in different salt mediums

VIII.   investigate the mechanical stability of TiCl, $TiCl_2$ and $TiCl_4$

1.4. Outline of the study

The dissertation is presented in the following manner:

In Chapter 1, we have given a brief introduction on the titanium metal, titanium clusters and the titanium production process. A brief background on the previous studies reflecting the Kroll and lithiothermic processes is presented. Furthermore, the aim and objectives of the study were given.

Chapter 2 gives the literature review of titanium, titanium clusters and the titanium production process. A summary of the importance of titanium and its properties, and what has been done previously in both computational and experimental techniques are presented.

Chapter 3 focuses on the details of the two computational techniques that are employed in the current study. Firstly, the Perdew-Burke-Ernzerhof revised for solids general gradient approximation (GGA-PBEsol) within density functional theory (DFT) is discussed for predicting ground-state properties and the electronic structure. Secondly, the classical molecular dynamics (MD) technique is used in analysing the trajectory of atoms in molecules and giving the dynamics of the molecules. The various computational codes, such as the Fritz Haber Institute ab initio molecular simulation (FHI-aims), CASTEP, DMol^3, General Utility Lattice Program (GULP) and DL_POLY, are presented.

Chapter 4 gives DFT results on modelling of the LiCl structure. The lattice parameters and elastic properties are discussed for validating the model to confirm whether the selected interatomic potential parameters reproduced the LiCl structure.

Chapter 5 predicts the thermodynamic behaviour of the LiCl and Ti_7/LiCl structures. The diffusion coefficients and radial distribution functions of the structures are calculated, and the phase change derived from total energy graphs computed using the molecular dynamics method.

Chapter 6 gives the MD results on the modelling of the TiCl, $TiCl_2$ and $TiCl_4$ structures. The lattice parameters, bond lengths, elastic properties and mechanical stability are discussed, and the diffusion coefficient and radial distribution functions for the TiCl, $TiCl_2$ and $Ti_7/TiCl_n$ (n=1,2) systems are calculated. The phase stability of the $TiCl_n$ structures is derived from

the total energy graph. Lastly, the entropy and Gibbs free energy are investigated for the

LiCl (rigid ion and shell models), TiCl and $TiCl_2$ structures (rigid ion model).

Chapter 7 presents the summary and conclusion of the work as well as future research

recommended to follow the efforts described in this dissertation.

Chapter 2

Overview of titanium production processes

This chapter is concerned with the literature review with regard to the titanium production processes, intermediates/precursors in titanium production, reducing agents, the different metal clusters and background information on the properties to be investigated. We begin by reviewing the production of Ti metal and Ti powder.

2.1. Titanium production

Titanium production proceeds in stages such as the extraction of Ti from its ore, Ti processing and manufacturing. These stages of titanium production are reportedly difficult and attribute to the high cost associated with titanium production [24]. Ti production is significant because, over the years, titanium applications have been limited to where high-temperature performance is required [2].

Production of titanium includes thermochemical processes and electrolytic winning processes. Thermochemical processes involve the reduction of a precursor ($TiCl_4$ and TiO_2) with a reductant, which is either sodium chloride (in a sodiothermic reduction process) or magnesium chloride (in a magnesiothermic reduction process) [25]. In the other study it was indicated that electrolytic winning process uses a fused salt electrolyte

to leach Ti metal from its ores [6]. It was also revealed that commercial production of Ti metal is usually carried out through the magnesiothermic and sodiothermic reduction processes [14]. The product of both processes is the Ti sponge, which is a standard Ti primary metal that is commercially available for melting and manufacturing.

White and Oden [26] patented a molten salt process to produce titanium powder by sodiothermic reduction of $TiCl_4$. In this process, sodium is dissolved in molten NaCl, mixed, reacted with dissolved $TiCl_2$ and then dissolved in a separate stream of molten NaCl. The splitting of the titanium powder slurry results in the observation of three streams [14, 26]. This approach is suitable for processes that involve using a metal as a reductant also known as metallothermic reduction processes, where the reducing metal has a relatively high solubility in the corresponding metal chloride such as sodiothermic (NaCl) and calciothermic ($CaCl_2$) reduction of $TiCl_4$ [14]. However, it is unsuitable for a magnesiothermic reduction of $TiCl_4$ because of the solubility of magnesium in molten $MgCl_2$.

Winter [27] patented an invention to reduce $TiCl_4$ continuously with molten magnesium which floats on top of a bath of stirred molten salt. The molten magnesium is contained in the vortex and does not contact any part of the stirrer or reactor walls [14]. It was decided not to pursue this solution as it is not robust enough for industrial processing. Furthermore, such a process offers little freedom to make changes to the processing conditions through which to manage titanium particle growth, since the $TiCl_4$ gas is in direct contact with a large mass of molten reducing metal [14, 27].

2.1.1. Magnesiothermic reduction process

The magnesiothermic reduction process also known as the Kroll process is a dominant process used in the industry in the production of titanium sponge metal whereby the gas-liquid reduction reaction is used to introduce the TiCl₄ gas and the TiCl₄ gas is reacted with molten magnesium chloride [28]. This process has some limitations that include the production of titanium in batches, which is not ideal for commercial use, thus making it costly and resulting in low titanium quantity production [29, 30]. Intensive research into new techniques is being developed to overcome the shortcomings in the Kroll process [7, 14]. One such effort pursued in industrial processing is the Fray-Farthing-Chen process [31].

The Fray-Farthing-Chen process is a method that was discovered in 1997 at the University of Cambridge for the electrochemical deoxidation of metal oxides in molten salt [32]. The overall reaction in this process is

$$TiCl_2 - MgCl_2(l) + Mg(l) = Ti\ (s) + 2MgCl_2(l). \tag{2-1}$$
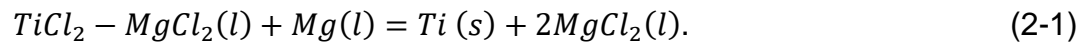
This reaction means that the molten state of the mixed salt is a reaction intermediate in this process and synthesis is by reacting solid sponge titanium seed positioned in the molten MgCl₂ with incoming TiCl₄ gas. The synthesis described above is as follows:

$$Ti\ (s) + MgCl_2(l) + TiCl_4(g) = TiCl_2 - MgCl_2(l). \tag{2-2}$$
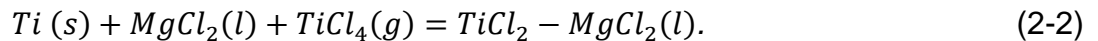
Titanium metal production follows reaction (2-1) through which there is a magnesium reduction reaction of the mixed salt in a molten state [7]. A conspicuous feature of this

reaction arrangement is that, compared to the complex Kroll process, the reduction is a more straightforward liquid-liquid reaction [33]. In this case, the reduction reaction takes place in a bulk region, which in turn, incorporates more significant reaction regions and space with a fast and controllable reaction, less localised heat burden, and homogeneous heat evolution.

The titanium metal product is powdery in appearance and nature, and forms along with the reactor shape. However, the titanium product shape, location and morphology are influenced by experimental conditions such as the reactor material, mixing mode, and $TiCl_2$ concentration [32]. It was observed that the macroscopic shape and the microscopic morphology of the titanium product depend on the temperature of the reduction process and that the titanium metal produced is suitable for the metal powder product application, and melted product application.

2.1.2. Sodiothermic reduction process

The sodiothermic reduction process, also known as the Hunter process, involves the reduction of $TiCl_4$ in molten NaCl. This is a two-step process consisting of a first step that is continuous with a low operating temperature and materials of construction for the equipment offer fewer problems [6]. The production of both Ti powder and Ti sponge is through this process [2]. Hunter was the first to develop the sodium reduction process, and the following reaction describes it:

$$TiCl_4(g) + 4Na(l) \rightarrow 4NaCl\ (l,s) + Ti\ (s)\ . \tag{2-3}$$
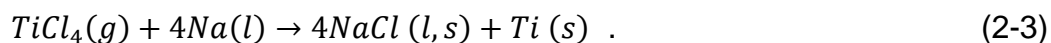
However, there are steps which occur simultaneously and sometimes competitively, as follows:

$$TiCl_4(g) + 2Na(l) \rightarrow TiCl_2\ (l) + 2NaCl\ (s), \tag{2-4}$$

$$TiCl_2(l) + 2Na(l) \rightarrow Ti\ (s) + 2NaCl\ (s,l), \tag{2-5}$$

$$Ti\ (s) + TiCl_4(g) \rightarrow 2TiCl_2\ (l). \tag{2-6}$$
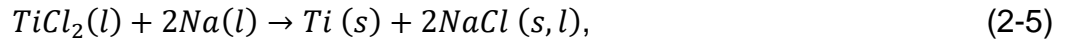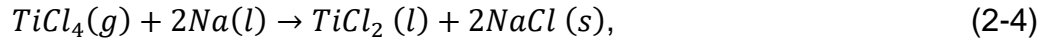
At near stoichiometric (at about 232°C), portions of TiCl4 and sodium are introduced to form the reaction in (2-4). Due to positive pressure and the agitation of inert gas, the TiCl2 and NaCl product mixture is free flowing at this temperature. Moreover, heating the product in the air results in drying. However, due to a large portion of reactive fines, using a centrifuge to remove the bulk of the liquid followed by vacuum drying results in product drying.

In other work, Zhang *et al.* [34] reported on the thermodynamic calculation of the self-diffusion of NaCl using the pressure-volume-temperature equation of state. It was reported that the self-diffusion coefficients of Na and Cl can be successfully reproduced in terms of bulk elastic and expansivity data. Furthermore, it was found that self-diffusion coefficients in NaCl are separately reproduced at low and high temperature ranges. More importantly, the formation of a "knee" behaviour was attributed to the presence of a "frozen equilibrium" at low temperatures. Their findings were also similar to previous experimental data, where the "knee" behaviour was also observed [35].

2.1.3. The electrolytic winning of titanium

Titanium can also be produced through electrowinning in the fused salt electrolyte [6]. The process occurs in two distinct steps described by the following cathodic reactions:

$$Ti^{+4} + 2e^- \rightarrow Ti^{+2} \tag{2-7}$$

$$Ti^{+2} + 2e^- \rightarrow Ti^0 \tag{2-8}$$

The anodic reaction is: $2Cl^- \rightarrow Cl_2(g) + 2e^-$ (2-9)

Reactions (2-7) and (2-8) are cathodic reactions that are carried out in a single cathode volume surrounded by a diaphragm, with the anodes outside. Electrolytic reduction of tetrachloride occurs at the dichloride generator, where the reduction of tetrachloride results in the production of titanium dichloride ($TiCl_2$), which is soluble in the molten salt electrolyte (catholyte). $TiCl_2$ is then further reduced to titanium, as in reaction (2-8). The reaction in (2-8) occurs at a second cathode, where titanium attaches for later harvesting by batch or semi-continuous schemes [36]. Furthermore, the harvested crystal, containing residuals of the electrolyte salts from all electrowinning processes, is leached, washed, and then dried.

One advantage of electrowinning processes for titanium reduction is that there is no need for an association with a source of sodium or magnesium. Electrowinning processes are inherently more straightforward than sodium or magnesium reduction practices and generally, are capable of producing higher-quality titanium [6, 7]. The aim of these investigations is at developing production methods that are continuous, so as to lower the production cost of titanium metal and improve its energy efficiency. Comparisons between

these processes show that the Kroll process has low residual volatiles and good titanium quality [7].

2.2. Alkali metals and alkali earth metals

There are a few alkali metals/alkali earth metals that can be used to reduce the $TiCl_4$ or TiO_2 precursors in titanium production. These include Mg, Na, Ca, Li, H_2 (although it is not part of the alkali metals group) and Al, which is a post-transition metal.

2.2.1. Hydrogen and aluminium

Hydrogen is a low costing reducing agent compared to other agents listed above; however, it is not an ideal medium for titanium production because it has low conversions which result in the need for unconverted precursor recycle loops and abundant hydrogen [13]. On the other hand, aluminium has been used in different investigations to reduce $TiCl_4$ and TiO_2 [37]. However, aluminium forms alloys with titanium and therefore, it is difficult to prevent contamination of the Ti product. Instead of recycling the aluminium-containing by-product, it would preferably be more economical to sell it [13, 37]. Selling as a new product can generate extra revenue however, the disadvantage is that the volume of a by-product sold sets the output of the titanium production plant.

2.2.2. Magnesium chloride

Magnesium chloride (and magnesium which is virtually insoluble in Ti) is currently the preferred choice of reducing agent in the titanium production industry and is used in the Kroll process [13, 24]. The reasons being that Mg is cheaper compared to Na, Ca, Li, and it is significantly less reactive than Na, Ca, or Li. Magnesium requires less energy to produce, and it can be handled safely in the solid-state without expensive or special precautions. In the Kroll process, there is a division of the anhydrous form of the bulk $MgCl_2$ by-product, by merely draining and tapping it from the sponge product [13].

2.2.3. Sodium chloride

Sodium chloride and sodium have been used to commercially produce titanium in the Hunter and similar processes for several reasons, which include the maturity of the production technology [30]. van Vuuren [13] has also noted that the production of Na and Cl_2 is through the electrolytic cells directly recycled from anhydrous NaCl, and it is virtually insoluble. Sodium has a higher vapour pressure at the reaction conditions of the Hunter process and can be highly dangerous [13, 30]. NaCl has the highest melting temperature than for all suitable alkali metal and alkaline earth metal chlorides (801°C).

2.2.4. Calcium chloride

Calcium chloride and Calcium have several properties that make them advantageous in some processes. These include the boiling point of $CaCl_2$ being higher than the reported melting temperature of Ti (1668°C), making it possible to melt and extrude a titanium ingot directly out of $CaCl_2$. Ca is nearly twice as expensive as Mg and virtually insoluble in Ti [13]. The melting temperature of Ca is relatively high (842°C), and this results in the operating temperatures of processes that involve these substances to be relatively high (>800°C).

2.2.5. Lithium chloride

Lithium chloride is an ionic compound characterised by high ionic conductivity and a low melting temperature [38, 39, 40]. Like other salts, the usage of this salt has limitations which include its sensitivity to moisture and easy absorption of water in the humid atmosphere. The morphological and structural analysis of lithium chloride using XRD analysis shows that LiCl has a minor amount of monohydrate $LiCl.H_2O$, which means that the salt is strongly prone to absorb, retain water and become increasingly sticky [40]. A thermo-analytical analysis of LiCl under ambient air using a DSC curve showed that heating LiCl under ambient air and argon produces identical curves. This means that it is possible to replace an inert gas atmosphere with an air atmosphere in processes such as those employing molten LiCl at elevated temperatures. Commercially available chlorides such as LiCl contain impurities such as trace amounts of oxides [41, 42].

2.3. Structures of LiCl and Ti

2.3.1. LiCl structure

The lithium chloride structure has a space group of Fm-3m, with space group number 225, and it has a cubic crystal system. The crystal structure of titanium is characterised by unit cell parameter of a = b= c = 5.070 Å [43] with α = β = γ = 90.000°. Table 2.1. shows the physical properties of LiCl. Lithium chloride is a colourless crystal or powder with low toxicity. It may become corrosive upon contact with water or moist surfaces and very soluble in water and alcohols.

Table 2.1. Physical properties of lithium chloride (LiCl).

Properties	Value
Melting temperature	605-614 °C
Boiling temperature	1382 °C
Coordination geometry	Octahedral
Molecular shape	Linear (gas)

2.3.2. Titanium

Titanium has a hexagonal closed packed (hcp) structure with a space group of P63/mmc and a space group number of 194. Table 2.2 shows the physical properties of Ti. The crystal structure of titanium is characterised by a unit cell parameter of a = b= 2.951 Å, c =

4.686 Å with α = β = 90.000° and γ = 120.000°. Titanium can be recrystallised into various crystal structures, although each transformation is only stable within certain temperature ranges [44]. This transformation temperature depends on the purity of the metal. Pure titanium and most of the titanium alloys crystallise at low temperatures to α-titanium also referred to as a hexagonal close-packed structure. However, at high temperature, the body-centred cubic structure, referred to as β-titanium, is stable. The transformation temperature for pure titanium to β-titanium is 882 °C. Generally, titanium metal does not merge with oxygen at room temperature and is unreactive. It also resists attack by chlorine, acids, and other corrosive agents. Nonetheless, at high temperatures, titanium becomes more reactive and can catch fire when heated in the presence of oxygen. In Figure 2.1, we show the crystal structures of lithium chloride and titanium.

Table 2.2. Physical properties of titanium metal (Ti).

Properties	Value
Melting temperature	1668 °C
Boiling temperature	3287 °C
Number of isotopes	18; 5 are stable
Most common isotopes	46Ti, 47Ti, 48Ti, 49Ti and 50Ti
Key isotopes	48Ti
Phase room temperature	20°C /Solid
Bulk modulus	110 GPa
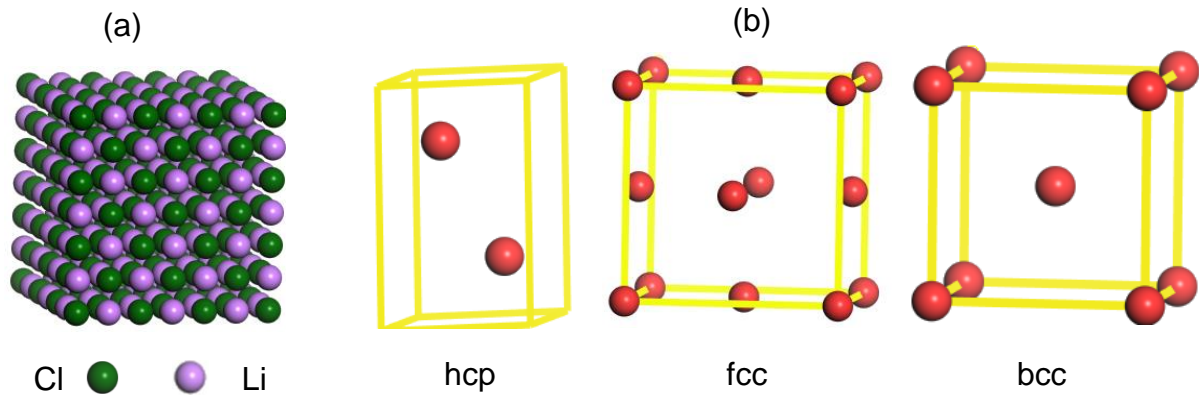
Figure 2.1. The crystal structure of (a) lithium chloride, (b) titanium hexagonal closed packed (hcp), face-centred cubic (fcc) and body-centred cubic (bcc).

2.4. Precursors/intermediates in Ti production process

2.4.1. Titanium dioxide

Titanium is extracted from its rutile (TiO_2) ore [28]. Titanium dioxide (TiO_2) occurs as a white powder with exceptional hiding power and exhibits three polymorphs, i.e. rutile, anatase and brookite [45]. This hiding power property stated gives reason for the meaningful usage of titanium dioxide in paint, as a catalyst in industrial operations and ceramics [46]. The two commercial processes used for TiO_2 pigment production are sulphate and chloride processes [46, 47]. The chloride process is the frequently used process since it generates superior pigment with considerably fewer wastes [47].

2.4.2. Titanium tetrachloride

The titanium tetrachloride ($TiCl_4$) intermediate is produced from the chlorination of Ti slag. This intermediate vaporises at moderate temperatures, but it is a liquid at atmospheric pressure and room temperature [2]. $TiCl_4$ is an intermediate used in the titanium sponge and TiO_2 pigment production [48, 49, 50]. The reactions between $TiCl_4$ and the reducing agents (NaCl or $MgCl_2$) can occur directly when $TiCl_4$ or any titanium sub-chlorides present encounter a suspended or dissolved reducing agent. Similarly, the reaction can also occur indirectly along an electronically mediated mechanism, without any physical contact between the reacting species [14].

2.4.3. Titanium sub-chlorides

2.4.3.1. Titanium trichloride and titanium dichloride

In the Kroll process, the reduction of $TiCl_4$ by reacting $TiCl_4$ with $MgCl_2$ or titanium scraps results in titanium subchlorides, either titanium trichloride ($TiCl_3$) or titanium dichloride ($TiCl_2$) [8, 16]. The generated titanium subchloride is then later augmented in molten $MgCl_2$. After the reaction, the excess magnesium and by-product $MgCl_2$ are removed and recovered by draining and vacuum distillation [16, 28]. The acquired titanium can be directly melted without crushing and can be cast into an ingot since the product is, in principle, oxygen and iron-free titanium.

2.5. The metal clusters of various transition metals.

In this section, we review titanium clusters and provide a brief overview of other transition metal clusters. Transition metal clusters have attracted a lot of attention globally. Several studies on transition metal clusters, such as Pd and Ti have been carried out [51, 52]. These studies report that properties of small metal clusters may significantly differ from those of the bulk. However, they can emulate the behaviour of either the metal particle or crystal defects in supported crystals [52]. An increment in the cluster size results in the gradual evolution of properties towards the bulk structure and creates new prospects for sustainable materials [53].

2.5.1. Titanium clusters

Titanium clusters have shown great potential since they exhibit different properties compared to that of bulk structure such as the dependence of the internal energy to the cluster size, which dictates their growth patterns and geometrical arrangement. These properties have prompted a great interest in this field, and thus, extensive studies on Ti clusters are being performed [54]. Titanium clusters form a fundamental point in understanding the electronic structure and geometry of the bulk Ti structure and small titanium clusters are reported to elucidate bulk-like electronic structures. DFT investigations performed by Zhao *et al.* [55] on Ti clusters to research their electronic and structural properties, showed that Ti clusters follow a pentagonal growth behaviour that favours close-packed structures. Sun *et al.* [56] reported on the icosahedral, octahedral-,

and tetrahedral- sequences being some of the size-dependent growth patterns. These structures or geometries can be attained by either adding or removing atoms from specific basic motif or positions. It was also reported that the *n* clusters with 7, 13 and 15 atoms are magic numbers or stable clusters, with unique configurational geometries.

A comparative study was carried out on Ti_n (n =13-19) clusters using PBE level of theory with PAW [57]. The distorted icosahedral was found to be the lowest geometry for Ti_{13}, and they also reported that distortions evolve with an increase in cluster size, where there is an addition of atoms onto the cluster surface [18]. Similarly, the shell effect of 3d electrons has been found to play a vital role in the formation of directional bonds. Medina *et al.* [58] reported on using DFT and applying two diverse exchange-correlation functionals (PBE and BLYP) to study the structural, magnetic and energetic properties of small Ti clusters. It was observed that the calculated bond lengths and binding energies show that properties of titanium clusters up to 13 atoms are notably different from bulk properties [52, 58]. The distorted icosahedral Ti_{13} was found to be the lowest energy isomer.

In other work, BPW/DNP calculations performed to investigate the structural stability of neutral and single charged icosahedral Ti_{13} clusters, suggest that the D_{3d} symmetry is favoured by the Ti_{13}, Ti_{13}^{-1}, and Ti_{13}^{+1} clusters as a result of Jahn-Teller distortions [59]. The small distortions from the icosahedral geometry are found to be comparable with experimental results [18]. Furthermore, the weak magnetism in icosahedral Ti_{13}, Ti_{19}, fcc $Ti_{43,}$ and quenched magnetic moments in icosahedral Ti_{55} are due to strong s, p-d hybridisation states in all the Ti clusters [18, 60].

Previous experimental studies reveal an observation of sharp spectral features to about n=8, beyond that, the spectral features appear to congest to a broad feature near the Fermi level [61]. The width of the spectral features increases with an increase in cluster size, which indicates that the electronics of the titanium clusters appear to behave bulk-like at slightly smaller sizes [62]. Moreover, the experiments reveal a clear correlation between the chemical reactivity and electronic structure and provide essential information about the electronic structure of the clusters. However, part of the interest in this field emanates from the complex interplay of opposing forces that are at work in the complex electron system. On the other hand, d-orbitals contribute to bond strength [61, 62].

The effect lessens as one moves from left to right across a periodic table since the radial size of the *d* orbital is notably significantly relative to the radial size of the *s*-orbitals [60]. There is an energetic price often paid to promote essential atoms to an electron configuration that diabatically correlates to the ground state molecules [60, 62]. The energy from the promotion of atoms may weaken the adiabatic bond energy relative to the diabatic bond energy. Additionally, the usual laser vaporisation in a flow system and cluster generation experimental techniques are associated with many control variables (gas transport pressure, cluster concentration, internal and source temperature) [63]. Also, cluster growth is a very complex process where the coexistence of diverse isomers is possible.

2.5.2. Other transition metal clusters

In the past two decades, 4d transition metal clusters were extensively studied for their applications in the development of new heterogeneous catalysts and magnetic properties [64]. Most popular theoretical and experimental investigations were carried out on metal clusters such as Ag, Ru, Rh, Pd and discrete variation local spin density functional method calculations performed on M_{13} (M = Y, Zr, Nb, Mo, Tc) clusters of possible three high-symmetry (O_h, I_h, D_{3h}) to explore their magnetic properties [65]. The studies reported that the preferred configuration for Mo_{13} and Tc_{13} is the cuboctahedra (O_h) structure, and for all other 13 atom metal clusters studied; the icosahedral configuration is the most stable. Moreover, the magnetic moments of all clusters with the lowest energy geometries were found not to be significant, and these geometries are reported to be magnetic [64, 65].

Kumar and Kawazoe reported on calculations carried out on the electronic structure of Nb_n clusters consisting of up to 23 atoms using a plane-wave basis and GGA exchange-correlation functional [66]. A distorted body centred cubic structure was observed for n = 15 and all other clusters n > 13; also, high coordination structures with hexagonal antiprism were observed. The magic numbers (stable configuration) n = 10, 12, and 16 showed that HOMO-LUMO gaps were more significant [18].

Molina *et al.* [67] performed energy minimisation investigations using a plane-wave basis and the PZ exchange-correlation functional on Pb_n (n=3-14), and they reported that icosahedral-like packing scheme was favoured for the ground state geometry growth of

the more massive clusters beginning from n = 7. The highest HOMO-LUMO gaps were observed for Pb_{10} and Pb_{13}, suggesting that in the experimental mass spectra, the abundance of the Pb_{10} and Pb_{13} clusters is an electronic effect.

DFT investigations carried out on Pb_n clusters using BLYP/DND level of theory by Wang *et al.* [68] report on the prediction that for Pb_{12} and Pb_{13} the closed packed icosahedral structures are not the lowest geometries. However, the lowest geometries are a strongly distorted icosahedral cage and face capped icosahedral cage, respectively. In this investigation, the HOMO-LUMO gaps gave an indication that the clusters with n = 10, 12, 16, 18 and 21 configurations have high stability compared to their neighbours [18, 68].

2.6. Computational details

The usage of computational simulation techniques is critical to understand the physical and chemical properties of materials [69]. In this study, the fritz haber institute ab initio molecular simulation (FHI-aims) code with the general utility lattice program (GULP) capable of generating interactions of the titanium cluster (Ti_7) with LiCl, will be employed. Moreover, DL_POLY [22], CASTEP [70, 71] and $DMol^3$ [72, 73] codes will be used to study the temperature dependence of stable Ti_7 cluster in the salt mediums and the stability of the cluster. These techniques are essential for investigating the geometry and thermodynamic properties of Ti nanoclusters in salts.

2.6.1. Properties to be investigated

2.6.1.1. Binding energy

The binding energy is one of the properties investigated and discussed. It is defined as the amount of energy that is required in dispersing all particles in a system or separating a particle from a system [52]. This energy applies to electrons bound to nuclei atoms, ions bound together in crystals and also subatomic particles in atomic nuclei.

2.6.1.2. Relative stability

The cluster stability can be discussed based on the average binding energies and second-order difference energy [74]. It has turned into a norm for calculations of the electronic structure of varying difficulty, to yield the total energy of a solid [75]. The total energy of a solid offers a possibility of estimating stabilities of structures that are either inaccessible experimentally or unavailable and this, in turn, has implications for making predictions on structural stability. More importantly, the binding energy and relative stability from DFT calculations have been used successfully to predict the structural stability of solid solutions and alloys [69].

2.6.1.3. Bond length and coordination

The bond length is the distance between the nuclei of two atoms that are bonded or the distance where the energy of a system is minimum [76]. A bond length is related to the size of atoms and follows the same trend as the atomic radii in the periodic table, i.e. decreasing down a group. Information regarding bond length can sometimes give clues as to the type of bonding present in a molecule. In simpler terms, the relative metal ion size, the ligands and electronic factors such as charge (which is dependent on the electronic configuration of the metal ion) influence the coordination number of a complex [77, 78].

Chapter 3

Methodology

This chapter introduces and describes various computational methods employed in this dissertation. The current work is based on density functional theory (DFT) [79, 80, 81] employing FHI-aims code [20], and molecular dynamics (MD) [19, 82] using the GULP [21] and DL_POLY [22, 23] codes. In this work, the GULP code is required to calculate lattice parameters for LiCl, TiCl, $TiCl_2$ and $TiCl_4$ based on the compatibility of interatomic potentials available in the literature. These are achieved by performing a full geometry optimisation of the structure through energy minimisation. The FHI-aims code is used to effectively investigate the total ground state energies of Li-Ti and Ti-Cl interactions to be used in deriving empirical potential parameters. Their potential parameters are then validated using GULP code through a least-square fitting. The DL_POLY code is required to calculate thermodynamic properties of the LiCl, TiCl and $TiCl_2$ structures, such as diffusion coefficients. Furthermore, the results of the DL_POLY calculations will be used as input to the CASTEP and $DMol^3$ calculations for checking and validating the stability of the Ti_7 cluster. We will indicate which method was used to deduce various properties in a given section. Firstly, we begin by discussing the density functional theory, which allows the prediction of the ground state energy of many-body systems, in the next section.

3.1. Density functional theory

In 1951, Slater used ideas from the electron gas with the purpose to abbreviate the Hartree-Fock theory such that electronic structure calculations on solids became achievable [83]. It is reported that in solid-state structures, molecules and atoms the electron density (ρ) is a scalar function defined at each point r in real space and is written as,

$$\rho = \rho(r). \tag{3-1}$$

This was adopted by Hohenberg and Kohn in 1964 [80] and Kohn and Sham in 1965 [81], and describes the ground state energy of many-electron systems as a functional of the electron density $\rho(r)$,

$$E = E[\rho(r)]. \tag{3-2}$$

This resulted in Kohn and Sham [81] deriving a one-electron Schrödinger equation by first expressing the functional as a sum of two terms, written as

$$E[\rho] = T_o[\rho] + U[\rho], \tag{3-3}$$

where $T_o[\rho]$ is the kinetic energy of non-interacting electrons and $U[\rho]$ is the coulomb energy which is purely classical consisting of electrostatic energy arising from the coulomb attraction between electrons and nuclei, the repulsion between all electronic charges and the repulsion between nuclei, which can be written as,

$$U[\rho] = U_{en}[\rho] + U_{ee}[\rho] + U_{ion-ion}. \tag{3-4}$$

The Hohenberg-Kohn-Sham theorem [84, 85], which is a central part of density functional theory, states that the total energy is at its minimum value for the ground state density and that the total energy is stationary with respect to first-order variations in the density, i.e.

$$\left.\frac{\partial E[\rho]}{\partial \rho}\right|_{\rho=\rho_0} = 0. \qquad (3\text{-}5)$$

In conjunction with the kinetic energy, one-particle wave-functions $\varphi_i(r)$ were introduced, which generate the electron density

$$\rho(r) = \sum_i n_i |\varphi_i(r)|^2, \qquad (3\text{-}6)$$

where n_i signifies the occupation number of the eigenstate i, which is signified by the one-particle wave function φ_i. Thus, by construction, $\rho(r)$ in the above equation is the exact many-body electron density.

A set of wave functions which reduce the Kohn-Sham energy functional is given by the equation:

$$\left[-\frac{\hbar^2}{2m}\nabla^2 + V_{ion}(r) + V_H(r) + V_{XC}(r)\right]\varphi_i(r) = \varepsilon_i\varphi_i(r), \qquad (3\text{-}7)$$

where φ_i is the wave function of electronic state i, ε_i is the Kohn-Sham eigenvalue, V_{XC} is the exchange-correlation functional which accounts for all other complicated electronic contributions to the total energy [81]. V_{ion} is the static total electron-ion potential and V_H is the Hartree potential of the electron written as,

$$V_H(r) = e^2 \int \frac{\rho(r')}{|r-r'|} dr'. \qquad (3\text{-}8)$$

The relation of the exchange-correlation potential to the exchange-correlation energy is written as,

$$V_{XC}(r) = \frac{\partial E_{XC}[\rho(r)]}{\partial \rho(r)}. \tag{3-9}$$

Moreover, it is formally exact because it does not contain any approximations to the complete many-body interactions. Consequently, following this discussion, the Kohn-Sham total energy functional can be written as,

$$E = 2\sum_{occ} \varepsilon_i + U_{nm} - \frac{e^2}{2} \iint \frac{\rho(r)\rho(r')}{|r-r'|} \, dr dr' + E_{XC}[\rho(r)] - \int \rho(r)V_{XC} dr. \tag{3-10}$$

Approximation methods used in DFT include the local density approximation (LDA) and generalized gradient approximation (GGA), discussed in the next section.

3.2. Approximation methods

3.2.1. Local density approximation

Local density approximation (LDA) forms the basis of all approximate exchange-correlation functionals [79]. It assumes that the exchange-correlation energy at a point r is merely equal to the exchange-correlation energy of a uniform gas that has the same density at a point r [79, 81]. In a homogeneous electron gas of density $\rho(r)$ the exchange-correlation energy is taken from the known results of the many-electron system, and the exchange-correlation energy of the whole molecule or solid is the integral over the contributions per volume element [81].

The LDA functional depends only on the density at a given point, and it can be expressed as:

$$E^{LDA}{}_{XC}(\rho) = \int \rho(r)\varepsilon_{XC}(\rho(r))dr, \qquad (3\text{-}11)$$

where

$$\varepsilon_{XC}(\rho(r)) = \varepsilon_X(\rho(r)) + \varepsilon_c(\rho(r)) \qquad (3\text{-}12)$$

and

$$\varepsilon_X(\rho(r)) = -\frac{3}{4}\left(\frac{3\rho(r)}{\pi}\right)^{\frac{1}{3}} \qquad (3\text{-}13)$$

is the Dirac-Slater exchange energy of the electron gas. LDA is useful in the construction of a more sophisticated approximation to the exchange-correlation energy. The LDA approximation is reported to underestimate the equilibrium cell parameters by 1-2% [86].

3.2.2. Generalized gradient approximation

There are two principal variants of the generalized gradient approximation (GGA): the parameter-free (parameters are determined from known coefficients) and empirical (parameters determined from fits to experimental data or calculated atomic properties) [79]. The parameter-free GGA functionals commonly used in physics are the Perdew, Burke and Ernzerhof (PBE) [87] and Perdew-Wang from 1991 (PW91) [88]. GGA is an improvement over LDA but still not necessarily very accurate; one reason is that the exchange potential does not necessarily have the correct qualitative behaviour. Symbolically this can be written as:

$$E_{XC}^{GGA}[\rho(\boldsymbol{r})] = \int d^3\boldsymbol{r}\rho(\boldsymbol{r})\varepsilon_{XC}{}^{GGA}[\rho(\boldsymbol{r}), \|\nabla\rho(\boldsymbol{r})\|], \qquad (3\text{-}14)$$

ε_{XC} is the exchange-correlation energy and ∇ is the gradient term. The use of GGA has little influence on local properties and tends to overestimate the bond lengths and cell parameters by about 1% but does usually lead to a significant improvement in global changes in the total energy, such as those that result when two atoms combine to make a molecule [79]. GGA includes only the electron density and the gradient of electron density in the exchange-correlation functional and not only on its value at each point in space.

The commonly known functional of GGA is the Perdew-Burke-Ernzerhof (PBE) version [87] of the generalized gradient approximation (GGA). It employs both the density and its gradient at each point in space. Popular GGAs represent a well-tempered balance between numerical accuracy, computational efficiency and reliability, but PBE also juggles the demands of quantum chemistry and solid-state physics [89].

In practice, the exchange-correlation energy or the exchange-correlation potential is unknown [81]. The only way to solve the problem is by way of approximation methods. DFT has been highly successful in describing many classes of systems using approximate functionals such as LDA, GGA, meta-GGA and hybrids to give reasonably accurate results. In this work, we use the GGA functional and the PBEsol [90] form of GGA in the FHI-aims code, since it provides accurate results for the interactions in the Ti_7/LiCl systems we are interested in. PBEsol is a revised form of the Perdew-Burke-Ernzerhof GGA functional that is designed to be more accurate than the original PBE formulation which underestimates surface energies for solids [91]. GGA-PBEsol yields highly accurate bulk exchange energies of metals within the pseudopotential approximation. The functional improves the

starting point for more advanced functional construction. It gives good accuracy for both surface exchange and XC energies. PBEsol minimises reliance on error cancellation between X and C.

3.3. Plane-wave pseudopotential method

Plane-wave pseudopotentials are fundamental methods used to solve one-electron Kohn-Sham equations [81]. These methods are dominant in calculations of the electronic structure in condensed matter physics, material science and provide an excellent balance between computational efficiency and accuracy [92]. The plane-wave pseudopotential technique involves replacing the ionic core electrons and the strong, attractive coulomb potentials binding them to the nuclei, by a weaker pseudopotential that describes features of valence electrons moving through a crystal [93, 94]. It is generally understood that inner electrons and nuclei play a minimal role in the properties of solids, but their proper inclusion into pseudopotentials creates room for sufficient use of plane-k-points wave basis sets in an electronic structure calculation [95].

The advantage of using the pseudopotential approximation is that it allows for the expansion of the electronic wave-function using much smaller numbers of plane-wave basis states to allow for a small amount of computational time to be required for convergence of energies. The pseudopotential has the form

$$V_{NL} = \sum_{lm} |lm\rangle V_i \langle lm|, \tag{3-15}$$

where $|lm\rangle$ and $\langle lm|$ are the spherical harmonics and V_i is the pseudopotential for angular momentum l. A local pseudopotential is defined as a pseudopotential that uses the same potential for all angular momentum components of the wave function [94]. An example of a non-local pseudopotential is the norm-conserving pseudopotential (NCP) by Kleinman and Bylander [96], which uses a different potential for each angular momentum component of the wave function. The ultrasoft pseudopotential (USP) put forward by Vanderbilt [97] has been implemented in plane-wave calculations. In this pseudopotential, the pseudo-wavefunctions are allowed to be as soft as possible within the core region and cover a wide range of atoms, including the transition metals.

3.4. Brillouin zone sampling

The translational symmetry via the Bloch theorem is used to treat the description of the electronic structure in a periodic system. Boundary conditions that apply to the bulk solid are used to determine the set of **k**-points that allow electron states [79].

$$\varphi_{kt}(\boldsymbol{r}) = \exp[i\boldsymbol{k}.\boldsymbol{r}]\, f_{\boldsymbol{k}}(\boldsymbol{r}). \tag{3-16}$$

This expression has a wavelike $(\exp[i\boldsymbol{k}.\boldsymbol{r}])$ and cell-periodic $(f_{\boldsymbol{k}}(\boldsymbol{r}))$ part. An infinite number of electronic states and atoms is transformed into a finite number of states and atoms in a translationally invariant unit cell but with an infinite number of **k**-points (wave-vectors) in the Brillouin zone.

The occupied states at each **k**-point contribute to the electronic potential in the solid bulk so that in principle an infinite number of calculations are needed to compute this potential.

We need to integrate over all the occupied electronic states to accurately compute the properties of materials such as total energy, forces and stress. However, the computational cost increases linearly with the number of **k**-points within the Brillouin zone [79].

The computational cost is reduced by using special **k**-point schemes that have been developed to use the fewest possible **k**-points for a given accuracy. Some sampling schemes include those of Chadi and Cohen [98], Joannopoulos and Cohen [99], Monkhorst and Pack [100]. However, the most used scheme in **k**-point sampling is that of Monkhorst and Pack.

The treatment of metals, semiconductors and insulators is different. Hence, the type of system determines the number of **k**-points to be used. In the case of a metallic system, a dense **k**-space mesh is required to describe the Fermi surface accurately as possible. A much denser set of **k**-points is used to reduce errors and to ensure the required convergence if the **k**-point sampling does not give a well converged total energy [79, 101].

3.5. Deriving potential models

It is important to obtain appropriate potential models for systems under consideration before any properties of a system are calculated using atomistic simulation methods [102]. In some cases, reliable potential models may already be derived for materials, but in many cases, it is either the potential models are not derived, or the conditions in which a simulation is to be run are far from those that the derived model was fitted to [102, 103]. In

the latter case, the derivation of potential models for desired conditions will be required. There are two possible ways of deriving interatomic potential parameters. Firstly, the parameters can be determined by fitting to data calculated by ab initio, electronic structure calculations, usually attempting to produce an energy surface (a function that describes how the system's energy varies with atomic coordinates). Secondly, it is to derive empirical potential parameters by trying to reproduce experimental data [103]. The approach used in this study is outlined as an empirical derivation approach and discussed below.

In the empirical derivation approach, the potential parameters derived require good experimental data on the crystal properties of relevant compounds. For example, the lattice parameters, ion/internal coordinates and elastic properties provide a reliable way of deriving potential parameters as they are often well characterised, but the experimental error or disagreement between experimental sources may be too great to derive a unique set of parameters in which case additional data is required [102].

The key quantity calculated in the fitting procedure is the "sum of squares" which is a measure of how good the fit is. The aim of the fit is to minimise the sum of squares F, which is calculated as:

$$F = \sum_{all\ observables} w[f_{calc} - f_{obs}]^2 . \qquad (3\text{-}17)$$

The f_{calc} and f_{obs} are the calculated and observable quantities that are being fitted, and w is a weighting factor. Weights are included to guide the fit, and there is no such thing as a unique fit since the fit will depend on the choice of the weighting factor for each observable [103]. The choice of the weighting factor depends on several factors, such as the relative

magnitude of the quantities and reliability of the data. This adjustment is continued until the difference in equation (3-17) is below a specified value. Usually, the final disagreement is well within the experimental error. This method is advantageous since it is relatively simple and can describe the full behaviour of a collection of atoms [102, 103]. The technique used in the fitting of potentials in this study is unique; therefore, a section is devoted to the procedure used to derive the interatomic potential parameters. A summary of the fitting procedure is shown in Figure 3.1.
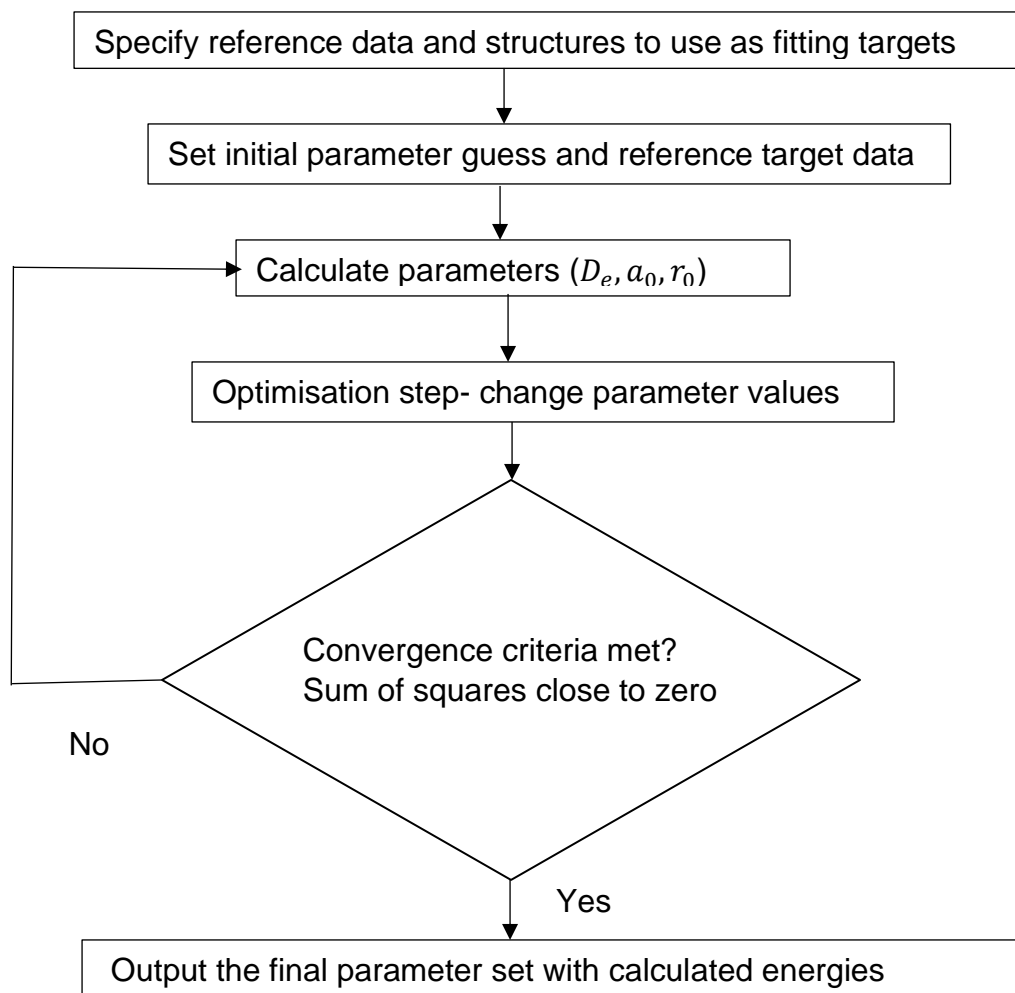
Figure 3.1. A simplified flowchart of the methodology for potential fitting.

3.6. Molecular dynamics

Molecular dynamics (MD) is a computational modelling technique used to simulate simultaneously, the motion of molecules (atoms) under their mutual interactions [82]. It is the most natural method of performing equilibrium statistical-mechanical calculations via simulation. MD plays an important role in the investigation of radiation effects because it provides a methodology for accurate microscopic modelling at the molecular scale. The atoms and molecules can interact for a period, giving a view of the motion of the atoms. Furthermore, the trajectories of molecules and atoms are then determined by numerically solving Newton's equations of motion for a system of interacting particles, where the molecular mechanical force fields define the potential energy and forces between the particles [19, 82].

In molecular dynamics, we follow the laws of classical mechanics, and most notably Newton's first law:

$$F_i = m_i \boldsymbol{a}_i,$$ (3-18)

for each atom, i in a system constituted by N atoms. m_i is the atom mass, F_i is the force acting upon it due to the interactions with other atoms and $\boldsymbol{a}_i$ is the acceleration of the atom given by

$$\boldsymbol{a}_i = \frac{d^2 r}{dt^2},$$ (3-19)

where r is the position of atom i.

To advance the atomic positions and velocities that describe the dynamical behaviour we

40

integrate Newton's equations (3-18) using the Verlet algorithm [104]:

$$r(t + \Delta t) = r(t) + \Delta t v(t) + \frac{1}{2}\Delta t^2 a(t), \hspace{3cm} (3\text{-}20)$$

$$v(t + \Delta t) = v(t) + \frac{1}{2}\Delta t[a(t) + a(t + \Delta t)], \hspace{3cm} (3\text{-}21)$$

The algorithm requires the storage of positions $r(t)$, velocities $v(t)$ and accelerations $a(t)$, all at the same time. MD simulations can be used to measure thermodynamic properties and evaluate the phase diagram of a specific material. MD is also used for other purposes such as studies of non-equilibrium processes and as an efficient tool for optimisation of structures overcoming local energy minima (simulated annealing) [82].

Therefore, molecular dynamics is a deterministic technique given an initial set of positions and velocities, the subsequent time evolution is, in principle completely determined. In more pictorial terms, atoms will "move" into the computer, bumping into each other, wandering around (if the system is fluid), oscillating in waves in concert with their neighbours, perhaps evaporating away from the system if there is a free surface, and so on, in a way similar to what atoms in a real substance would do [105]. The computer calculates a trajectory in $6N$-dimensional phase space ($3N$ positions and $3N$ momenta). However, such a trajectory is usually not particularly relevant by itself.

3.6.1. Energy

The internal energy results from a simulation, as an ensemble average of the energies of the states examined during the simulation [82]:

$$U = \; <E> \; = \frac{1}{M}\sum_{i=1}^{M} E_i. \tag{3-22}$$

The average potential energy V is a result of averaging its instantaneous value, obtained at the same time as the force computation. Thus, the potential energy is given by:

$$V(t) = \sum_i \sum_{j \geq 1} \Phi\big(|r_i(t) - r_j(t)|\big). \tag{3-23}$$

and the kinetic energy is given by:

$$K(t) = \frac{1}{2}\sum_i m_i[\overline{V_i}(t)]^2, \tag{3-24}$$

where m_i is the mass of atom i and $\overline{V_i}$ is the velocity of atom i. Total energy for a system can be represented as the sum of the kinetic energy and the potential energy. The total energy of the system with a given set of positions and velocities is represented by:

$$E_{tot} = K(t) + V(t). \tag{3-25}$$

3.6.2. Temperature

The temperature depends on a certain kind of ensemble for a particular simulation. In a canonical ensemble, the total temperature is constant, whereas in the microcanonical ensemble the temperature is fluctuating. The temperature is directly related to the kinetic energy of the system as follows:

$$K = \sum_i^N \frac{|\dot{P_i}|}{2m_i} = \frac{K_B T}{2}(3N - N_c), \tag{3-26}$$

where P_i is the total of particle i, m_i is its mass and N_c is the number of constraints on the system. In a system, each degree of freedom contributes $\frac{k_B T}{2}$. This is according to the equipartition of energy [82]. If there are N particles, each with three degrees of freedom,

then the kinetic energy should be equal to $\frac{3Nk_BT}{2}$. The total linear momentum of the system

is often constrained to a value of zero in a molecular dynamics simulation, which has the

effect of removing three degrees of freedom from the system and N_c would be equal to 3.

3.6.3. Pressure

Calculation of pressure is usually in a computer simulation via Clausius's virial theorem [82,

105]. This virial is the expectation value for the sum of products of the particle coordinates

and the forces acting on them. Usually, written as

$$W = \sum x_i p_{x_i},$$ (3-27)

where x_i is a coordinate (e.g. the x or y coordinate of an atom) and $\acute{p}_{x_i}$ is the first derivative

of the momentum along that coordinate ($\acute{p}_i$ is the force, by Newton's second law) [105]. The

virial theorem states that the virial is equal to $-3Nk_BT$. In an ideal gas, the only forces are

those due to interactions between the gas and the container, and the virial in this case is

equal to $-3PV$. This result can be obtained directly from

$$PV = Nk_BT.$$ (3-28)

Forces between the particles in a real gas or liquid affect the virial and hence the pressure.

The total virial for a real system equals the sum of an ideal gas part $(-3PV)$ and a

contribution due to interactions between the particles. The result obtained is:

$$W = -3PV + \sum_{i=1}^{N}\sum_{j=i+1}^{N} r_{ij} \frac{dv(r_{ij})}{dr_{ij}} = -3Nk_BT$$ (3-29)

If $\frac{d(r_{ij})}{dr_{ij}}$ is written as f_{ij} the force acting between i and j, then pressure can be presented

as:

$$P = \frac{1}{V}\left[Nk_BT - \frac{1}{3k_BT}\sum_{j=i+1}^{N}r_{ij}f_{ij}\right].$$

(3-30)

3.6.4. Ensembles

Integrating Newton's equations of motion allows one to explore the constant energy surface of a system. However, most natural phenomena occur under conditions where the system is exposed to external pressure and/or exchanges heat with the environment. Under these conditions, the total energy of the system is no longer conserved, and extended forms of MD are required [82]. Several methods are available for controlling the temperature. Different statistical ensembles are generated depending on which state variables, i.e. the enthalpy (H) (i.e. $E + PV$), the energy (E), number of particles (N), pressure (P), temperature (T), stress (S), and volume (V), are kept fixed. The averages or fluctuations of these quantities over the ensemble generated can be used to calculate a variety of energetic, structural and dynamic properties. Furthermore, the three most used ensembles in MD simulations are the NVT, NVE and NPT ensembles [19].

NVT ensemble is also known as a canonical ensemble where temperature and volume are kept constant. This is also the ensemble of choice in this study. In statistical mechanics, it is a statistical ensemble representing a probability distribution of microscopic states of the system [19, 82]. The probability of finding a system in the microscopic state with energy level based on the prior knowledge that the total energy of the system and reservoir combined remains constant, characterises the probability distribution of a system taking

only discrete values of energy.

NVE ensemble is also known as a microcanonical ensemble where energy and volume are kept constant. NVE ensemble is a result of solving the standard Newton equation without any temperature and pressure control. The generation of this adiabatic ensemble causes energy conservation. However, because of rounding and truncation errors during the integration process, there is always a slight fluctuation or drift in energy [82].

NPT ensemble is also known as an isothermal-isobaric ensemble. This ensemble plays a vital role in chemistry as chemical reactions are usually carried out under constant pressure condition. In the NPT ensemble, pressure and temperature are kept constant. MD simulations and experiments are compared using the NPT ensemble [19]. The temperature in the NPT ensemble is controlled using the Langevin method. The partition function can be written as the weighted sum of the partition function of canonical ensemble, $Z(N, V, T)$.

$$\rho(N, P, T) = \int Z(N, V, T) e^{(-\beta pV)C} dV, \tag{3-31}$$

where

$$\beta = \frac{1}{k_B T}, \tag{3-32}$$

k_B is the Boltzmann constant and V being the volume of the system.

3.6.5. Time and system size limits

The amount of memory available to the computer limits the size of an MD simulation, and while technically there is no restriction to the duration of a simulation, the short time-steps required for an accurate simulation (on the order of 10-15 s) imposes a practical limit [19]. Simulations of metal systems (where only 1 or 2 types of atom exist, and only very short-range forces need to be considered) have been made in which millions of atoms have been simulated for nanoseconds. The simulations run during the calculations also consist of individual runs containing 216 atoms at 0.001ps.

3.7. Interatomic potentials

The potential energy for a system of atoms with given positions can be calculated using interatomic potentials [106]. Interatomic potentials are widely used as the physical basis of molecular dynamics and molecular mechanics simulations in material physics or science, chemistry and molecular physics, sometimes in connection with such effects as thermal expansion, cohesion and elastic properties of materials [107]. There are various types of potentials, namely: pair potentials, many-body potentials, Buckingham potentials, Morse potentials and repulsive potentials for short-range interactions.

3.7.1. Buckingham potential

The Buckingham potential is used to describe the Pauli repulsion energy and van der Waals energy for the interaction between two atoms that are not bonded directly as a function of the interatomic distance r [108]. It is used to model two body non-bonded interactions in ionic solids. The general form of Buckingham potential is given by

$$U_{ij} = \frac{z_i z_j e^2}{r_{ij}} + A \exp\left(-\frac{r_{ij}}{\rho_{ij}}\right) - \frac{C_{ij}}{r_{ij}{}^6}, \qquad (3\text{-}33)$$

where the first term is the long-range Coulomb term, the second term is the short-range Pauli repulsion, and the last term is the dispersion energy. The parameter A_{ij} is the size of the ions, ρ_{ij} is the hardness and C_{ij} is the dispersion parameter. In the above equation, the repulsive interaction between the ions is represented by the first term while the second term is the van der Waals attractive interaction of the ions. Table 3.1 shows the Buckingham potential parameters from the Catlow-library [109], used to describe the interactions between Li-Li, Li-Cl and Cl-Cl. Table 3.2 shows the Ti-Ti Buckingham potentials.

Table 3.1. Buckingham potential parameters for LiCl.

	A (eV/Å)	ρ	C (eV)
Li - Li	1153.800	0.1364	0.00
Cl - Cl	1227.200	0.3214	0.34
Li - Cl	1380.600	0.2786	0.00

Table 3.2. Buckingham potentials parameters for Ti.

	A (eV/Å)	ρ	r_0 (Å)	C (eV)
Ti-Ti	13477.9114	0.1723	1.7621	0.0000

The long-range interaction is a result of simplifying all the interactions to include only the pairwise. Fundamentally, the long-range interaction is the electrostatic interaction between the ion pair and as such, can either be attractive for oppositely charged ions or repulsive if they are of like charges [108].

3.7.2. Morse potential

The Morse potential is used to describe the interaction of two atoms that can form a bond to create a diatomic molecule when they approach each other closely. This situation is possible provided the potential energy of the product is lower than that of the reactants. A potential energy curve called a potential well describes the energy minimum. The Morse potential [110] is a well-known pair potential that is important to this day, and it gives analytical solutions for the Schrödinger equation. In 1929, a good approximation for many (vibrating) diatomic molecules was reported, and it has the form

$$U(r) = De^{-2a(r-r_0)} - 2De^{-a(r-r_0)}, \tag{3-34}$$

where D is the depth of the potential well (defined relative to the dissociated atoms), r_0 is the equilibrium bond distance, and a controls the 'width' of the potential (the smaller a is,

the larger the well) and it can be determined from the frequency of classical small vibrations, which in the Morse potential is given by

$$\omega_0 = \frac{a}{2\pi}\sqrt{\frac{2D}{\mu}}, \tag{3-35}$$

where μ represents the reduced mass. The Morse potential makes up the basis of many important many-body potentials.
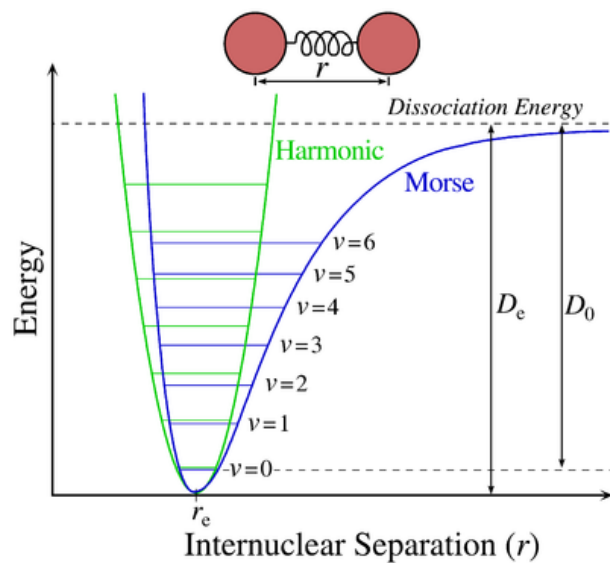
Figure 3.2. Morse potential curve and similarities with the harmonic curve [110].

3.8. Ionic polarizability

Ion polarizability describes the distortion of an electron cloud that surrounds an ion in an electric field. In rigid ion models, this interaction is completely overlooked, as this model treats the ion as point charges. An underestimation of the dynamical properties of the lattice is introduced as the mean error for not adding a polarization term, as the ionic polarizability strongly influences lattice vibrations [111]. The point polarizability model can

be used to obtain a simple description of ionic polarizability. This model has the following form:

$$\mu = \alpha E, \tag{3-36}$$

where μ stands for the dipole moment, introduced by an electric field E and ionic polarizability α, where α is a fixed parameter. However, calculations involving the point polarizability model do not account for the coupling between short-range repulsions and polarizability [112]. Thus, due to the problem with the point polarizable ion model, another model, i.e. the shell model, was required which allows the polarization of the ion to change with changing environment.

3.9. The shell model

Electronic polarization of the atoms is implemented via the Dick-Overhauser model [113]. The electronic polarization of the atoms is represented by the equilibrium distance between the core and shell. This representation is important since there are no electrons in the shell model, and all atoms are effectively represented by point charges. The effects of the electron density flow on the atomic interactions are approximated by the shells.

The shell model is a common model used to incorporate environmental effects. It consists of each ion having two charged particles: a massive rigid core surrounded by a massless shell that mimics the electronic cloud [114, 115]. In simple models, each shell is spherical and rigid and has an internal ionic potential energy that is a function of the displacement

of the shell centre from that of the core, which is usually taken to be harmonic (see Figure 3.3) with force constant k_I giving rise to the interaction energy:

$$U = \frac{1}{2}k_i r_i^2,$$
(3-37)

where r_i is the distance between the core and shell.

The potential energy contributions remaining are the Coulomb interactions between the ions (core-core, core-shell and shell-shell) and short-range pair potentials between neighbouring shells [115]. The parameters are thus the core and shell charges and the internal core-shell force constants for each type of polarizable ion. Thus, the polarizability of a free ion is defined as:

$$\alpha_i = \frac{Y^2}{4\pi\varepsilon_0 k_i}$$
(3-38)

where ε_0 is the permittivity of free space and the numerical constant applies if Y is in electron charge units and k_i is in units of $eV\ Å^2$.
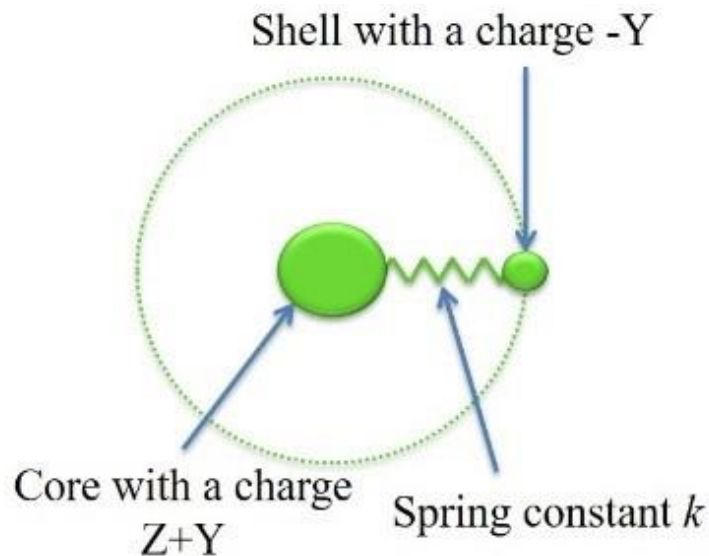
Figure 3.3. Schematic representation of the shell model [116].

The short-range potentials are taken to act between shells, and polarizability is associated with short-range interactions [115]. It should be noted that the shell model doubles the species which are found in rigid ion model. A large number of species results in an increase in the number of degrees of freedom and thus lead to simulations that take a long time to minimise. One advantage observed in this study is the prevention of the core from aggregating into massive particles and maintaining the structural integrity of the structures [114]. The total charge of the ion is divided between the core and a massless shell.

3.10. Simulation codes

3.10.1. Implementation within CASTEP

The Cambridge Serial Total Energy Package (CASTEP) code makes use of a density functional theory with a plane-wave basis set to calculate electronic properties of solids, and it uses its basic property which is energy, to derive other quantities [70, 71]. CASTEP code is employed to perform geometry optimisation calculations on the Ti_7 cluster, after the cluster has interacted with the salt medium (LiCl), to achieve ground state properties. In this dissertation, we use the ultrasoft pseudopotential by Vanderbilt [97] within the CASTEP program. Single-point energy calculations were performed to determine suitable cut-off energy for Ti_7 cluster at different energy cut-offs and different **k**-points. The energy cut-offs were varied from 100 eV – 1000 eV.
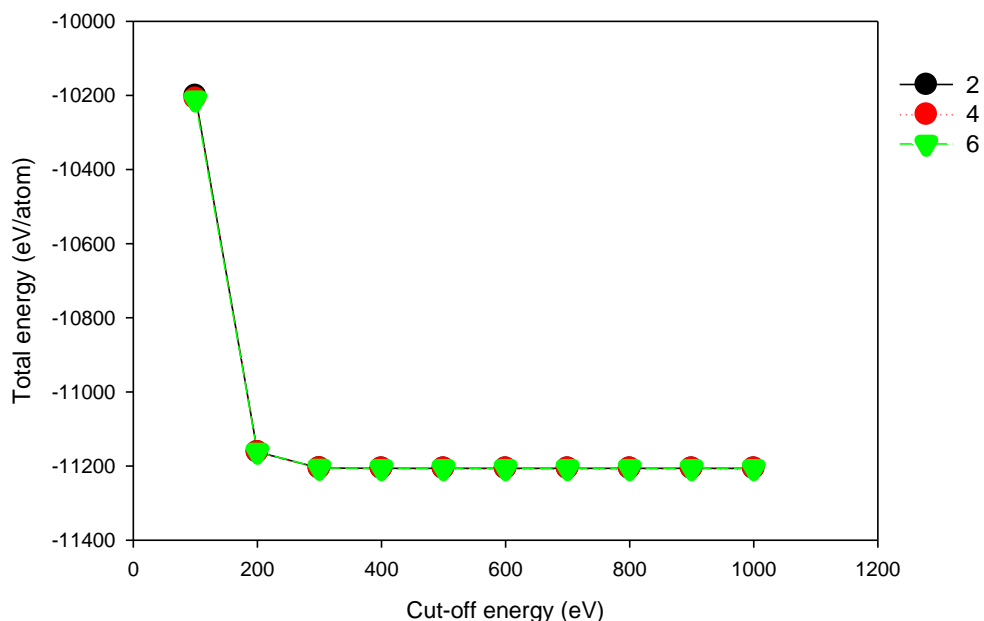
Figure 3.4. Total energy against energy cut-off for titanium cluster (Ti$_7$) at different **k**-points.

Figure 3.4 shows the total energy against energy cut-off for different sets of **k**-points (2x2x2, 4x4x4 and 6x6x6). The graphs show a constant trend starting at 400 eV, and a similar trend is observed for all plots. The energy cut-off of 500 eV was chosen since the total energy after this cut-off energy is almost negligible. A convergence tolerance energy of 1.0x10^{-6} eV/atom was set to ensure accurate energy convergence, thus improving the convergence criteria. Also, Figure 3.4 shows that as the number of **k**-points increases from the 2x2x2 to 6x6x6 **k**-points set, the variation in energy is similar. We employed the Monkhorst and Pack sampling scheme to generate efficient and accurate sets of special points in the Brillouin zone [100]. In order to determine a set of **k**-points that gives rise to the lowest energy, we calculated the **k**-points at a fixed energy cut-off of 500 eV.
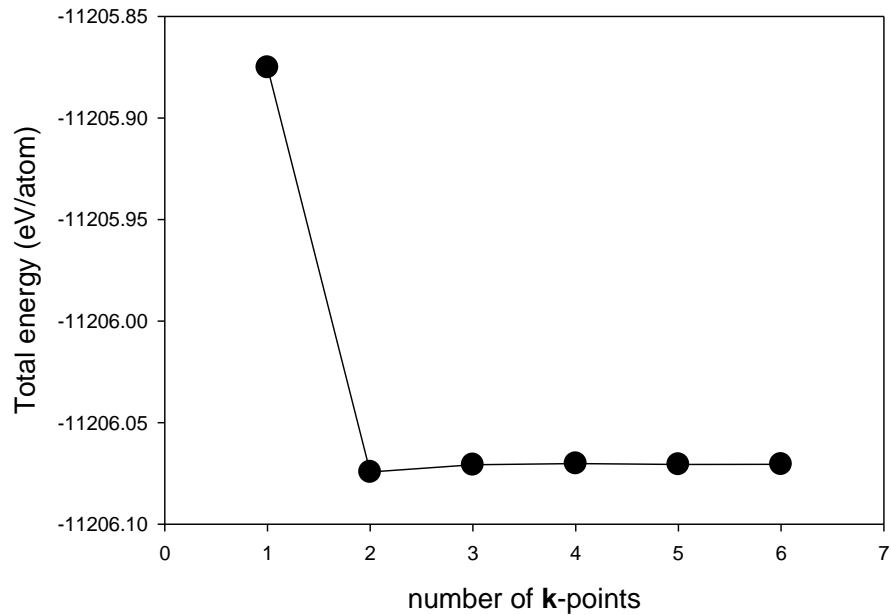
Figure 3.5. Graph of **k**-point convergence of the total energy per atom for titanium cluster (Ti7).

Figure 3.5 shows the total energy against **k**-point sampling with **k**-convergence up to 6 **k**-points of the total energy per atom for titanium cluster (Ti7). We observe that by 3 **k**-points the total energy has converged to within 1meV/atom. This **k**-point set gives a good convergence to the total energy calculations. The calculations were considered converged when the change in total energy is less than 2×10^{-6} eV. Also, the maximum displacement of the atoms during geometry optimisation steps were less than 0.005 Å, and the residual bulk stress was less than 0.1 GPa.

3.10.2. DMol^3 code

The DMol^3 code uses numerically generated atomic wave functions as a basis set and quasi-logarithmically spaced mesh points along the radical direction that generate a set of spheres [72, 73]. Each sphere consists of the Lebedev scheme [117] which was first introduced to solve different types of partial differential equations used in generating angular points. The DMol^3 code is well suited for a massively parallel computational environment with these numerical meshes. DMol^3 incorporates the best atomic functions, which are the exact solutions of the Kohn-Sham [81] for free electrons; they automatically have the correct shape, both close to the nucleus and at large distances. As such by construction, the limit of dissociation for a molecule of a cluster into free atoms is correctly described by DMol^3.

3.10.3. Fritz Haber Institute ab initio molecular simulation

Fritz Haber Institute ab initio molecular simulation (FHI-aims) is an efficient computational materials science program that is based only on quantum-mechanical first principles [20]. The computation of the total energy and derived quantities of molecular or solid condensed matter in its electronic ground state is through its primary production method, which is DFT. FHI-aims is exceptionally efficient for nanostructures and molecular systems while also sustaining high numerical accuracy in all production tasks [20, 118]. Production calculations can handle up to several thousand atoms and efficiently use thousands of cores. It allows for a description of electronic single-quasiparticle excitations in molecules

using different self-energy formalisms and wave-function based molecular total energy calculation based on the Hartree-Fock and many-body perturbation theory [118].

3.10.4. GULP

The General Utility Lattice Program (GULP [21]) is developed to perform a variety of tasks based on the force field method (e.g. calculation at the interatomic level of theory). GULP geometry optimisation supports molecular dynamics of molecules, clusters, 0D, 2D, and 3D systems using a wide range of potential models that span both organic and inorganic fields with fully flexible molecules [102]. This code was written to facilitate the fitting of interatomic potentials to both energy surfaces and empirical data. The potentials include shell model, embedded atoms (for metals), and bond order reactive forcefields [21, 102].

3.10.5. DL_POLY

DL_POLY [22] is a widely used classical molecular dynamics code that has been under continual development at Daresbury laboratory since 1994. It is a code that enables an excellent load-balancing and parallel performance provided that the particle density of the modelled system is close to uniform in space and time. The program can simulate systems as small as 100 atoms and as massive as 30 million atoms [22, 23]. DL_POLY package does not provide any particular set of forcefield parameter to describe the interatomic interactions. However, it does implement an enormous selection of functional forms for the interaction's potentials arising in many forcefields commonly used in molecular simulation.

It contains all commonly used pair potentials $(U_{pair}(r_{ij}))$ which include the Buckingham, Lennard-Jones and Morse potentials, to name a few [23].
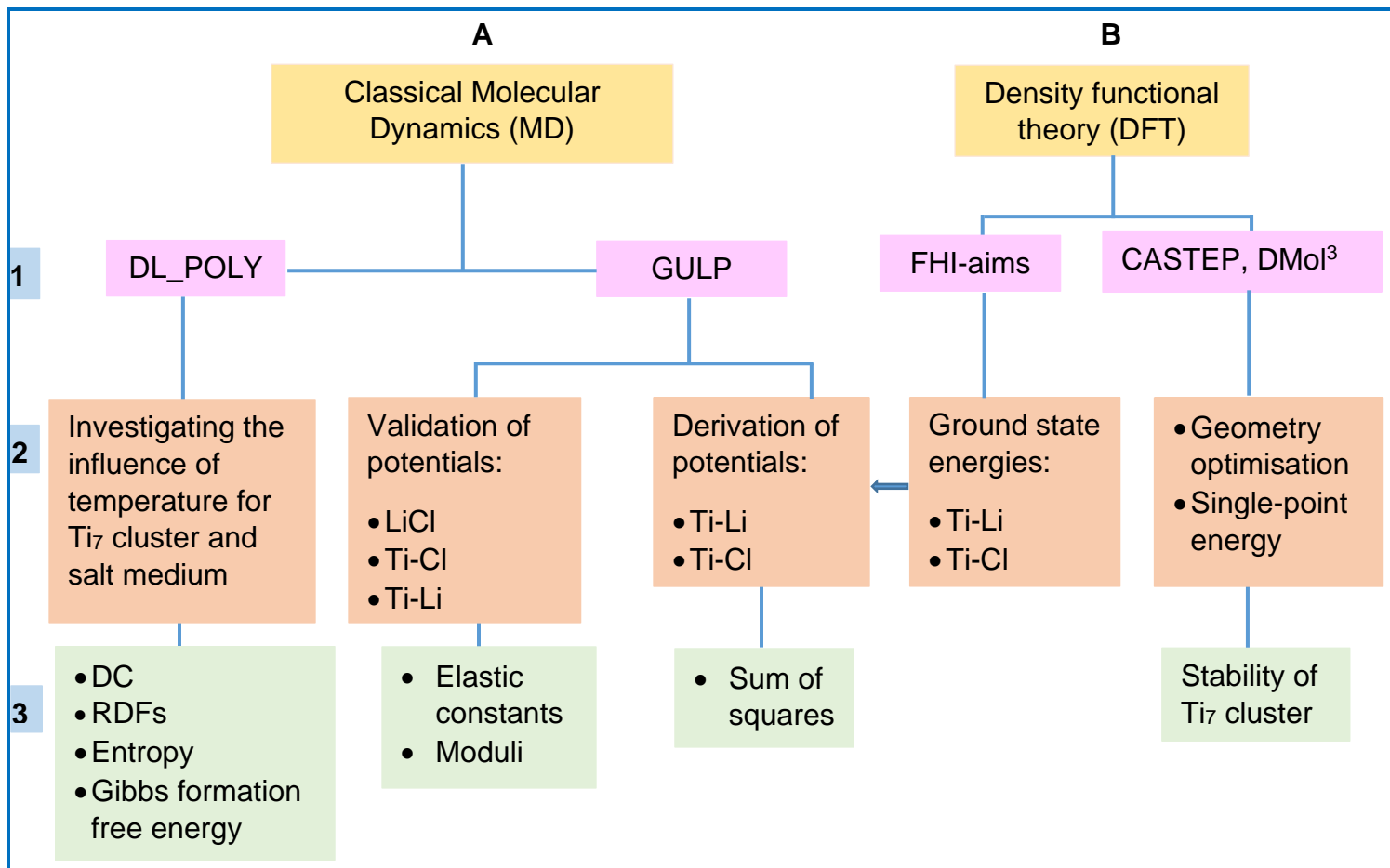
Figure 3.6. A schematic representation showing the methodology, techniques, codes used, as well as the properties calculated.

Figure 3.6 shows the schematic representation of the multi-scale methods that were adopted in the current study. The two main approaches (A) classical molecular dynamics and (B) Density functional theory can be explained as follows:

Stage 1A: Classical molecular dynamics codes i.e., GULP and DL_POLY were used to simulate and calibrate the LiCl, Ti_7/LiCl, $TiCl_n$ and Ti_7/$TiCl_n$ structures.

Stage 1B: Density functional theory code FHI-aims was used to generate the interactions of the Ti_7 cluster with LiCl. While the CASTEP and $DMol^3$ codes were used to perform total energy calculations. Furthermore, predict the stability of Ti_7 cluster.

Stage 2A: DL_POLY code is used to calculate the temperature dependence of the structures. GULP code was employed to validate the systems and also derive the interatomic potentials.

Stage 2B: The ground state energies for the Ti-Li and Ti-Cl interactions were calculated before fitting of potentials was carried out. These energies were used to derive potentials using GULP code.

Stage 3A: Properties such as elastic constants, moduli, diffusion coefficients, radial distribution functions, entropy and Gibbs free energy were calculated.

Stage 3B: The sum of squares property was investigated to measure how good the fitting of potentials was. Geometry optimisation and single-point energies were calculated to evaluate the stability of the Ti_7 cluster after interactions with LiCl.

Chapter 4

Interatomic potential parameters

This chapter is based on the LiCl model, particularly the development and fitting of Li-Cl-Ti interatomic potential parameters from accurate first-principle calculations [20]. Interatomic potentials for describing the Li-Li, Li-Cl and Cl-Cl interactions were adopted from the Catlow-library [109]. In addition, the Ti-Ti interaction is described using Buckingham potentials [108]. The energy minimisation code (GULP) [21] was used to simulate and validate the LiCl structure. Lattice parameters, internal coordinates and elastic constants will be discussed. The validation of the LiCl model is conditioned by the lattice parameters and the Cauchy relation. This is done in order to confirm the Buckingham potentials used produce the properties of LiCl. Further density functional theory was performed. This is to establish suitable conditions for other salt mediums such as TiCl and $TiCl_4$. The fitted interatomic potential parameters were cross validated by comparing the DFT and GULP results.

4.1. Simulating and validating the LiCl structure

The LiCl model was generated in a way that it contains properties similar to those of real systems. This crystal structure was constructed based on the internal coordinates and crystallographic properties stated in Table 4.1. The unit cell of the LiCl structure was specified with a lattice parameter of a=10.62 Å, and the structure was assumed to repeat along the three directions of space at an angle of 90.00° in the xyz direction. LiCl atoms were specified along only three sides of the cubic cell, as atoms on the three opposite sides will be generated when the cell is mathematically replicated, see Figure 4.1.

Table 4.1. Internal coordinates and crystallographic properties of LiCl.

	Crystallographic properties
Li^+	(0 0 0) (½ ½ 0) (½ 0 ½) (0 ½ ½)
Cl^-	(0 ½ 0) (½ 0 0) (0 0 ½) (½ ½ ½)
Crystal system	Cubic
Lattice type	fcc
Space group	Fm3m
Space group #	225
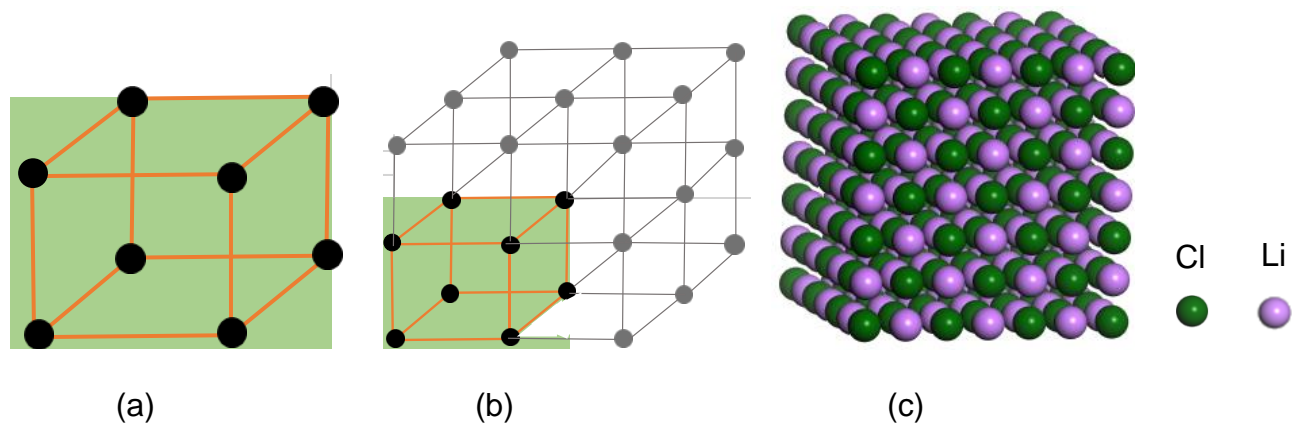
Figure 4.1. (a) fcc unit cell (b) fcc unit cell with replicas and (c) atom positions before optimisation runs of a 10.62 Å 3x3x3 LiCl crystal.

Moreover, after constructing the LiCl structure, the most important factor is model validity which was achieved by using GULP [21]. In order to validate the LiCl structure, geometry optimisation calculations were performed where the lattice parameters, volume and internal coordinates were allowed to vary. The elastic constants were also calculated and compared with available experimental data. Once elastic constants are satisfied, then we can conclude that we have managed to find conditions in which the system is valid. It was found that the lattice parameters and elastic constants compare well with the experimental values [43, 119]. The predicted elastic constants also satisfied the Cauchy relation of $C_{11} = C_{44}$. This Cauchy relation is significant in that it provides a test for selecting pair potentials that can best describe interactions in materials [120, 121]. The simulated LiCl structure was then expanded (supercell of 2x2x2 and 3x3x3) to create enough space relative to the interatomic potential's cut-offs to ensure that no atom interacts with any duplicate atom in both directions along a dimension.

4.2. Energy minimisation

Energy minimisation calculations were performed on the bulk structure to compute the equilibrium configuration of the LiCl structure. This is done because a structure with atoms in perfect crystalline positions results in an imbalance of energy since there are minor atomic vibrations at temperatures near 0 K [122]. Energy minimisation processes employ a mathematical procedure of optimisation to move atoms so as to reduce the net forces on the atoms until they become negligible. The ion positions are adjusted until a minimum energy configuration is reached at 0 K to obtain a more stable structure during energy minimisation of a molecular system [102]. Therefore, the final state of the system corresponds to the configuration of atoms when the temperature of the system is approximately zero. Thus, it is important to find a point for each ion where the force acting upon it is zero.

To minimise the total energy of the system and obtain equilibrium structural properties, we performed constant temperature calculations using the GULP code [21]. The calculation also confirmed that the selected interatomic Buckingham potentials from the Catlow library are valid for the LiCl model. Validation was done by comparing the experimental (Exp.) lattice parameters versus those derived from the simulation run (Calc.). The results are tabulated, as seen in Table 4.2. We obtained a lattice parameter of a= 5.049 Å, which compared well with the experimental value of 5.070 Å [109]. The interatomic Buckingham potentials used were observed to reproduce the structure to within 1% in agreement with experimental data.

Table 4.2. Calculated (Calc.) and experimental (Exp.) lattice parameter of LiCl structure.

	Calc.	Exp.
a (Å)	5.049	5.070 [43]

Elastic constants are important for applications related to the mechanical properties of solid materials and interatomic bonding [123]. For a cubic structure, the elastic constants regarded are the C_{11}, C_{12}, and C_{44}. The C_{12} and C_{44} are known as shear elastic constants. Elastic constants are deduced by analysing the change in the calculated values of stress that result from strain changes [124, 125]. The elastic constants provide information on the magnitude of the repulsive part of the near-neighbour interaction and the attractive part of the next-nearest neighbour potential [109].

Table 4.3 lists the calculated elastic constants (C_{ij}) and anisotropy (A) values of LiCl at zero pressure and zero temperature. The calculated results for C_{11} and C_{12} are larger than the experimental data, except for C_{44}, which is less than its experimental value. Also, the value of C_{12} is equal to C_{44}, suggesting that the Cauchy relation holds, and the potential parameters used can reproduce the properties of the LiCl structure. These findings are in agreement with experimental results, as shown in Table 4.3. The anisotropy factor A was calculated from the elastic constants using the equation below

$$A = \frac{2C_{44}}{(C_{11}-C_{12})},$$ (4-1)

Table 4.3. Calculated (Calc.) and experimental (Exp.) LiCl elastic constants (C_{ij}) in GPa and anisotropy (A) factor.

LiCl	C_{11}	C_{12}	C_{44}	A
Calc.	69.140	26.152	26.152	1.217
Exp. [119]	63.200	23.800	27.600	

Table 4.3 shows that the value of A is above 1.0, which suggests that LiCl cannot be regarded as elastically isotropic. The result indicates that the properties of the structure change with different crystallographic orientations. Anisotropy results agree with other computational work reported by Hou *et al.* [123].

4.3. Fitting potential parameters for the Li-Cl-Ti interaction

Within the GULP code, before any properties of a system are calculated, it is important to derive potential parameters for that system. A complete Li-Cl-Ti interatomic potential requires parametrizations for the Li-Li, Cl-Cl, Li-Cl, Ti-Ti, Ti-Li and Ti-Cl interaction. Firstly, a combination of Buckingham potentials from Catlow library was used to describe the Li-Li, Li-Cl, Cl-Cl and Ti-Ti interactions within the GULP code. The results were satisfactory, as discussed above. Secondly, the Ti-Cl and Ti-Li interactions were derived using FHI-aims code by considering first optimising Cl and Li, and then subject these optimised systems to titanium cluster (Ti_7). This approach was intended to predict the best possible interactions that may be used for deriving the potentials.

Thus, to determine the potential parameters for Ti-Cl and Ti-Li interactions, the FHI-aims code was used to calculate the ground state energies of these interactions. This was achieved by simulating a lithium/chlorine atom or lithium chloride between two symmetrically oriented titanium clusters (Ti$_7$) as shown in Figure 4.2.
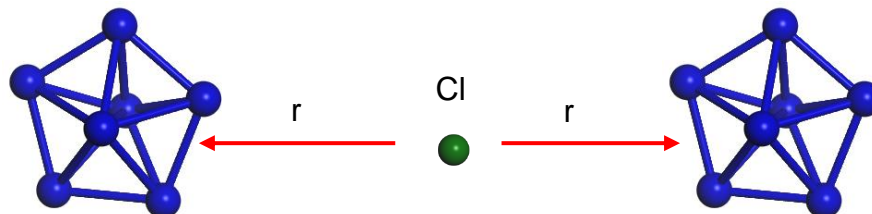
Figure 4.2. Chlorine atom simulated between two Ti$_7$ clusters.

The distance r between the clusters and the central atom (Cl/Li) was varied from 2.0 Å– 5.0 Å with a 0.1 increment. This was done using a script whereby the central atom is at a fixed position, and the clusters are simultaneously moved towards the central atom to a distance of 2.0 Å. Furthermore, this was done until a distance of 5.0 Å is reached, where the cluster is likely to experience a maximum or minimum electrostatic force (repulsion or attraction). The variation of the distances was done in order to calculate the ground state energies for interacting atoms at different possible distances. This is done to ensure the accuracy of the potential parameters to be derived. The FHI-aims code was used to calculate the ground state energies of the system at different Ti$_7$ distances, and binding energies were then calculated.

The binding energies were calculated using the equation

$$E_b = \frac{1}{2}(E_{FHI} - 2E_{Ti} - E_{alk}),$$ (4-2)

where E_b is the binding energy, E_{FHI} is the total energy from FHI-aims calculations, E_{Ti} is the energy of the titanium cluster with the coefficient "2" indicating that there are two Ti7 clusters and E_{alk} represents the energy of Li/Cl.

The binding energies of the Ti-Cl and Ti-Li interactions are shown in Figure 4.3 and denoted as DFT curve. From this graph, it was observed that the trend followed by the DFT curve is similar to that of a Morse-potential curve. Recall that the Morse potential is determined using equation (3-34), as described in chapter 3 $(U(r) = De^{-2a(r-r_0)} - 2De^{-a(r-r_0)})$. The lowest binding energy for each interaction and its corresponding distance was used as the D_e and r_0 values in this equation, and the a_0 parameter is the value where the 'dip' of the two curves coincides. Results from the Morse equation calculations are denoted as the Morse curve in Figure 4.3.
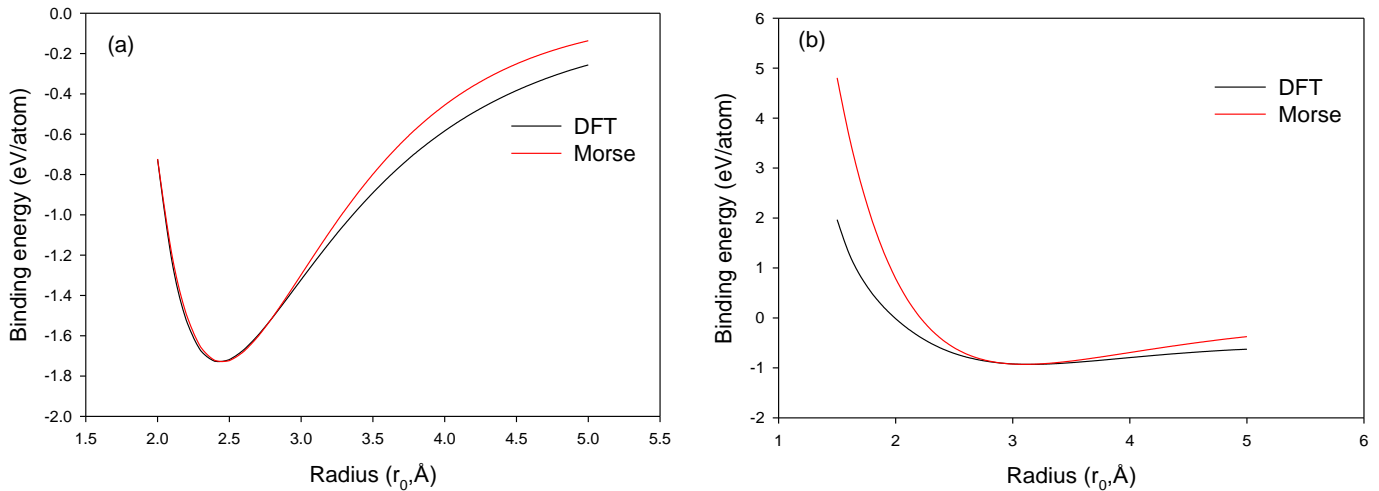
Figure 4.3. The interaction of the system deduced from binding energies calculated from FHI-aims energies between (a) Ti-Cl and (b) Ti-Li for the DFT and Morse potential.

Figure 4.3 shows the comparison between the (a) Ti-Cl and (b) Ti-Li interactions using DFT and Morse potential methods. For each interaction, the D_e, r_0 and a_0 values that were used in the Morse equation were taken as initial values for the fitting process. The relaxed-fitting algorithm [103] was used in all parameter determinations. In this algorithm, the optimisation of the crystal structure is performed at every stage of the least sum of squares procedure.

The fundamental quantity in potential fitting is the 'sum of squares' which is a measure of how good a fit is. A fit aims to minimise the sum of squares by varying the potential parameters, and at the end of the fit, this quantity should be zero. This criterion will only happen in cases where the potentials can be guaranteed to completely reproduce data [21]. The parameters for fitting were calculated using the values that are set as the initial guess, and the internal coordinates of all individual atoms given for all atoms included in the fitting process. The findings from the fitting process were optimised and used as the initial values for fitting the Li-Cl-Ti interactions. Results of the Li-Cl-Ti fitting are indicated in Figure 4.4 (a) as the GULP curve and the parameters listed in Table 4.4 as initial parameters.

The Ti-Cl fitting results are used as initial values for the fitting of Li-Cl-Ti interactions since these parameters resulted in a sum of squares close to zero. Recall that the DFT and Morse curves do not coincide well for the Ti-Li interaction in Figure 4.3 (b). Fitting of these Ti-Li parameters resulted in a sum of squares far from zero. This Indicated that the initial parameters adopted from Figure 4.3 (b) were not suitable parameters for describing the

Ti-Li interaction. However, from Figure 4.4 (a), we observe that the GULP curve can be manoeuvred to allow the two curves to coincide, by fine-tuning the D_e, r_0 Morse parameters to give the desired output, which is a sum of squares close to zero. The a_0 parameter was not altered since this was the value where the 'dip' for DFT and Morse curves coincided in Figure 4.3 (b).
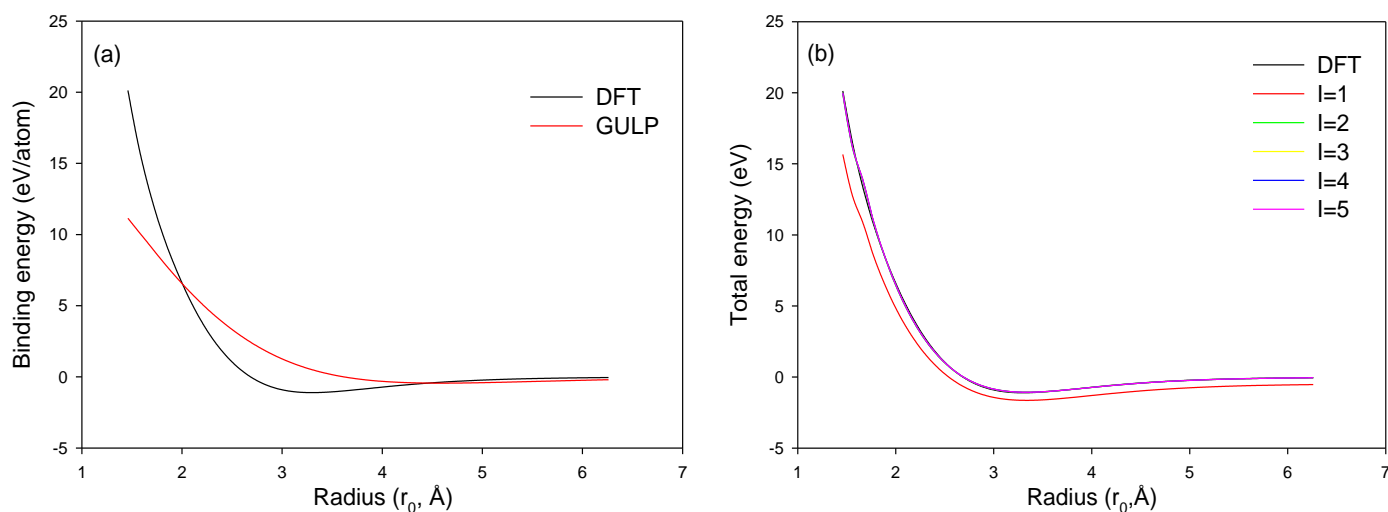
Figure 4.4. Validation of Li-Cl-Ti potential using GULP code.

Thus, a successive two-parameter search technique was used to minimise the sum of the squares error function. This technique involves the fitting of parameters, optimising the fit result and then using the optimised result as the initial potential parameters for the next fit until the given convergence criteria of a sum of squares close to zero. The technique is shown through Figure 4.4 (b) and each search is denoted with an "I" followed by a number, e.g. I=1 for the first iteration. In Figure 4.4 (b), we observed that the first iteration was able to align the DFT and GULP graph curves but still needed to be fine-tuned further. The parameters were able to give a final sum of squares close to zero at the third iteration and

the values for the Li-Cl-Ti potential parameters listed in Table 4.4. The column labelled as initial shows the optimised parameters after the fit for Ti-Cl and Ti-Li interactions and the Final values after fitting for the Li-Cl-Ti interaction. We observe that for Ti-Cl, the initial and final parameters remained the same, indicating that the parameters described the Ti-Cl interaction well.

Table 4.4. Morse pair potential parameters.

	Ti-Cl		Ti-Li	
	Initial	Final	Initial	Final
D_e	0.400	0.400	0.033	0.730
a_0	1.279	1.279	0.857	1.717
r_0	2.681	2.681	3.875	2.000

Chapter 5

Influence of temperature on LiCl and Ti$_7$/LiCl structures

In this chapter, we present results on molecular dynamics calculations that were carried out to study the temperature dependence of LiCl and Ti$_7$/LiCl systems using different structure models (rigid ion model and shell model). The shell model is important to model the effects of polarization of an ionic compound LiCl, while the rigid ion model treats ions as point charges and overlooks short-range interactions [112].

The derived model, i.e. LiCl, as discussed in chapter 4, was adopted to evaluate its behaviour at high temperature using molecular dynamics simulations. This is important since molecular simulations provide an insight into the structural and transport properties of materials. The transport and structural properties such as diffusion coefficients and radial distribution functions were calculated. This was done to understand the lithium and chlorine ion diffusion capability for each LiCl model, and the behaviour of titanium cluster with n=7 (Ti$_7$) at various temperatures. In addition, their structural transformations are calculated in order to estimate atomic interactions in the case of other structures such as TiCl and TiCl$_4$. The DL_POLY code [22] was used to calculate the thermodynamic properties of LiCl and Ti$_7$/LiCl employing the rigid ion model and shell model. Thereafter, the evolution and growth of the Ti$_7$ cluster after contact with the LiCl medium is investigated using DFT codes such as CASTEP and DMol^3.
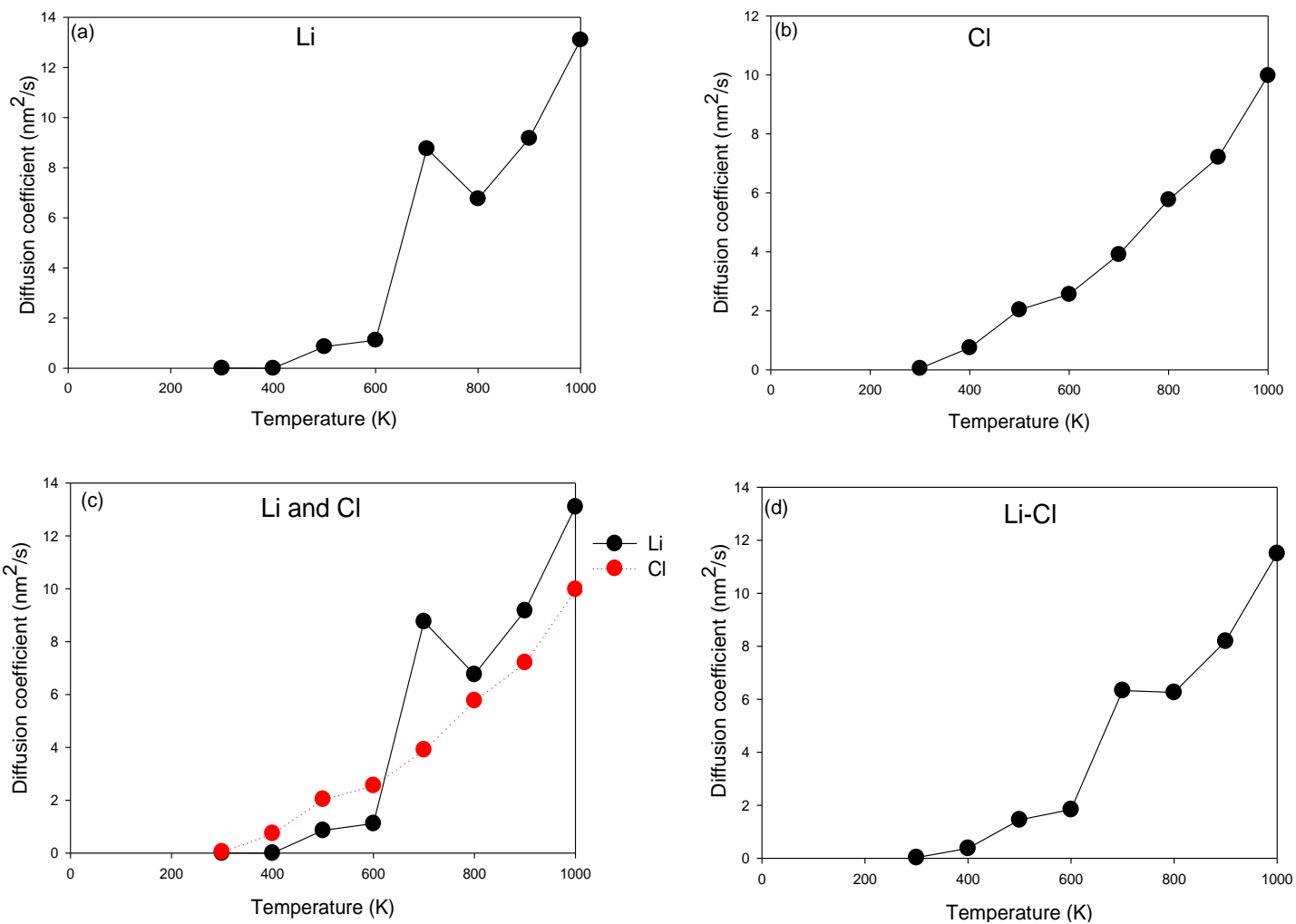
5.1. Diffusion coefficient

Diffusion coefficient (DC), also known as diffusivity, is defined as a measure of the mobility of species (atom, molecules, or ions) and depends on the frequency in which the species moves and the size of each movement [126]. DC was determined to trace the trajectories of Li^+ and Cl^- ions for the LiCl system, as well as their motion. An increase in temperature results in an increase in the diffusion coefficient. This is attributed to the molecules gaining more kinetic energy when the temperature is applied to the system.

Figure 5.1 depicts the diffusion coefficient graphs for LiCl rigid ion model at various temperatures. The lithium ion (Figure 5.1 (a)) diffuses slightly at around 400 K – 500 K then a kink at 500 K - 600 K before a sharp increase until 700 K and forms a "knee" behaviour. This behaviour is similar to those observed for NaCl system, where a self-diffusion of Na and Cl was reported [34, 35]. It was indicated that this is attributed to the presence of a "frozen equilibrium" at low temperature [34]. Furthermore, it can be clearly seen that LiCl self-diffusion coefficients are separately reproduced at low temperature range of about 610 K – 780 K. Moreover, the diffusion coefficient decreases until 800 K and then increases sharply until 1000 K. The chlorine graph, Figure 5.1 (b), shows an exponential increase in the diffusion coefficient from 300 K – 1000 K and then a slight kink from 500 K – 600 K. Figure 5.1 (c) shows a comparison of the lithium and chloride ions diffusion coefficients in one set of axes. At 300 K, the chlorine ions show mobility followed by the lithium graph at 400 K. At temperatures above 800 K, both graphs indicate an increase until 1000 K with the diffusion rate of Li dominant at high temperature. The sharp

peaks for Li suggest minimum Li-Li interactions for the second-neighbouring ions that are also observed in the RDFs where the second peak is not observed at that temperature.

Figure 5.1 (d) shows the average diffusion coefficient for the system. At 300 K – 600 K, the graph follows a similar pattern to the lithium diffusion. At 600 K – 700 K, there is also a sharp increase in the diffusion coefficient followed by a small kink at 700 K – 800 K (which is as a result of Li diffusion) and an increase until 1000 K. However, the diffusion coefficient shows an exponential increase at high temperature. This clearly shows that Li promotes DC than Cl.

Figure 5.1. Diffusion coefficient graphs for (a) Li, (b) Cl, (c) comparison between Li and Cl, (d) average for Li and Cl ions; for LiCl rigid ion model.

Figure 5.2 depicts the diffusion coefficient graphs for LiCl shell model. In Figure 5.2 (a), the lithium diffusion graph shows the mobility of ions from 300 K – 1000 K. The figure depicts a decrease in the mobility of the ion at 400 K – 500 K. At 500 K – 600 K, the diffusion coefficient increases and at 600 K – 700 K, the diffusion is slowly varying and only increases significantly at 800 K until 1000 K. Furthermore, in Figure 5.2 (b), the chlorine diffusion follows a similar pattern to the lithium diffusion, except at 600 K – 700 K

where constant immobility is observed. An increase in mobility is observed until 900 K and then constant immobility observed at 900 K – 1000 K.

Figure 5.2 (c) compares the diffusivity of Li and Cl ion at various temperatures. The lithium and chlorine graphs coincide with each other at 300 K – 600 K, and then there is a slight shift in the lithium ions at 600 K – 800 K. This suggests that the Li diffusivity is favourable at that temperature range. The diffusivity graphs of these ions are similar at 800 K – 900 K followed by an increase in the diffusivity of lithium, and constant immobility of chlorine is observed at 900 K – 1000 K. Figure 5.2 (d) shows the average diffusion coefficient for the system and this graph shows a similar pattern to the chlorine diffusion graph. This indicates that Cl promotes diffusivity than Li.
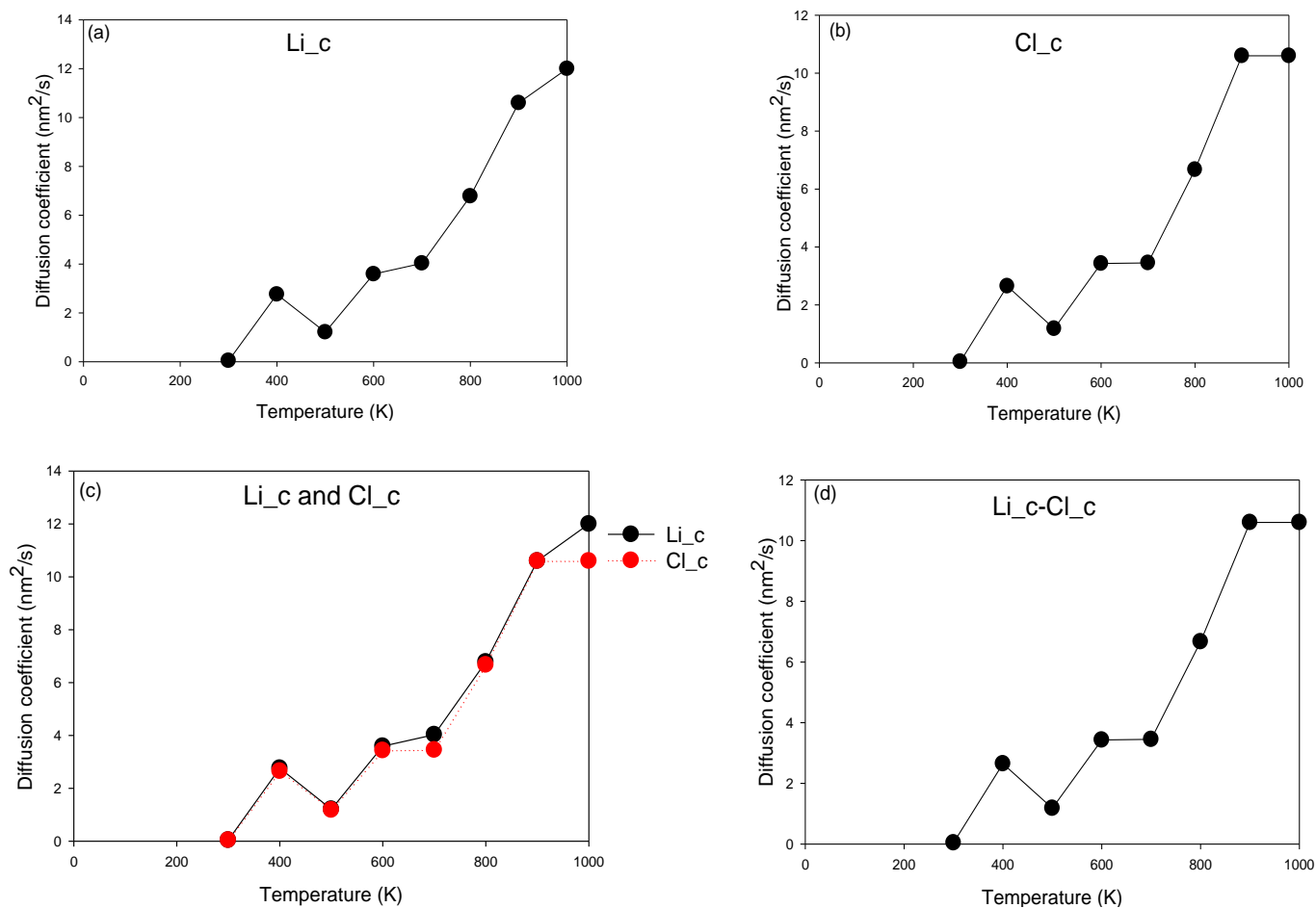
Figure 5.2. Diffusion Coefficient graphs for (a) Li_c, (b) Cl_c, (c) comparison between Li_c and Cl_c, (d) average for Li_c and Cl_c ions; for LiCl shell model.

Figure 5.1 and Figure 5.2 revealed that $DC_{Li} > DC_{Cl}$, this could be as a result of the atomic mass effect, which suggests that the lighter the ion, the higher the diffusivity. It is reported that the diffusion coefficient is constant at the melting temperature for a given crystal structure [127]. Thus, we note the melting temperature range for rigid ion model at 700 K – 800 K (Figure 5.1), the calculated value is closer to the experimental melting temperature range of 878 K – 887 K (605ºC -614 ºC) [128] while in the case of shell model (Figure 5.2), the melting temperature is at 600 K – 700 K. Based on the results in Figure 5.2, we observe

that the shell model calculations exaggerate the changes in the LiCl structure relative to those found for the rigid-ion model in Figure 5.1 (b). The difference between the calculated and experimental melting temperatures may be attributed to a slight mismatch in the potential parameters, which have a substantial effect on the melting temperature and in turn resulted in an insignificant difference in the observed structural lattice parameters.
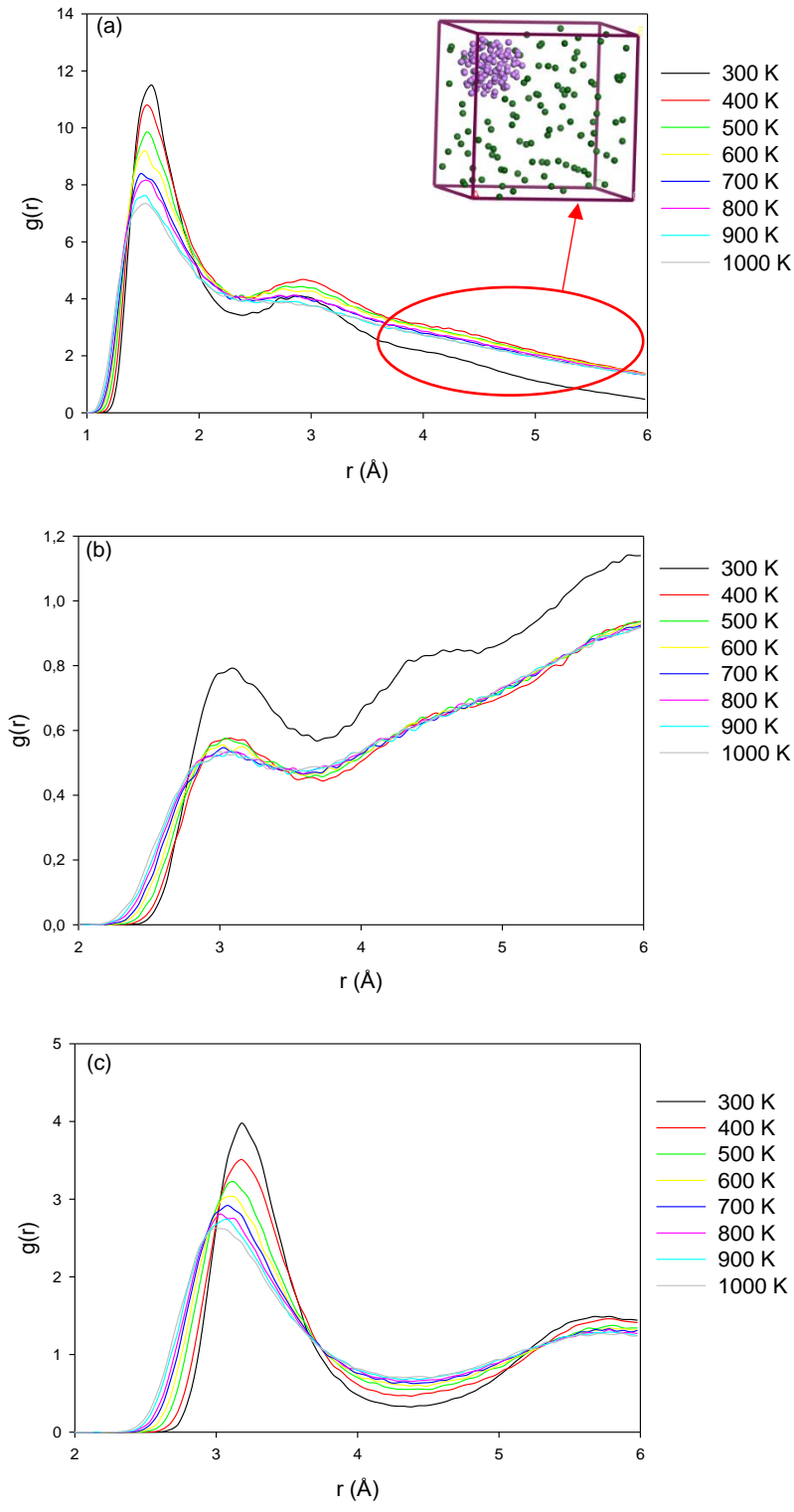
5.2. Radial distribution function for LiCl

Radial distribution function (RDF) is an essential structural characteristic that is used to understand the interactions of atoms in a system. In the recent work, we will calculate the RDF for LiCl in both rigid ion and shell models at various temperatures in the range 300 K – 1000 K. The first peak represents the interatomic bond length in each interaction. At higher temperatures, the general trend observed by some interactions is a decrease in peak height and a broadness of the peak width.

Figure 5.3 illustrates the Li-Cl, Li-Li, and Cl-Cl interactions for the LiCl rigid ion model. Figure 5.3 (a) shows the radial distribution function graph for Li-Li. The graph depicts the first peak around 1.58 Å and g(r) around 11.52, while the first principle molecular dynamics (FPMD) [129] indicates the first peak at 3.70 Å. At around 3.53 Å – 5.98 Å, the graph decreases rapidly until a g(r) around 0.47. This observation may be attributed to the aggregation of the cations to one region, as indicated by the corresponding snapshot showing the Li-Li interaction in a cell. As the temperature is increased, lithium bonds

loosen, and the cations diffuse through the system as indicated by the broadening of the peaks.

Figure 5.3 (b) depicts the first peak at 3.08 Å and g(r) around 0.79. The second peak is at 4.33 Å, and g(r) around 0.82 at 300 K. The FPMD results [129] indicates the first peak around 2.20 Å and a second peak around 5.70 Å. The radial distribution graph shows that the height of the first peak decreases with an increase in temperature while the width of this peak broadens to almost a straight line. This may suggest that the interaction between Li-Cl is weaker at higher temperatures, due to the increase in the kinetic energy of atoms suggesting melting. Furthermore, the second peak at 300 K is broad and shows that there are still atom-atom interactions observed in the system. However, this peak starts to disappear around 800 K, which implies a random distribution of atoms that results in the structure beginning to lose its morphology. The linear increase of the second peak height may be due to unlike ions clustering around a reference ion with less steric hindrance from its second neighbouring atoms. Moreover, all the peaks converge and fluctuate near g(r)= 1.20, which suggests that they all reach a molten state in equilibrium. This observation is similar to the work reported by Sinha and Duwez [130] for amorphous Ni-Pt-P alloys.

Figure 5.3 (c) depicts the first peak at 3.18 Å and g(r) around 3.98, and a second peak at 5.68 Å with g(r) around 1.49. The first peak values are comparable with the FPMD results [129] to within a percentage difference of 2%. Figure 5.3 (c) indicates that there is no long-range order at long distances since g(r) is approaching one (g(r)≈1).
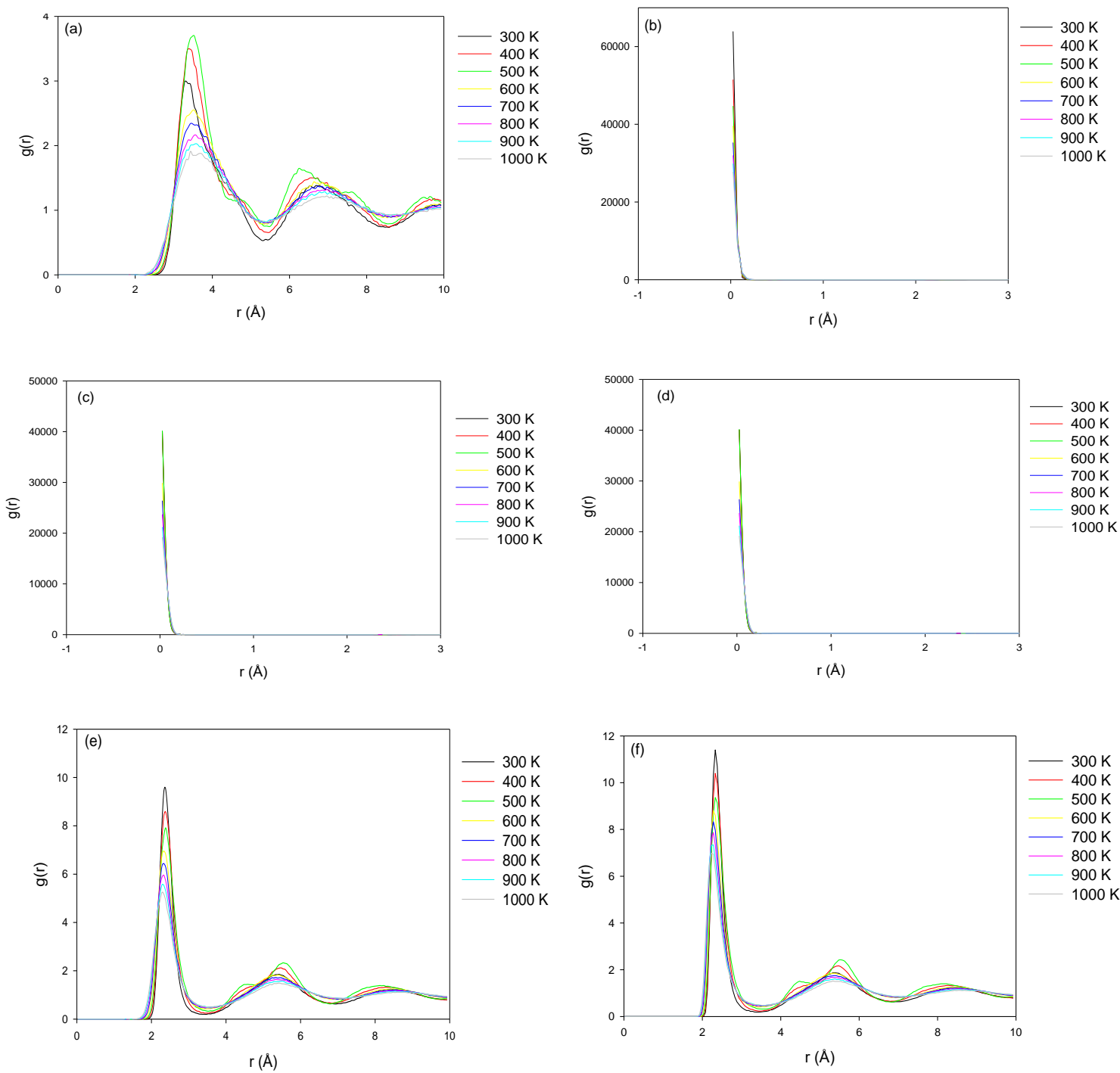
Figure 5.3. Radial distribution function for (a) Li-Li, (b) Li-Cl, and (c) Cl-Cl for LiCl rigid ion model. The insert in (a) shows the Li dimers.

Figure 5.4 illustrates the radial distribution function for the LiCl shell model. Figure 5.4 (a) shows the radial distribution function graph for Li_c-Li_c. The graph depicts the first peak around 3.43 Å and g(r) around 2.99 and a second peak at 6.78 Å at a g(r) around 1.38. Figure 5.4 (b), (c) and (d) shows the interactions of the core-shell in a single atom. The graph starts at a higher value of g(r) at a radial distance corresponding to 0.03 Å, and it gradually decreases until a g(r) of 0.00. The observation may be attributed to the understanding that radial distribution functions measure the probability of finding an atom at distance r away from a reference atom. In this case, if Li_c is the reference atom, then Li_s will be the nearest atom at a distance r. However, Li_c and Li_s are at the same distance since Li_s acts as an electron cloud, as discussed in chapter 3. Moreover, the FPMD results [129], reported the Li-Li first peak at 3.70 Å. The results are comparable to within a percentage difference of 7%.

Figure 5.4 (e) and (f) shows the Li_c-Cl_c and Li_s-Cl_s interactions of the system. The graphs for these interactions are also similar, as seen in Figure 5.4. The Li_c-Cl_c graph shows the first peak at 2.38 Å, and g(r) around 9.53 and the first peak for Li_s-Cl_s is at 2.33 Å with g(r) around 11.42.

Figure 5.4. Radial distribution functions for (a) Li_c-Li_c, (b) Li_c-Li_s, (c) Cl_c-Cl_s, (d) Cl_s-Cl_c, (e) Li_c-Cl_c and (f) Li_s-Cl_s for LiCl shell model.

Figure 5.5 (a) depicts the Li_s-Li_s first peak at 3.48 Å and g(r) around 3.33. The second peak is at 6.68 Å and g(r) around 1.40. It is noted that the Li_c-Li_c and Li_s-Li_s graphs are similar. The similarity is also noted on the bond distances (first peak value of 3.43 Å) and is comparable to within a percentage difference of 2% and 1% respectively, with the FPMD results [129]. Figure 5.5 (b) and (c) shows the Li_c-Cl_s and Li_s-Cl_c interactions of the system. The Li_c-Cl_s graph shows the first peak at 2.33 Å around 9.26 and the first peak for Li_s-Cl_c at 2.38 Å with g(r) around 12.00. In addition, the results are comparable with the FPMD results [129] to within a percentage difference of 1% and 4%, respectively.

Furthermore, it is noted that Figure 5.6 (a) and (b) depicting the Cl_c-Cl_c and Cl_s-Cl_s interactions are similar. Figure 5.6 (a) depicts the first peak at 3.58 Å with g(r) around 3.91 and Figure 5.6 (b) depicts the first peak at 3.48 Å with g(r) around 4.09. The FPMD results [129], indicates the first peak around 2.20 Å and a second peak around 5.70 Å. This implies that in the shell model, there is a long-range order of atoms since g(r) for Cl_c-Cl_c and Cl_s-Cl_s interactions are not approaching one at long distances (g(r)$\neq$ 1).
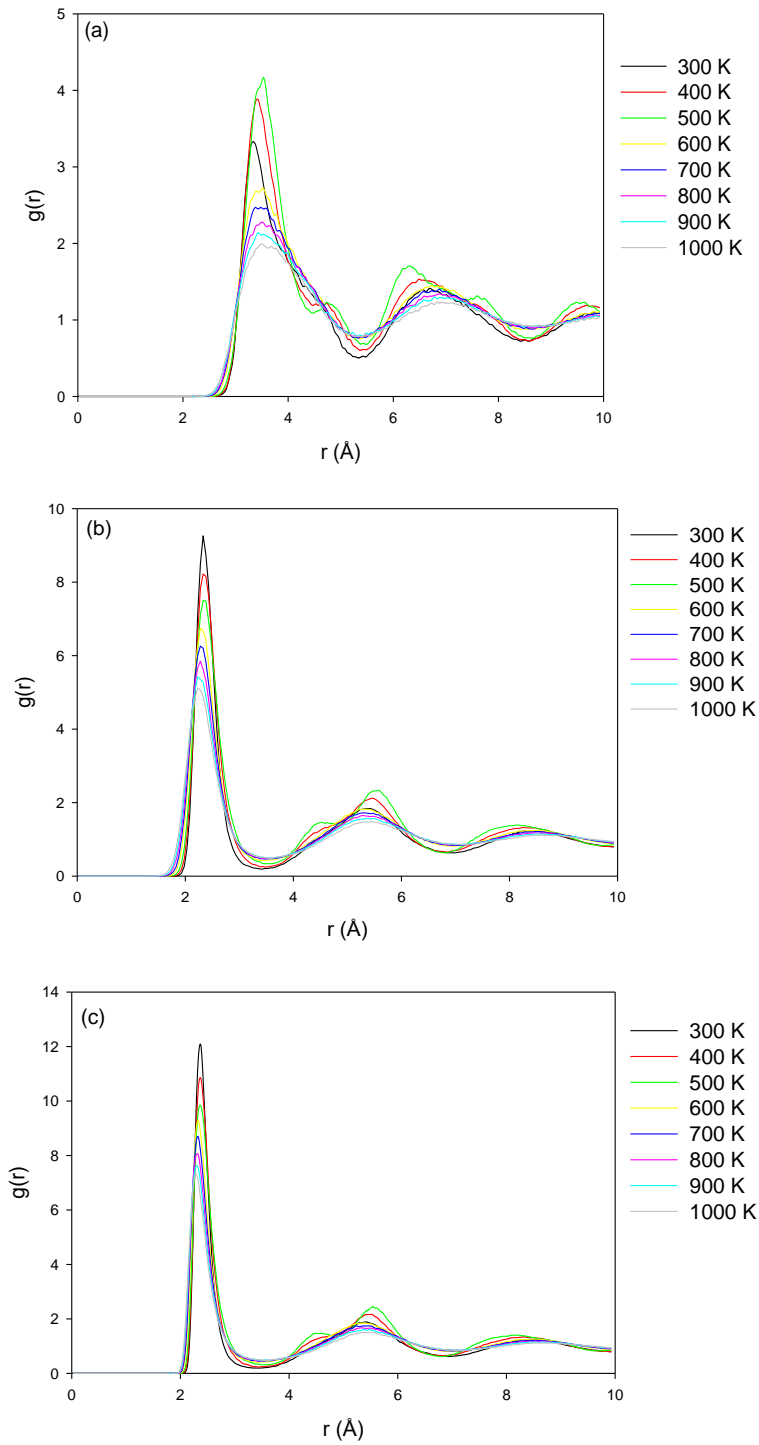
Figure 5.5. Radial distribution function for (a) Li_s-Li_s, (b) Li_c-Li_s, and (c) Li_s-Cl_c, for LiCl shell model.
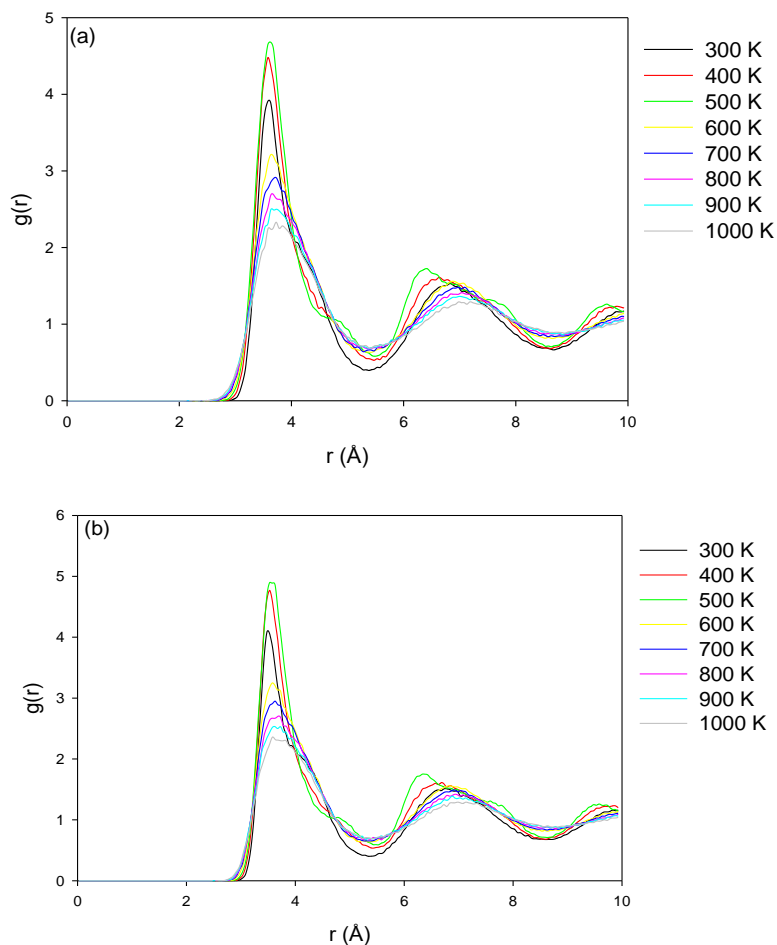
Figure 5.6. Radial distribution function for (a) Cl_c-Cl_c, and (b) Cl_s-Cl_s for LiCl shell model.

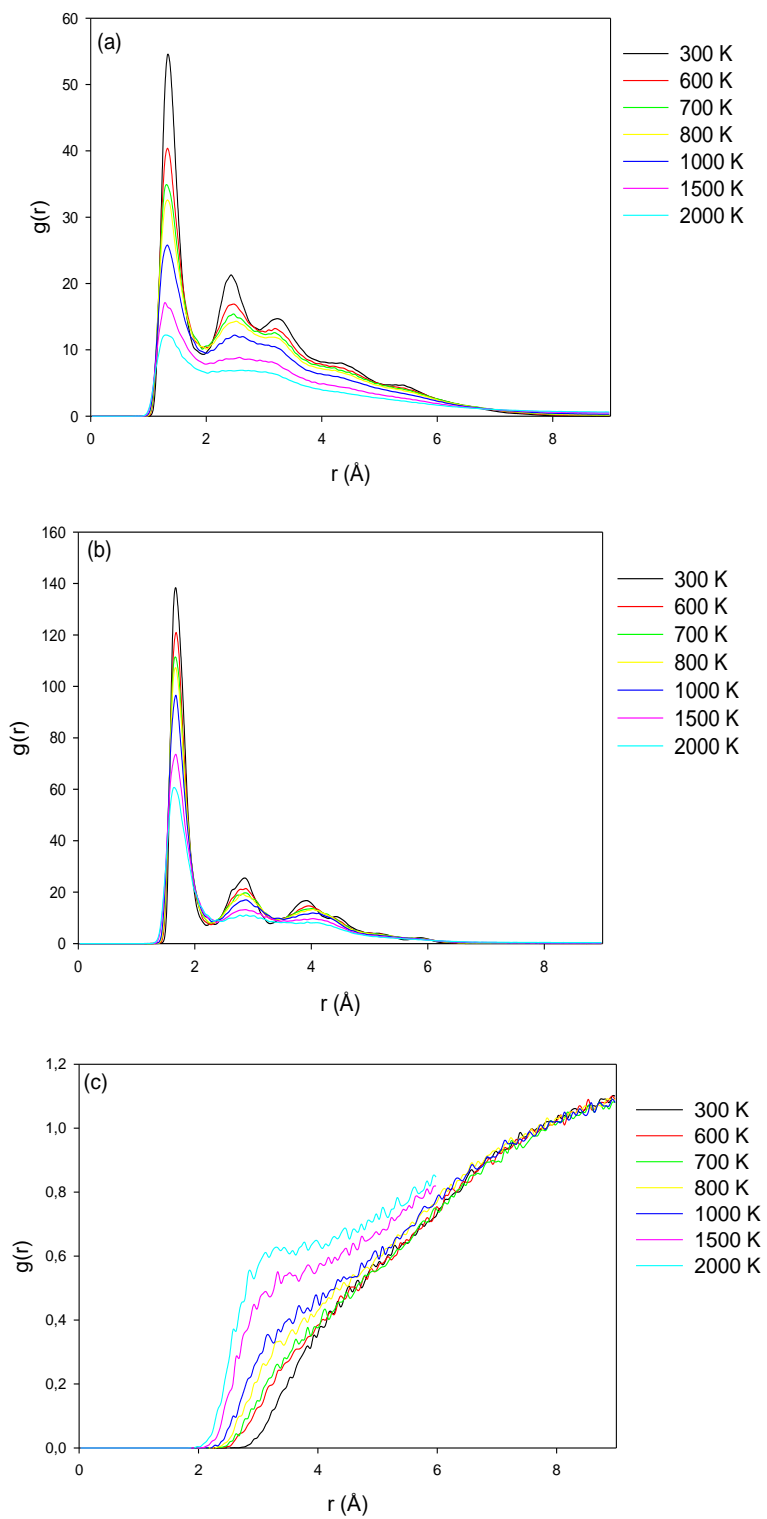## 5.3. Radial distribution function interactions in Ti₇/LiCl

This section describes the interaction of titanium cluster (Ti₇) with LiCl environment. The Ti₇ cluster was chosen for this purpose since it was reported as the special or magical number within the clusters. This is done in order to understand how titanium can react in this medium to gain understanding towards titanium production processes.

5.3.1. Ti$_7$/LiCl interaction (LiCl rigid ion model)

Firstly, we describe the interaction with LiCl rigid ion model at 300 K – 2000 K. The first peak represents the interatomic bond length in each interaction. In Figure 5.7 (a) we note that the RDF for the Li-Li bond indicates the first peak at 1.33 Å and g(r) of 54.50. The FPMD results show a Li-Li first peak at 3.70 Å [129]. Also, the Li-Ti$_7$ bond length is shown in Figure 5.7 (b). The first Li-Ti$_7$ peak is at 1.68 Å with a g(r) of 138.00. Figure 5.7 (c) shows the first peak of Li-Cl at 5.43 Å and g(r) of 0.64. The experimental values for the Li-Li, Li-Cl bond lengths are 2.672 Å and 2.021 Å [131], respectively. Deviations from the current findings may be due to the interatomic potential parameters employed.

The Ti$_7$-Ti$_7$ bond length is shown in Figure 5.8 (a) at 2.83 Å and g(r) at 176.00 in agreement with the theoretical bond length of 2.65 Å as reported for the bicapped trigonal bipyramid geometry for Ti$_7$ cluster [55]. Figure 5.8 (b) shows the first peak of Ti$_7$-Cl at 5.58 Å and g(r) of 0.76. This may suggest that the interaction between Ti$_7$ and Cl are weaker as distance r is increased due to the clustering of the Li ions on the cluster. The Cl-Cl bond length is shown in Figure 5.8 (c) at 3.93 Å with a g(r) at 1.80. This is in agreement with the FPMD LiCl results [129], which shows the first peak at 3.90 Å. The figures reveal that at higher temperatures, there is a decrease in peak height and a broadness in the peak width. Furthermore, the sharp peaks on the RDFs illustrate the strong bonds between the atoms and a high probability of atom location within a radial distance of 10 Å.

Figure 5.7. Radial distribution function for (a) Li-Li, (b) Li-Ti₇, and (c) Li-Cl for the Ti₇/LiCl system (rigid ion model).
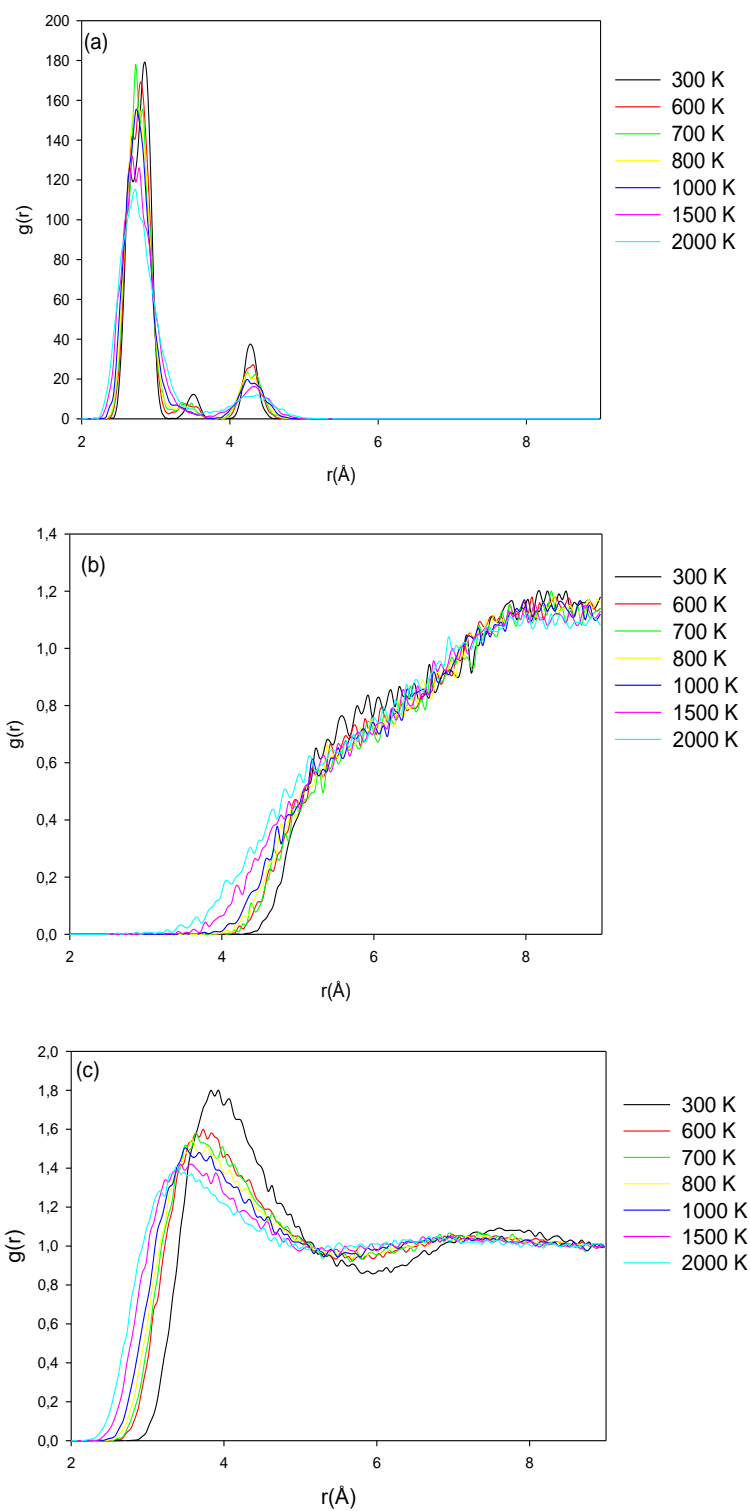
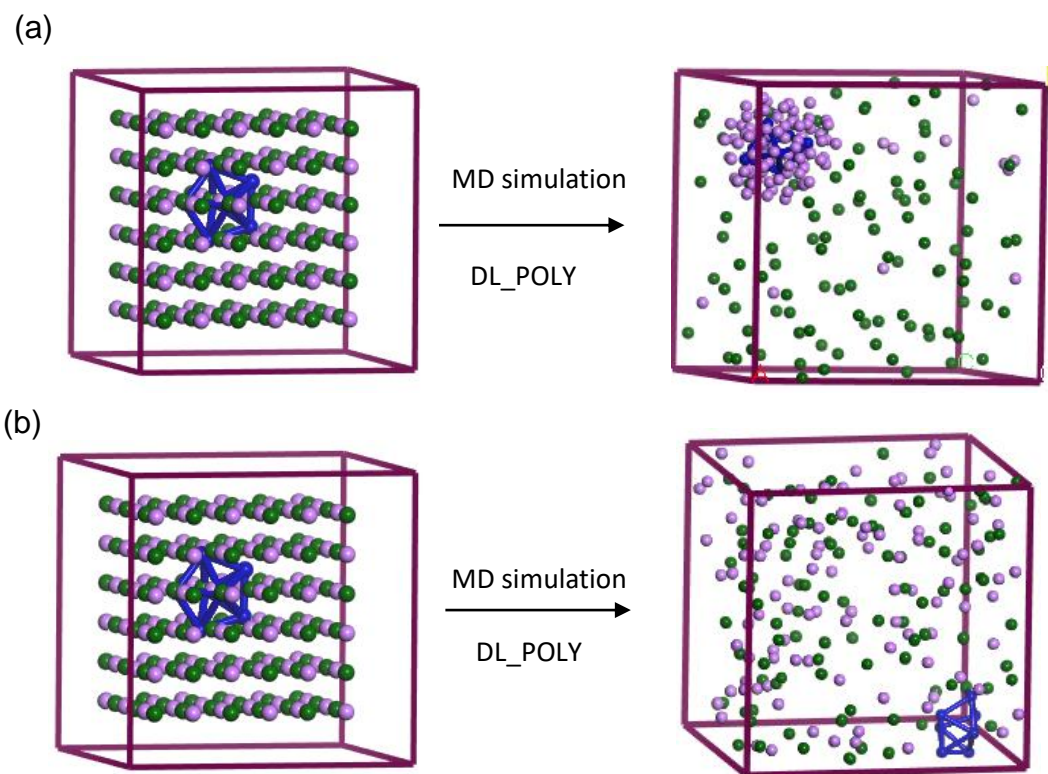**Figure 5.8.** Radial distribution functions for (a) Ti₇-Ti₇, (b) Ti₇-Cl and (c) Cl-Cl for the Ti₇/LiCl system (rigid ion model).

Moreover, the RDFs indicate a decrease in the number of peaks in the 2nd nearest neighbouring atoms when the temperature is increased. The peaks at 2.43 Å and 3.23 Å (Figure 5.7 (a)) merge into a single and much broader peak. The RDFs indicate that at higher temperatures, the bonds are weak, and the atoms are randomly distributed in the system indicating a phase change. This observation is expected since increasing the temperature of a system results in the atoms gaining more kinetic energy; thus, the rapid motion of atoms and random distribution of atoms indicating a phase change.

An atomic representation of the observation made in the Li-Li and Li-Ti$_7$ RDFs is shown in Figure 5.9 (a). The figure symbolically shows the observations made in the RDFs for rigid ion model, in which we observe that lithium tends to cluster around the Ti$_7$ cluster, but chlorine does not. This might be due to the probability rate (g(r)) of lithium being very low and the graph approaching g(r) closer to 0.35 at longer distances, as shown in Figure 5.7 (a). The observation has prompted an investigation on what would be the interactions of the Ti$_7$ cluster in LiCl shell model. Figure 5.9 (b) depicts observations made in Figures 5.10 (section 5.3.2), which indicates no clustering of atoms around the Ti$_7$ cluster and a random distribution of atoms.

Figure 5.9. Interaction of Ti$_7$ with lithium chloride in (a) LiCl rigid ion model and (b) LiCl shell model.

5.3.2. Ti$_7$/LiCl interaction (LiCl shell model)

Figure 5.10. shows the radial distribution functions for Ti$_7$/LiCl system using LiCl shell model. Note that the Li_c-Li_c, Li_c-Li_s, Li_s-Li_s, Li_c-Cl_c, Li_c-Li_s, Li_s-Cl_c, Li_s-Cl_s, Cl_c-Cl_s, Cl_s-Cl_c, Cl_c-Cl_c and Cl_s-Cl_s interactions are similar as in Figure 5.4-5.6, thus not discussed in this section. Instead, we will only discuss the interactions of the titanium cluster with the LiCl shell model, i.e. Li_c-Ti_c, Li_s-Ti_c, Cl_c-Ti_c, Cl_s-Ti_c and Ti_c-Ti_c interactions. Also, note that *s* is for the shell, *c* for the core and *Ti_c* is the core for Ti$_7$ cluster.

Figure 5.10 (a) shows the radial distribution function graph for Li_c-Ti_c. At 300 K, the graph depicts the first peak around 1.83 Å and g(r) around 18.00. Figure 5.10 (b) shows the interactions for Li_s-Ti_c. The first peak is observed at 1.83 Å and g(r) around 21.90. Figure 5.10 (c) shows the Ti_c-Ti_c first peak at 2.63 Å and g(r) around 257.00 in agreement with the reported theoretical value of 2.63 Å for capped octahedron Ti_7 cluster geometry [55].

Figure 5.11 (a) and (b) shows the Cl_s-Ti_c and Cl_c-Ti_c interactions, respectively. Cl_s-Ti_c interactions (Figure 5.11 (a)) shows the first peak at 1.38 Å and g(r) around 10.30. In Figure 5.11 (b) the first peak is indicated at 1.48 Å and g(r) around 8.45. Figure 5.11 indicates that an increase in temperature results in an increase in the peak height (g(r)) of the first peak at 500 K, however, the peak decreases as temperature increases above 500 K. The observed trend might indicate that at 500 K there is a decrease in the correlation of the particles as a result of the fast-translational motion of the system. This is because a fast translation motion results in a decrease in ion-ion correlations which results in an increase in g(r) value as temperature increases. Also, this observation is similar to reported work by Mohoric *et al.* [132] on the effects of translational and rotational degrees of freedom.
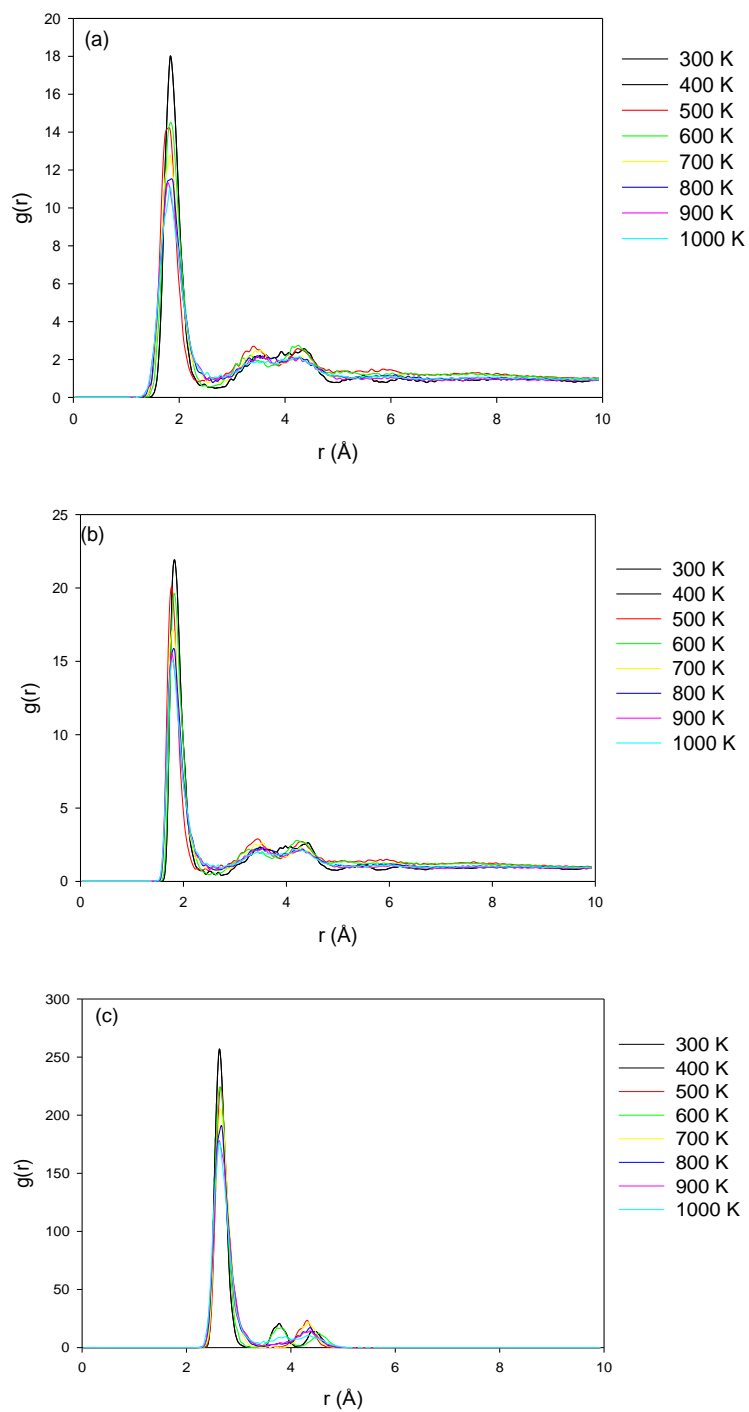
Figure 5.10. Radial distribution functions for (a) Li_c-Ti_c, (b) Li_s-Ti_c and (c) Ti_c-Ti_c for Ti₇/LiCl (LiCl shell model).
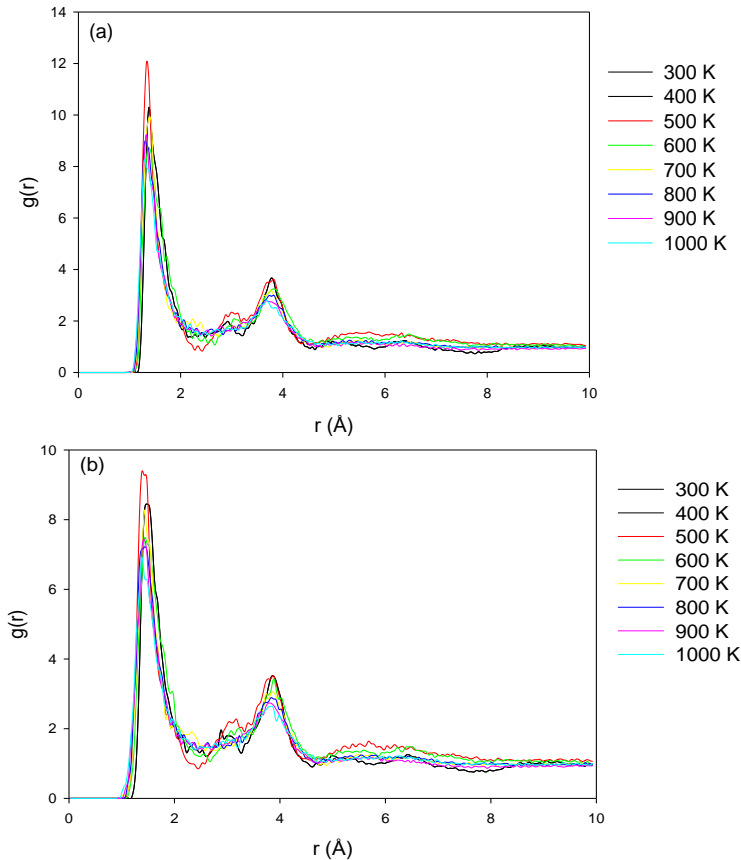
Figure 5.11. Radial distribution functions for (a) Cl_s-Ti_c and (b) Cl_c-Ti_c for Ti$_7$/LiCl (LiCl shell model).

5.4. Diffusion coefficient for Ti$_7$/LiCl system.

5.4.1. Ti$_7$/LiCl (LiCl rigid ion model)
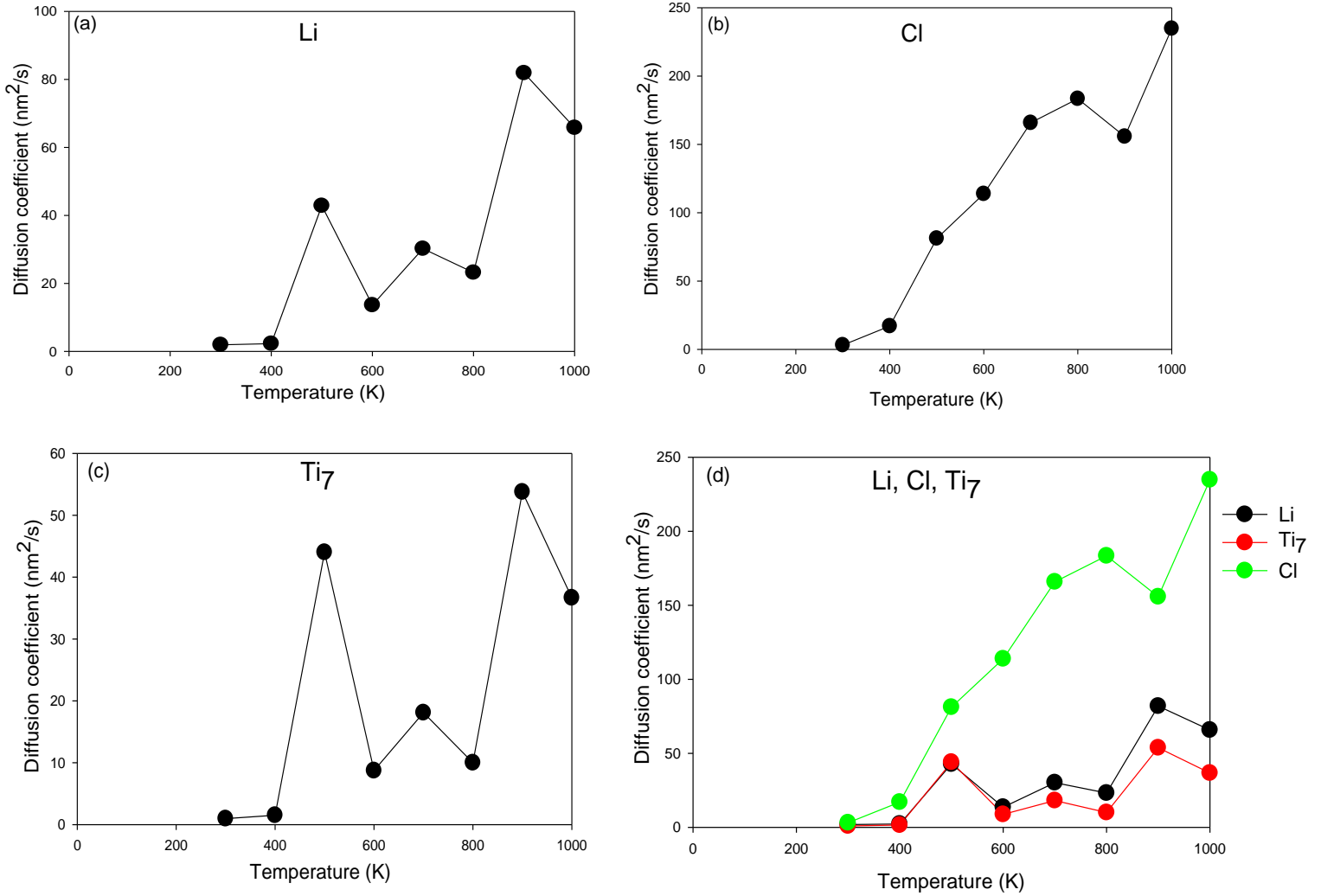
Figure 5.12 depict the diffusion coefficient (DC) graphs for Ti$_7$/LiCl rigid ion model at 300 K – 1000 K. We note that the diffusion coefficient curve of Li and Ti$_7$ are similar, DC for the former is slightly higher (Figure 5.12 (a)). This may be indicative that the rigid ion model overestimates the diffusivity of the ion since short-range interactions are not taken into

consideration [112]. Figure 5.12 (a) shows that the DC undergoes an exponential increase until 500 K before it decreases to 600 K. A slight increase in DC is observed from 600 K to 700 K followed by a slight decrease in the temperature range 700 K - 790 K. The graph then exponentially increases to 900 K before decreasing again around 920 K - 1000 K. The diffusivity trend in this figure shows fluctuation as the temperature is increased, similar to Figure 5.12 (c). These observations suggest that the energy barriers for diffusion are too high with respect to temperature resulting in the formation of single jumps ("knee" behaviour). This is again as a result of Li and Ti_7 self-diffusion, similar to Figure 5.1. However, the Li and Ti_7 self-diffusion coefficients occur at two regions i.e. low temperature range of 420 K – 590 K and high temperature range of 810 K – 980 K.

The chlorine graph in Figure 5.12 (b), shows an exponential increase in the DC from 380 K – 800 K followed by a slight decrease at 900 K before the diffusivity increases until 1000 K. Figure 5.12 (c) shows a titanium diffusion coefficient graph similar to the Li curve. This may be due to the ionic radius of Ti and Li being more than that of Cl.

Figure 5.12 (d) shows a comparison of the lithium, chlorine and titanium cluster diffusion coefficients in one set of axes. This was done to compare the diffusion trend of each ion at different temperatures. At 300 K – 400 K, we observe a decrease in the lithium and titanium cluster diffusivity whilst the chlorine ions show mobility through a linear increase in its diffusion coefficient. The Ti_7 and Li curves are similar and coincide from 300 K to around 600 K. At 600 K, we observe that the titanium cluster diffusivity becomes lower than that of Li. However, the Li curve follows a similar trend but different DC. The

observation might be attributed to the molecular weight of Ti being more than that of Li. This indicates that as the temperature is increased, the atoms gain more kinetic energy and, since Li is lighter than Ti, Li is likely to diffuse faster than Ti.
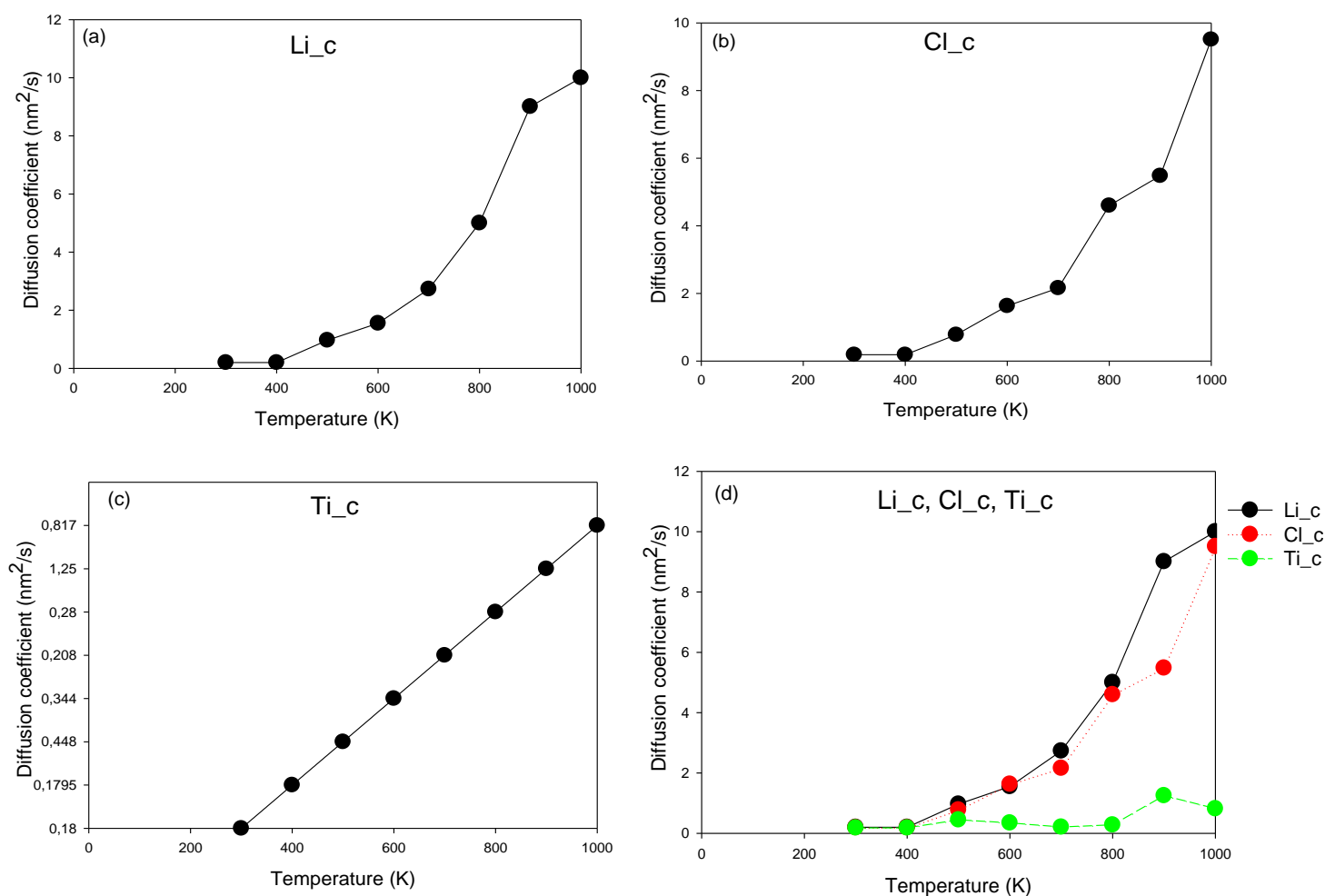

Figure 5.12. Diffusion coefficient for (a) Li, (b) Cl, (c) Ti$_7$ and (d) comparison between Li, Cl, Ti$_7$ diffusions for Ti$_7$/LiCl structure (LiCl rigid ion model).

5.4.2. Ti₇/LiCl (LiCl shell model)

The diffusion coefficient (DC) for the Ti₇/LiCl in the case of LiCl shell model is shown in Figure 5.13. Recall that the shell model considers the effects of polarization of an ionic compound (see section 3.8). Figure 5.13 (a) depicts the diffusion coefficient graph for Li. The Li ions mobility is detected at 400 K where a linear increase in the diffusion rate is observed until around 920 K where the curve slightly changes to almost equal to a DC of 10 nm^2/s at 1000 K. In Figure 5.13 (b), the chlorine diffusion is observed from 300 K and increases exponentially until 600 K. In the temperature range 600 K – 700 K and 800 K – 890 K, the diffusion rate is almost equivalent followed by an increase around 900 K – 1000 K. The titanium cluster graph on the other hand (Figure 5.13 (c)) shows a linear increase in the diffusion rate from 300 K – 1000 K.

Figure 5.13 (d) shows a comparison of Li_c, Cl_c and Ti_c diffusion rate in one set of axes. Since the shells in the system do not affect the diffusion coefficient, the diffusion coefficient of Li_s and Cl_s is almost zero. Both Li_c and Cl_c curves have high diffusing rates than Ti_c. The two curves are almost similar at 300 K – 600 K and 600 K – 900 K. Furthermore, we observe an exponential increase on the Li_c curve until at 900 K where the curve slightly decreases to 10 nm^2/s. In addition, the diffusion rate is low for the Ti_c ion.

Figure 5.13. Diffusion coefficient for (a) Li_c, (b) Cl_c, (c) Ti_c and (d) comparison between the Li_c, Cl_c, Ti_c diffusions for Ti_7/LiCl structure (LiCl shell model).

5.5. Temperature dependence of the Ti_7/LiCl structure.

In this section, we investigate the total energy for the interaction of titanium cluster (Ti_7) with LiCl environment. This is done in order to understand the effects of temperature on titanium cluster and the behaviour of the Ti_7 cluster to gain understanding towards titanium production processes. It is clearly seen that the kinetic energies and the motion of ions for each model increase as the temperature increases.

Figure 5.14 (a) depicts the total energy of the Ti_7/LiCl system at different temperatures for LiCl rigid ion. The rigid ion total energy graph (Figure 5.14 (a)) increases exponentially at temperatures below 1000 K and linearly above this temperature as the temperature is increased. Figure 5.14 (a) shows the titanium cluster retains its original geometry of pentagonal bipyramid except at 900 K. This geometry is reported as the most stable configuration of the Ti_7 cluster [133]. The titanium cluster undergoes a transition at 900 K to a capped octahedron, suggesting that at 900 K the cluster is unstable.

Figure 5.14 (b) shows the total energy of the Ti_7/LiCl at 300 K – 1000 K for LiCl shell model. The shell model (Figure 5.14 (b)) show a completely linear increase in energy as the temperature is increased. We note that the total energy is more favourable as the temperature is increased compared to the rigid ion model. This is indicated by the low total energies depicted on the graph suggesting stability. Therefore, we can deduce that the shell model is the most stable model for investigating Ti_7 interaction in LiCl environment. We further observed that the cluster transitions from a capped octahedron geometry at 300 K and pentagonal bipyramid geometry at 500 K back to a capped octahedron at 600 K. At 700 K – 1000 K, the titanium cluster is stable since it has its most stable geometry (pentagonal bipyramid).
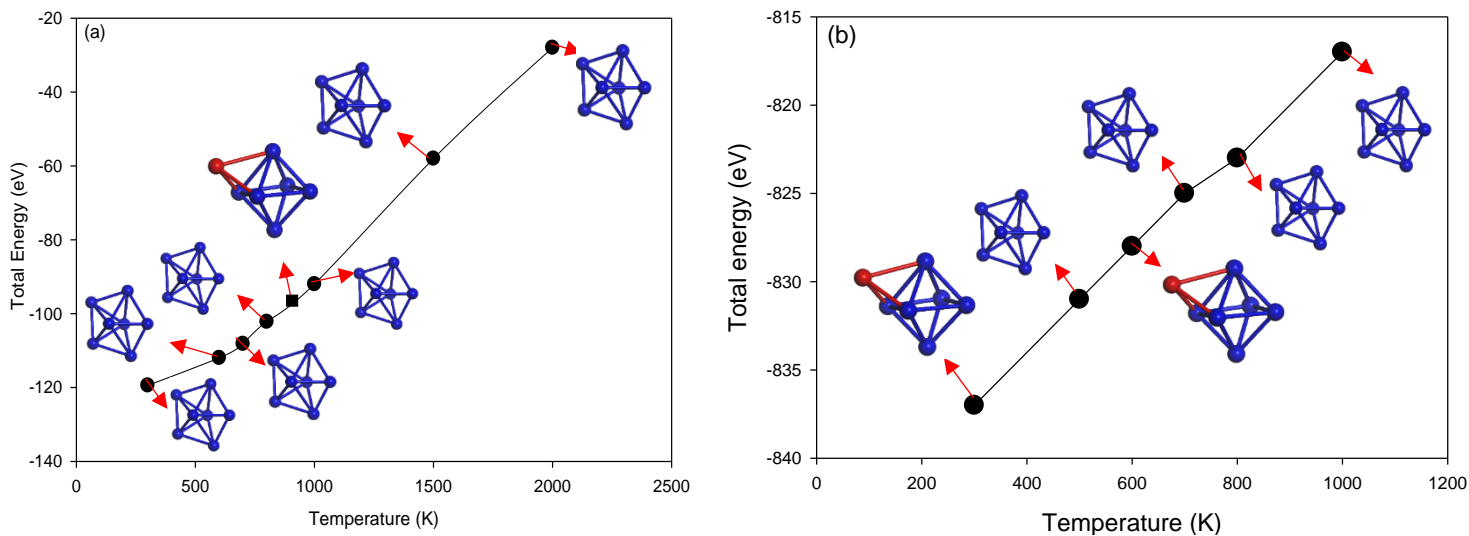
Figure 5.14. Total energy versus temperature for Ti$_7$/LiCl structure for (a) LiCl rigid ion model and (b) LiCl shell model.
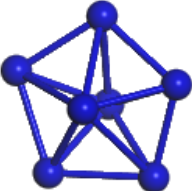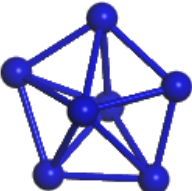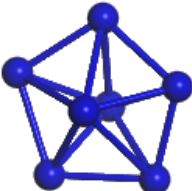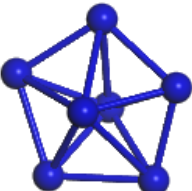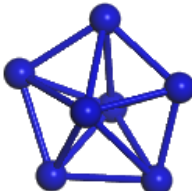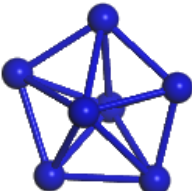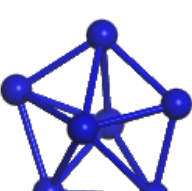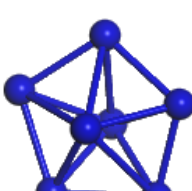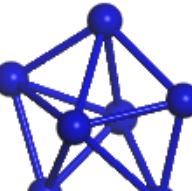
The phase transition as the system transformed from solid to liquid phase for Figure 5.14 (a), is indicated by a change in the trend of the graph from exponential below 1000 K to linear increase above 1000 K and for Figure 5.14 (b) at a slight kink around 700 K. This is an indication of a change in the energy of the system as a result of the motion of atoms. The observation made here agrees well with the observations on the radial distribution functions (Figure 5.7 and 5.8, Figure 5.10 and 5.11), where we observe a possible phase change from a decrease in the peak height as temperature increases.

5.6. Geometry optimisation of Ti_7 cluster using CASTEP and $DMol^3$

The geometry optimisation calculations are performed on the cluster using CASTEP and $DMol^3$ codes. This is done to check the stability of the titanium cluster as a validation to results obtained using D_POLY code (section 5.5). It will be important to know how the Ti_7 cluster geometry responds or change with different codes or approach. Table 5.1 shows the geometry of Ti_7 using LiCl rigid ion model for DL_POLY, CASTEP and $DMol^3$ codes at 300 K – 700 K. We note that the cluster maintains its pentagonal bipyramid geometry across the three codes at that temperature range.

Table 5.2 shows the geometry of Ti_7 using LiCl rigid ion model for DL_POLY, CASTEP and $DMol^3$ codes at 800 K – 1000 K. We observe the pentagonal bipyramid geometry at 800 K. The geometry of the cluster transitions to a capped octahedron at 900 K and back to a pentagonal bipyramid at 1000 K. The cluster transition at 900 K may be attributed to a possible melting temperature.

Table 5.1. The geometry of Ti$_7$ in LiCl rigid ion model using DL_POLY, CASTEP and DMol^3 at 300 K – 700 K.

Temperature (K)	DL_POLY (Rigid ion model)	CASTEP	DMol^3
300 K			
400 K			
500 K			
600 K			
700 K			

Table 5.2. The geometry of Ti$_7$ in LiCl rigid ion model using DL_POLY, CASTEP and DMol^3 at 800 K – 1000 K.
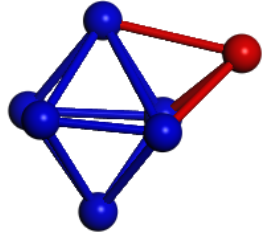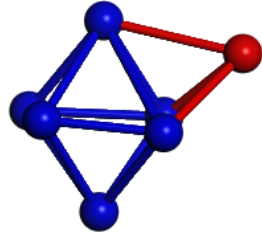
Temperature (K)	DL_POLY (Rigid ion model)	CASTEP	DMol^3
800 K			
900 K			
1000 K			

Figure 5.15 shows the total energy against temperature graph of the Ti$_7$ cluster from DL_POLY rigid ion model results using CASTEP and DMol^3 codes. The CASTEP and DMol^3 curves on the graph indicate the geometry optimisation results obtained using these codes. Single-point energies were calculated to investigate if some of the geometry optimisation results will be obtained in single-point calculations. The pentagonal bipyramid

geometry of Ti$_7$ gives lower energies (shown by the constant straight line in the CASTEP

and DMol^3 curves) for both codes confirming that it is the stable geometry of Ti$_7$ cluster.
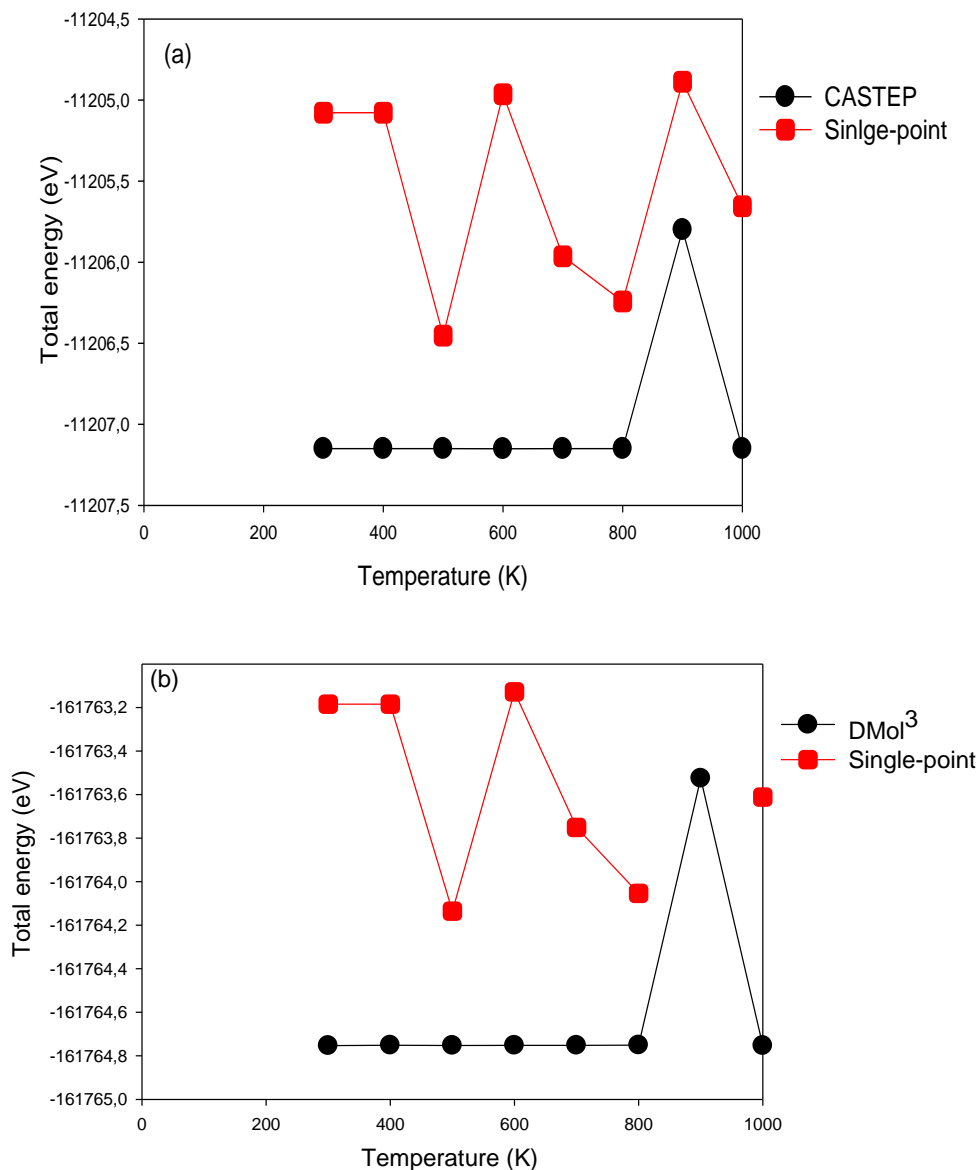
Figure 5.15. Total energy against temperature for (a) CASTEP and (b) DMol^3 energies for Ti$_7$ cluster.

Table 5.3 shows a comparison of the cluster geometry at 300 K – 700 K from the DL_POLY

shell model results using CASTEP and DMol^3 codes. At 300 K – 400 K the cluster has the
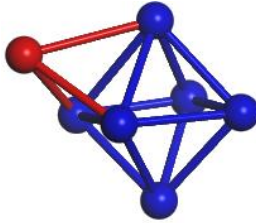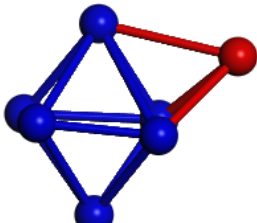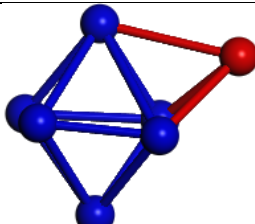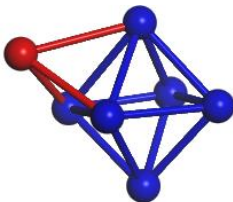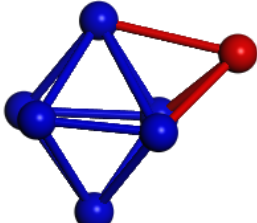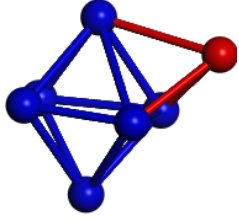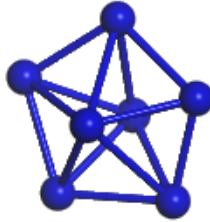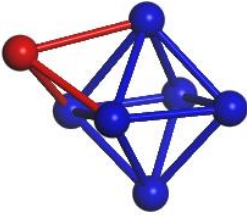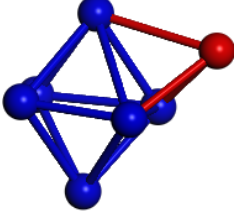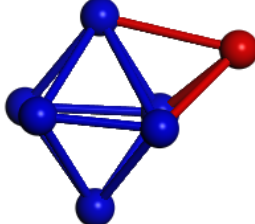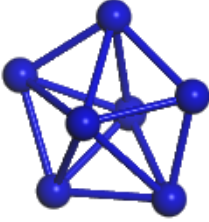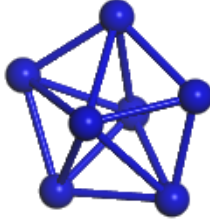
capped octahedron geometry for all three codes but at different orientations for CASTEP and DMol^3 code. At 500 K the cluster retains its pentagonal bipyramid geometry before transitioning to a capped octahedron at 600 K. At 700 K the cluster transitions back to a pentagonal bipyramid.

Table 5.4 shows the cluster geometry at 800 K – 1000 K from the DL_POLY shell model results using CASTEP and DMol^3 codes. We observe the pentagonal bipyramid geometry at 800 K for all computational codes. At 900 K, the cluster on the DL_POLY column shows a capped octahedron geometry, and the CASTEP calculations show the pentagonal bipyramid geometry, suggesting that in DFT calculations the cluster is stable at 900 K. The pentagonal bipyramid geometry is observed again at 1000 K for all codes used. Furthermore, the CASTEP and DMol^3 graphs show similar trends confirming this observation.
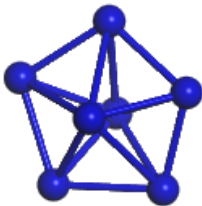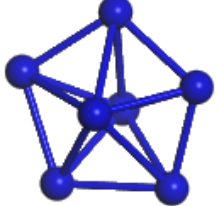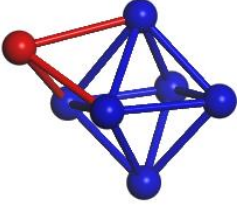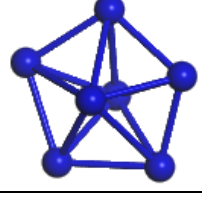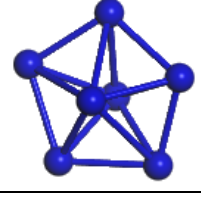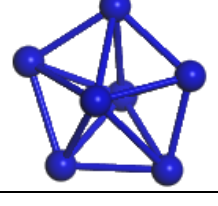
Figure 5.16 shows the total energy against temperature graph of the Ti$_7$ cluster from DL_POLY shell model results using CASTEP and DMol^3 codes. It is clearly seen that the pentagonal bipyramid geometry of Ti$_7$ gives low energies for both codes at high temperature (CASTEP and DMol^3 curves). The low energies indicate the stability of the cluster.

Table 5.3. The geometry of Ti$_7$ in LiCl shell model using DL_POLY, CASTEP and DMol^3 at 300 K – 700 K.

Temperature (K)	DL_POLY (Shell model)	CASTEP	DMol^3
300 K			
400 K			
500 K			
600 K			
700 K			

Table 5.4. The geometry of Ti_7 in LiCl shell model using DL_POLY, CASTEP and DMol^3 at 800 K – 1000 K.

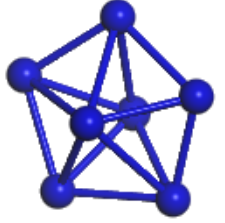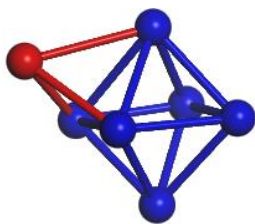| Temperature (K)	DL_POLY (Shell model)	CASTEP	DMol^3
800 K			
900 K			
1000 K			

Figure 5.16. Total energy against temperature for (a) CASTEP and (b) DMol^3 energies for Ti$_7$ cluster.

Chapter 6

The influence of temperature on TiCl$_n$ and Ti$_7$/TiCl$_n$ structures

In this chapter, we present molecular dynamics results on the elastic properties, mechanical stability and temperature dependence of the TiCl, TiCl$_2$ and TiCl$_4$ structures. Firstly, the elastic stability of the structures is discussed. Secondly, interatomic potential parameters for describing the Ti-Cl interaction were adopted from those derived in chapter 4. These interatomic potential parameters are used to describe Ti$_7$/LiCl interactions. The GULP code [21] was used to validate the TiCl, TiCl$_2$ and TiCl$_4$ structures. Their lattice parameters, bond lengths, elastic and mechanical stability will be discussed. Thirdly, the ion diffusion (DC) capabili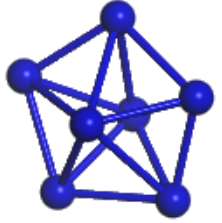ties and radial distribution functions (RDF) are discussed to evaluate the TiCl and TiCl$_2$ interactions. These properties were calculated to check the transferability of the Ti-Cl potential parameters. This will assist in understanding the titanium production process, particularly how titanium evolved in the presence of TiCl and TiCl$_2$ salt medium. Lastly, we investigate the entropy and Gibbs free energy to evaluate the possible phase transitions that may occur for the LiCl (rigid ion and shell models) and TiCl$_n$ structures within the rigid ion model.

6.1. TiCl$_n$ structures

Figure 6.1 shows the atomic arrangement per unit cell of TiCl, TiCl$_2$ and TiCl$_4$ structures. The TiCl$_n$ structures were subjected to full geometry optimisation using the GULP code, and the results are summarised in Table 6.1.

The TiCl structure (Figure 6.1 (a)) crystallises in a cubic system with an Fm-3m space group, internal coordinates at Ti (0, 0, 0) Cl (1/2, 1/2, 1/2) and equilibrium lattice parameter a= 4.276 Å. The Ti atoms are in an octahedral position in the middle of the cell edges and the centre of the cell. Titanium and chloride atoms touch each other along the cell edges. The unit cell contains four titanium atoms and four chloride atoms [134, 135].

TiCl$_2$ has a trigonal P-3m1 space group with equilibrium structural parameters a=b= 2.651 Å and c= 7.127 Å as shown in Figure 6.1 (b). The atomic positions are described as Ti (0, 0, 0), Cl (2/3,1/3,1/3) and Cl (1/3,2/3,2/3). The coordination of the Ti atoms is close to a regular octahedron. Also, the Ti and Cl atoms are arranged in hexagonal layers [136], and the structure consists of three atoms per unit cell.

The TiCl$_4$ structure (Figure 6.1 (c)) crystallises in a monoclinic crystal structure with a P2$_1$/c space group and has a tetrahedral shape [137]. The equilibrium structural parameters are a= 6.304 Å, b= 4.032 Å and c= 6.390 Å. The internal coordinates for this structure are at Ti (0.251, 0.077, 0.133), Cl (0.190, 0.392, 0.077), Cl (0.077, -0.083, 0.196), Cl (0.307, -

0.080, -0.045) and Cl (0.431, 0.075, 0.309). The structure consists of five atoms per unit cell.

(a) (b) (c)
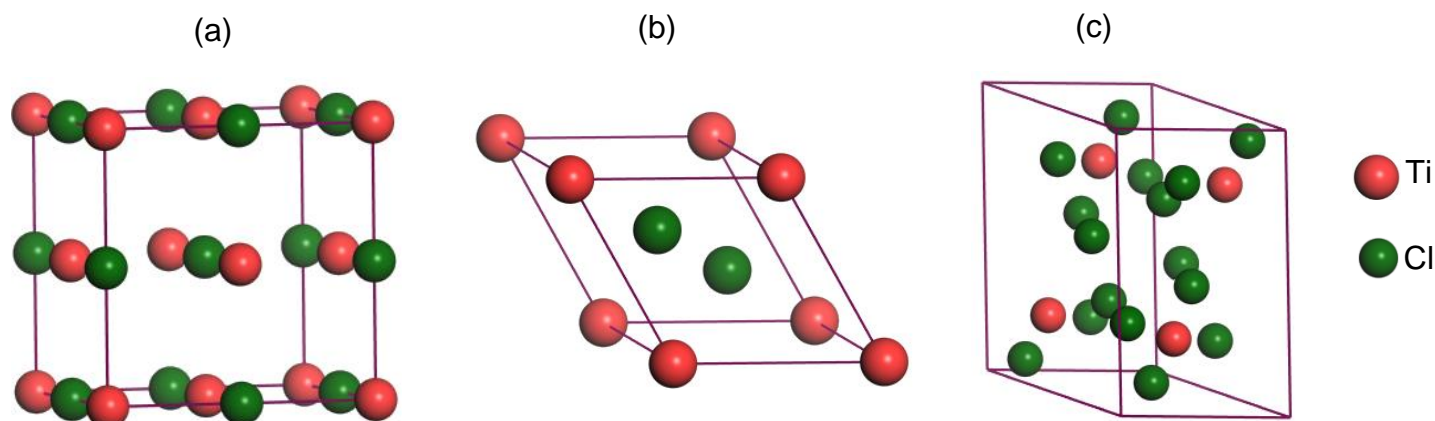
Figure 6.1. The unit cells of (a) TiCl, (b) $TiCl_2$ and (c) $TiCl_4$ structures.

The lattice parameters show good agreement to the available experimental data to within 5%. More importantly, note that the geometric symmetry of these systems was preserved during optimisation. In order to validate the structures, we have examined the Ti-Cl bond length for each structure. The equilibrium Ti-Cl bond length is comparable with the available experimental values (Table 6.1). It is clearly seen that the Ti-Cl bond length is well reproduced to within 5% and 1% for TiCl and $TiCl_4$ systems, respectively. The short Ti-Cl bond length in $TiCl_2$ suggests a strong interaction between the Ti and Cl atoms. We note that the Ti atoms in the $TiCl_n$ structures do not form a bond; hence Ti-Ti bond length is not observed. Also, the Ti-Ti (2.503 Å) bond length of the Ti_7 cluster compares well with the experimental value of 1.943 Å [138] for titanium dimer (Ti_2). It should be noted that the bond length for a cluster depends on the size of the cluster.

Table 6.1. The calculated (Calc.) and experimental (Exp.), lattice parameters, bond lengths for TiCl, TiCl$_2$ and TiCl$_4$ structures. The (–) implies that there is no bonding.

Structure		Lattice parameters			Ti-Cl bond length (Å)	
		a (Å)	b (Å)	c (Å)	Calc.	Exp.
TiCl		4.276	4.276	4.276	2.138	2.264 [139]
TiCl$_2$	Calc.	2.651	2.651	7.115	1.878	–
	Exp.[a]	3.561	3.561	5.875		
TiCl$_4$	Calc.	6.304	4.032	6.390	2.165	2.170 [140]
	Exp.[b]	9.670	6.474	9.682		

[a] is ref [141], [b] is ref [142]

The elastic properties were calculated to observe the stability of the systems. Note that the cubic crystal system has three independent elastic constants which are C_{11}, C_{12} and C_{44}. Accordingly, the mechanical stability criteria for the cubic crystal is [135, 143]:

$$C_{11} > 0, C_{11} - C_{12} > 0, C_{11} + 2C_{12} > 0, C_{44} > 0, C_{11} > B > C_{12}, \tag{6-1}$$

for the trigonal crystal system is [135, 143]:

$$C_{11} > |C_{12}|, C_{44} > 0, C^2{}_{13} < \frac{1}{2}C_{33}(C_{11} + C_{12}), C^2{}_{14} < \frac{1}{2}C_{44}(C_{11} - C_{12}) \equiv C_{44}C_{66}, \tag{6-2}$$

and for the monoclinic system is [144]:

$$C_{ii} > 0 \ (i = 1 - 6), [C_{11} + C_{22} + C_{33} + 2(C_{12} + C_{13} + C_{23})] > 0, (C_{33}C_{55} - C^2{}_{35}) > 0,$$

$$(C_{44}C_{66} - C^2{}_{46}) > 0, (C_{22} + C_{33} - 2C_{23}) > 0,$$

$$[C_{22}(C_{33}C_{55} - C^2{}_{35}) + 2C_{23}C_{25}C_{35} - C^2{}_{23}C_{55} - C^2{}_{25}C_{33}] > 0,$$

$$\{2[C_{15}C_{25}(C_{33}C_{12} - C_{13}C_{23}) + C_{15}C_{35}(C_{22}C_{13} - C_{12}C_{23}) + C_{25}C_{35}(C_{11}C_{23} - C_{12}C_{13})] -$$

$$[C^2_{15}(C_{22}C_{33} - C^2_{23}) + C^2_{25}(C_{11}C_{33} - C^2_{13}) + C^2_{35}(C_{11}C_{22} - C^2_{12})] + C_{55}g\} > 0 \quad (6\text{-}3)$$

The other important parameter is the bulk (B), shear (G) and Young's (E) moduli. These parameters were obtained from the Voigt-Reuss-Hill approximation [145]. For a cubic system [144, 145],

$$B_{voigt} = B_{Reuss} = \frac{1}{3}(C_{11} + 2C_{12}),$$

$$G_{voigt} = \frac{1}{5}(C_{11} - C_{12} + 3C_{44}), \quad G_{Reuss} = \frac{5(C_{11}-C_{12})C_{44}}{[4C_{44}+3(C_{11}-C_{12})]} \quad\quad (6\text{-}4)$$

for the trigonal system (with a hexagonal layer) [144, 145]:

$$B_{voigt} = \left(\frac{1}{9}\right)[2(C_{11} + C_{12}) + 4C_{13} + C_{33})], \quad B_{Reuss} = \frac{C^2}{M}$$

$$G_{voigt} = \left(\frac{1}{30}\right)(M + 12C_{44} + 12C_{66}), \quad G_{Reuss} = \frac{(5/2)[C^2C_{44}C_{66}]}{[3B_{voigt}C_{44}C_{66}+C^2(C_{44}C_{66})]}$$

$$M = C_{11} + C_{12} + 2C_{33} - 4C_{13}, \quad C^2 = (C_{11} + C_{12})C_{33} - 2C^2_{13} \quad\quad (6\text{-}5)$$

For a monoclinic system [144, 145]:

$$B_{voigt} = \left(\frac{1}{9}\right)[C_{11} + C_{22} + C_{33} + 2(C_{12} + C_{13} + C_{23})],$$

$$B_{Reuss} = \Omega[a(C_{11} + C_{22} + 2C_{12}) + b(2C_{12} - 2C_{11} - C_{23}) + c(C_{15} - 2C_{25})$$

$$+ d(2C_{12} + 2C_{23} - C_{13} - 2C_{22}) + 2e(C_{25} - C_{15}) + f]^{-1}$$

$$G_{voigt} = \left(\frac{1}{15}\right)[C_{11} + C_{22} + C_{33} + 3(C_{44} + C_{55} + C_{66}) - (C_{12} + C_{12} + C_{23})],$$

$$G_{Reuss} = 15\left\{\frac{4[a(C_{11}+C_{22}+C_{12})+b(C_{11}-C_{12}-C_{23})+c(C_{15}+C_{15})+d(C_{22}-C_{12}-C_{23}-C_{13})+e(C_{15}-C_{25})+f]}{\Omega} + \right.$$

$$\left. 3\left[\frac{g}{\Omega} + \frac{(C_{44}+C_{66})}{(C_{44}C_{66}-C^2_{46})}\right]\right\}^{-1}$$

$$a = C_{33}C_{55} - C^2_{35}, \quad b = C_{23}C_{55} - C_{25}C_{35}, \quad c = C_{13}C_{35} - C_{15}C_{33}, \quad d = C_{13}C_{55} - C_{15}C_{35},$$

$$e = C_{13}C_{25} - C_{15}C_{23}, \quad f = C_{11}(C_{22}C_{55} - C^2_{25}) - C_{12}(C_{12}C_{55} - C_{15}C_{25}) + C_{15}(C_{12}C_{25} -$$

$$C_{15}C_{22}) + C_{25}(C_{23}C_{35} - C_{25}C_{33}), \quad g = C_{11}C_{22}C_{33} - C_{11}C^2_{23} - C_{22}C^2_{13} - C_{33}C^2_{12} +$$

$$2C_{12}C_{13}C_{23},$$

$$\Omega = 2[C_{15}C_{25}(C_{33}C_{12} - C_{13}C_{23}) + C_{15}C_{35}(C_{22}C_{13} - C_{12}C_{23}) + C_{25}C_{35}(C_{11}C_{23} - C_{12}C_{13})] -$$

$$[C^2_{15}(C_{22}C_{33} - C^2_{23}) + C^2_{25}(C_{11}C_{33} - C^2_{13}) + C^2_{35}(C_{11}C_{22} - C^2_{12})] + gC_{55} \qquad (6\text{-}6)$$

Young's modulus (E) is calculated using: $E = \dfrac{9BG}{(3B+G)}$ $\qquad\qquad$ (6-7)

Table 6.2. Calculated elastic constants (C_{ij}), bulk (B), shear (G), Young's (E) moduli in GPa and the ratio of brittleness/ductility (B/G) for TiCl, TiCl$_2$ and TiCl$_4$ structures.

C_{ij} (GPa)	TiCl	TiCl$_2$	TiCl$_4$
C_{11}	17.570	1556.795	788.412
C_{12}	132.181	-1139.614	162.260
C_{13}	-	0.008	68.927
C_{14}	-	-0.001	-
C_{15}	-	-	87.627
C_{22}	-	-	655.116
C_{23}	-	-	241.912
C_{25}	-	-	-64.298
C_{33}	-	0.192	688.834
C_{35}	-	-	-
C_{44}	132.181	0.004	286.527
C_{46}	-	-	24.642
C_{55}	-	-	257.459
C_{66}	-	1347.735	320.519
$B\left(=\frac{1}{2}(B_{voigt}+B_{Reuss})\right)$	93.977	46.461	341.701
$G\left(=\frac{1}{2}(G_{voigt}+G_{Reuss})\right)$	-176.648	276.559	273.934
$E\left(=\frac{9BG}{(3B+G)}\right)$	-215.774	278.023	596.435
B/G	-0.532	0.168	1.247

In order for the systems to be stable, the above conditions (Equations (6-1), (6-2) and (6-3)) should be satisfied. Table 6.2 presents the calculated elastic constants and moduli for TiCl$_n$ structures. It is clear that the independent C_{ij} for the cubic system (TiCl) satisfies all the stability criteria ($C_{ij} > 0$), which suggests that the structure is elastically stable. The elastic constants show that the Cauchy relation holds for the TiCl cubic structure since the values of C_{12} and C_{44} are equal [120, 121]. However, the trigonal system (TiCl$_2$) displays negative values for C_{12} and C_{14}. This suggests that the structure is elastically unstable since the stability criteria for the trigonal system is not satisfied. The independent C_{ij} for the TiCl$_4$ structure displays a negative value for C_{25}, suggesting that this structure is also elastically unstable. From this observation, it is observed that the TiCl structure is stable compared to the TiCl$_2$ and TiCl$_4$.

Furthermore, to estimate the mechanical stability for these structures, we calculated the bulk, shear and Young's moduli, and the results are listed in Table 6.2. The TiCl$_2$ structure has a higher shear modulus (G) compared to the other structures, which implies that the TiCl$_2$ structure is highly rigid. It is noted that the TiCl$_2$ and TiCl$_4$ structures are mechanically stable ($G > 0$). This indicates that a large force is required to produce deformation on the structure. Also, the ratio of brittleness/ductility (B/G) as proposed by Pugh [146], reveals that the TiCl$_4$ structure has a tendency towards brittleness ($B/G < 1.75$). We are not aware of any experimental or theoretical data for the calculated moduli to compare our results. Thus, we consider the calculated results as prediction study that awaits experimental confirmation.

6.2. Diffusion coefficient for TiCl and TiCl$_2$

In this section, we discuss the diffusion coefficients (DC) of the TiCl and TiCl$_2$ structures. The DC describes how fast one material can diffuse in another material. A higher DC value implies a faster diffusion; otherwise, the diffusivity is low for small DC values [126]. The DC (diffusivity) was determined to understand the movement of Ti and Cl ions as the temperature is increased from low to high temperature range.

Figure 6.2 depicts the diffusion coefficient plot against temperature for TiCl structure. The different diffusivity of Ti and Cl ions are shown. A linear increase in the titanium (Ti) ions mobility is observed from 50 K until 2000 K (Figure 6.2 (a)). At 500 K – 700 K, the DC is almost equal to 27 nm^2/s. We observe kinks at about 900 K, 1100 K and 1300 K, which may suggest the possible phase transitions of titanium to either α-Ti (hcp), bcc (β-Ti) and ω-Ti under pressure. It is known that at ambient conditions the titanium phases reach a transitional temperature at 146 K (ω-Ti), below 1155 K (α-Ti), and above 1155 K for β-Ti [44, 147]. The increase in DC at 1400 K – 1800 K suggests that the structure has transitioned to a possible liquid phase. These predictions are in good agreement with the available theoretical data [44, 147].

Now, in the case of Cl, a linear increase is observed from 50 K – 2000 K (Figure 6.2 (b)). The Cl ions mobility is detected around 50 K, followed by a steady increase up to 800 K. At above 900 K to 2000 K, we observe kinks which suggests less mobility due to strong interactions. This may be attributed to Cl being bonded to Ti (see snapshot).

Figure 6.2 (c) shows a comparison between the Ti and Cl diffusion coefficients on one set of axes. This is done to compare the diffusivity of Ti and Cl ions in the structure. The Ti and Cl curves are almost similar from 50 K – 500 K but with different DC. At 400 K – 500 K, there is a slow variation of the DC, and we observe fluctuations in the diffusion coefficient of Ti and Cl as temperature increases. It is noted that Cl diffuses faster between 500 K and 800 K than Ti, while Ti is favourable beyond 800 K. This could be due to the fact that the molecular weight of Cl is lower than that of Ti and an atom with a lower molecular weight diffuses faster.

Figure 6.2 (d) shows the average diffusion coefficient for Ti and Cl ions. The DC follows the same trend as the chlorine diffusion coefficient graph (Figure 6.2 (b)) at 50 K – 800 K. A small variation of the DC is observed at 900 K – 1050 K followed by a slight increase until 1100 K. However, the diffusion coefficient for Ti-Cl in the TiCl system is linearly increasing than in the single Ti and Cl. This may suggest that Ti influences diffusivity more than Cl. At 1800 K – 2000 K the graph does not change, which indicates it has reached the highest diffusion coefficient at a higher temperature.
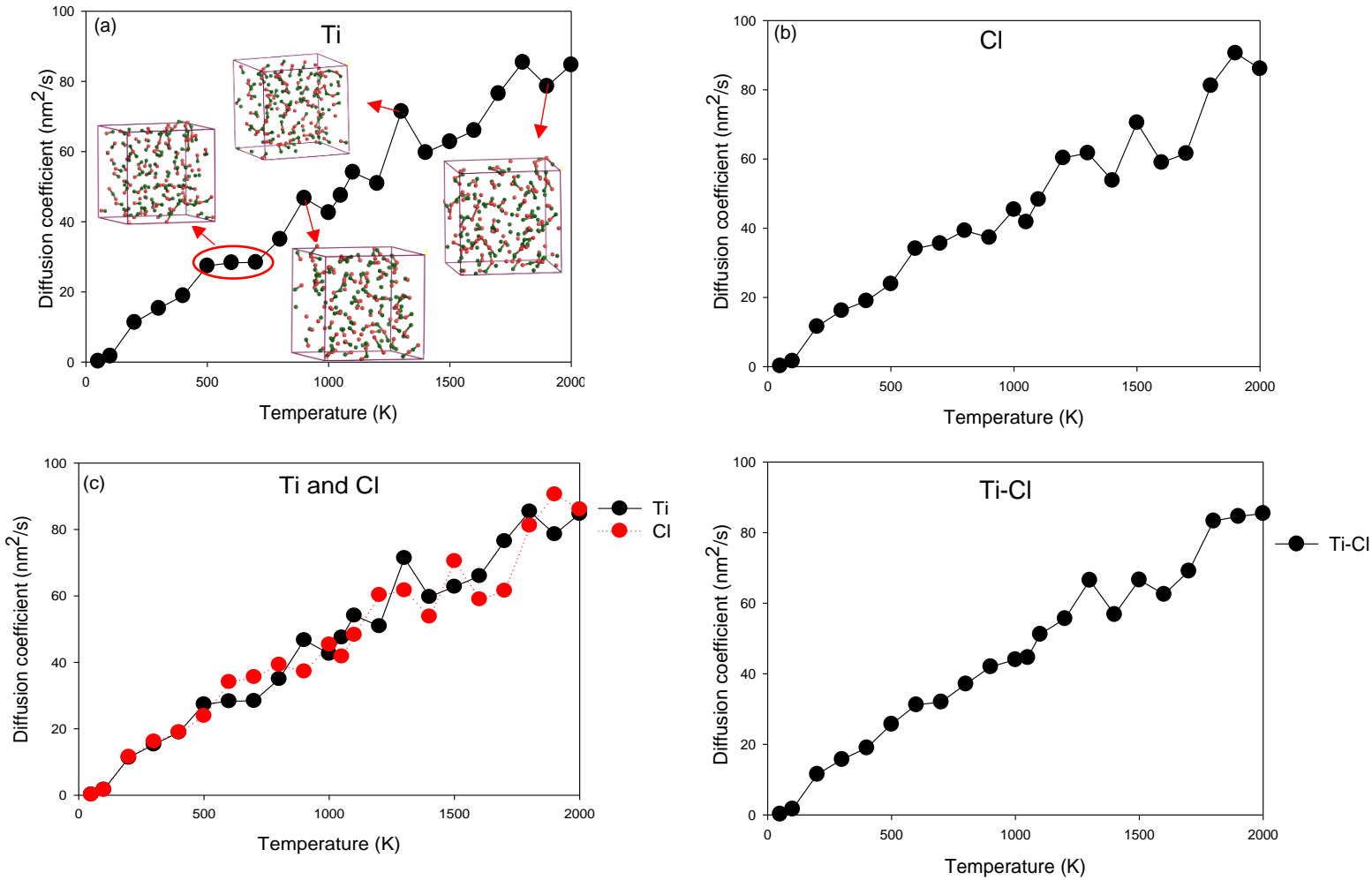
Figure 6.2. Diffusion coefficient graphs for (a) Ti, (b) Cl, (c) comparison between Ti and Cl, (d) average for Ti and Cl ions in TiCl structure (rigid ion model).

Figure 6.3 depicts the diffusion coefficients for $TiCl_2$ structure. Figure 6.3 (a) shows the Ti diffusion in $TiCl_2$ system. The mobility of Ti ions is detected at 50 K – 2000 K. A slow variation of the DC is observed at 50 K until 200 K. At 200 K – 300 K, the DC increases steadily until 300 K followed by a decrease to 400 K. The DC slightly increases from 400 K until 700 K. At 700 K – 800 K, we observe a decrease in the DC and then it increases until 900 K before decreasing until 1000 K. Moreover, the diffusion rate for Ti is not preferential beyond 200 K. This could be due to the weak Ti-Ti interaction for Ti in $TiCl_2$

(short bond distance for Ti-Cl ranging from 1.275 Å to 1.674 Å). This bonding behaviour was evident from the corresponding structure (Figure 6.3 (a)). The Ti and Cl self-diffusion occurs several times as the temperature is increased compared to Li and Cl. A "knee" behaviour is observed at about 300 K, 900 K, 1300 K and 1600 K. Similarly, to the case of NaCl, this behaviour is due to the presence of a "frozen equilibrium" at low and high temperatures [34, 35]. The kinks observed at about 300 K and 900 K may suggest possible α-Ti (hcp) existence, which is a low-temperature phase. We observe a slight increase in DC at 1000 K – 1100 K before decreasing until 1200 K. At 1200 K – 1300 K, the diffusivity sharply increases followed by a decrease until 1400 K. This is followed by a slight increment in the DC up to 1500 K. The DC sharply increases until 1600 K and slightly decreases until 1700 K. We observe kinks at about 1300 K and 1600 K which may suggest possible β-Ti phase transition of titanium. At 1700 K – 1800 K, the DC increases followed by a sharp decrease until 1900 K before increasing until 2000 K. The predictions are comparable with the available theoretical data for titanium [44, 147].

In Figure 6.3 (b), the diffusivity of Cl linearly increases from 50 K – 2000 K. The kinks observed above 300 K indicate that the diffusion coefficient is not favourable above 400 K. The observation suggests that random distribution of Cl increases significantly as temperature is increased. This corresponds to a possible melting process in agreement with the reported melting temperature of Cl at 172 K [148]. At 400 K – 600 K, the DC shows a slight decrease before increasing linearly again until 900 K. The DC decreases at 900 K – 1200 K and linearly increases up to 1400 K. This is followed by a decrease in the DC at 1400 K – 1500 K. At 1500 K – 1600 K, the DC is observed to be equivalent and reaches a

constant value of around 155 nm²/s. The linear increase at 1600 K – 2000 K, suggests another possible phase transition from a liquid phase to a gas phase. This in general shows that DC increases gradually as the temperature increases, however, showing the presence of "frozen equilibrium" at 400 K and 1300 K. These are referred to as "knee" behaviour as previously indicated [34, 35].
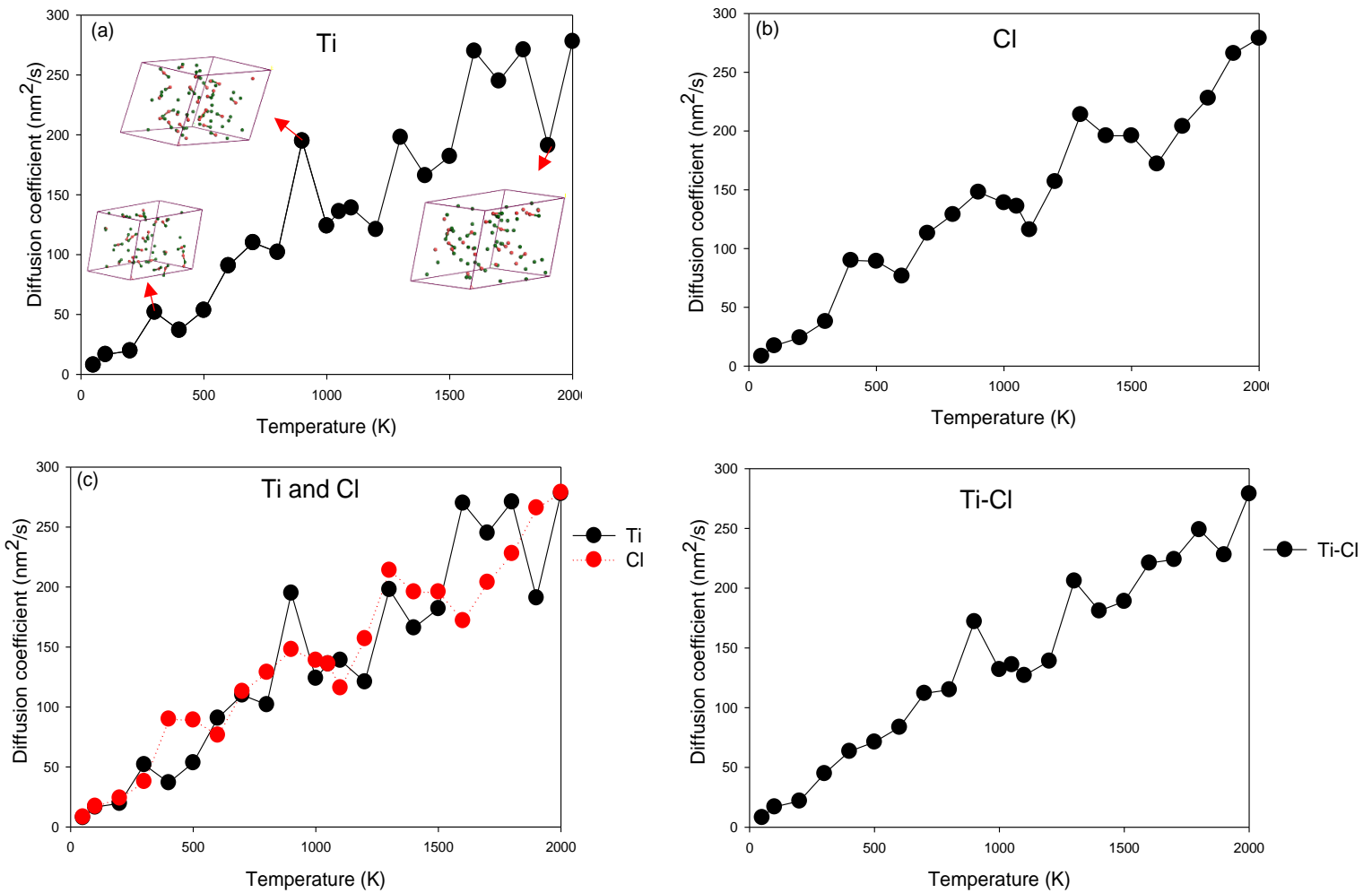
Figure 6.3. Diffusion coefficient graphs for (a) Ti, (b) Cl, (c) comparison between Ti and Cl, (d) average for Ti and Cl ions in TiCl$_2$ structure (rigid ion model).

Figure 6.3 (c) shows a comparison between the Ti and Cl diffusion coefficients. A comparison of the diffusion coefficients for Ti and Cl atoms (Figure 6.2 (c)), shows a linear increase in the DC of both atoms. We note that the DC for Cl is higher between 300 K and 600 K and, between 1100 K and 1500 K. The DC for Ti is favourable at 900 K, and above 1500 K. This is attributed to the molecular weight of the atoms, atoms with a small molecular weight (Cl) diffuse faster. Figure 6.3 (d) shows the average diffusion coefficient for Ti and Cl ions. We note that the diffusion coefficient for Ti-Cl (Figure 6.3 (d)) follows a similar trend as the diffusivity of Ti (Figure 6.3 (a)). However, the diffusion coefficient of Ti-Cl is linearly increasing than in the single Ti and Cl graphs. This clearly shows that Ti promotes DC than Cl.

Figure 6.2 and Figure 6.3 revealed that $DC_{TiCl} < DC_{TiCl_2}$, this could be due to the molecular weight of the structures. $TiCl_2$ has a higher molecular weight than TiCl; thus, diffusivity would be faster in TiCl than $TiCl_2$. The mobility of the ions is not easily detected above 700 K for TiCl and above 800 K for $TiCl_2$ (Figure 6.2 (d) and Figure 6.3 (d)). This may suggest that the atoms are more spread out (not ordered like in a solid) above those temperature ranges. It is clearly shown that Ti promotes diffusivity than Cl in the systems. Furthermore, compared to the LiCl structure, the TiCl structure has a higher diffusion coefficient which may be attributed to the atoms that influence the diffusivity in each case, i.e. Ti and Li; and Li has a smaller molecular weight than Ti.

6.3. Radial distribution functions of $TiCl_n$

This section focuses on TiCl and $TiCl_2$ interactions at different temperatures. Firstly, this is done to validate the transferability of the Ti-Cl potential parameters derived in chapter 4. The interatomic potential parameters were deduced to describe Ti_7/LiCl interactions. Secondly, to also understand the Ti-Ti, Ti-Cl and Cl-Cl interactions of these structures. This is important to gain knowledge of titanium growth which is significant for production processes. Note that in the previous section, the LiCl structure was used to describe the various interactions such as Li-Li, Cl-Cl and Li-Cl. The LiCl structure was chosen to initiate the calculations since it is well known, availability of potential parameters and similar features to TiCl structure. A similar analysis is used to describe $TiCl_n$ systems.

6.3.1. TiCl

Figure 6.4 shows the radial distribution function graphs for TiCl structure. Note that the first peak represents the interatomic bond length for first nearest neighbour atom in the structure. In Figure 6.4 (a), the first peak corresponds to the Ti-Ti bond length (3.08 Å). The peak is highest at low temperatures (g(r) = 8.77 at 50 K) and decreases as the temperature is increased (g(r) = 4.17 at 100 K). At 2000 K, the peak height is reduced to g(r) of 1.22. This value agrees well with the theoretical prediction as reported for TiO_2, which shows the Ti-Ti bond length of ~3.00 Å [149]. Furthermore, the second peak (6.08 Å) corresponds to the second nearest neighbour atom bonded with Ti, which suggests weak interactions.

The Ti-Cl interaction, however, is more orderly as the temperature is increased (Figure 6.4 (b)). A similar trend is observed where the peak decreases with an increase in temperature. The Ti-Cl bond distance is 1.53 Å which is lower compared to the experimental value of 2.264 Å as reported for TiCl [139]. This could be due to an increase in the attraction force between Ti and Cl as temperature increase.

Similarly, the Cl-Cl interaction shows a decrease in the peak height as the temperature is increased (Figure 6.4 (c)). The peak is highest at low temperatures (g(r) = 7.92 at 50 K) and decreases as the temperature is increased (g(r) = 3.82 at 100 K). Furthermore, we note that the peak height is low with g(r) of 1.21 at 2000 K. The calculated Cl-Cl bond length (3.08 Å) agrees well with the theoretical prediction as reported for LiCl system [129], which shows Cl-Cl bond length corresponding to ~3.90 Å. Moreover, the bonds are weak at longer distances (6.08 Å) as indicated by the second peak corresponding to the second nearest neighbour atom bonded with Cl.
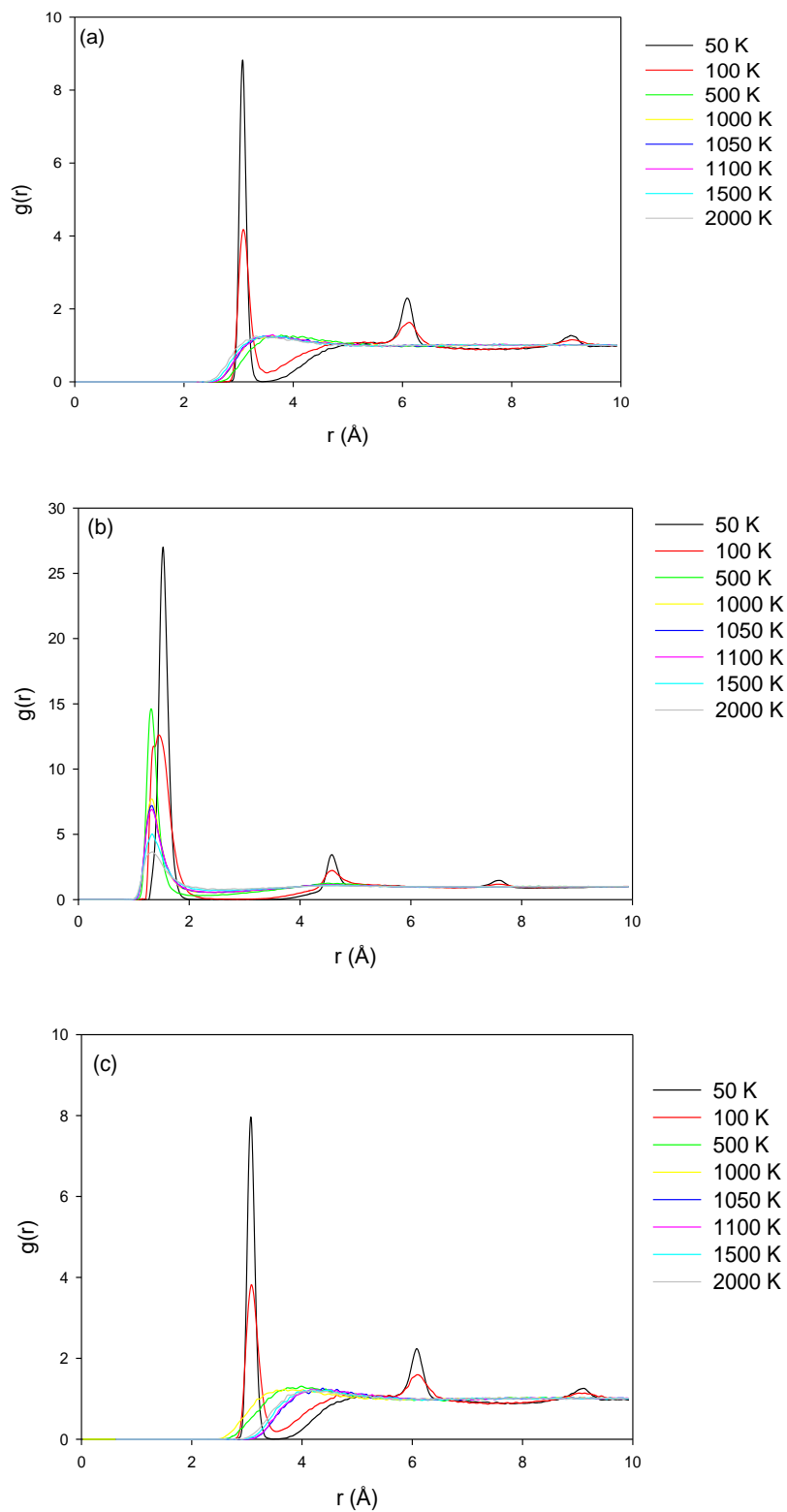
Figure 6.4. Radial distribution function for (a) Ti-Ti, (b) Ti-Cl and (c) Cl-Cl for the TiCl structure (rigid ion model).

6.3.2. TiCl$_2$

In a similar manner, we discuss the RDF for the TiCl$_2$ structure, as shown in Figure 6.5. The first peak in Figure 6.5 (a), corresponds to the Ti-Ti bond length (3.13 Å). This peak is highest at low temperatures (g(r) = 6.60 at 50 K) and decreases as the temperature is increased. For example, at the temperature of 100 K, the peak size is reduced to g(r) of 2.86. At higher temperatures, the peak size is nearly flattened. This agrees well with the theoretical Ti-Ti bond length of ~3.00 Å as reported for TiO$_2$ bulk system [149]. Furthermore, the second peak has a bond length of 6.23 Å which suggests weak interactions at long distances.

The Ti-Cl interactions are shown in Figure 6.5 (b). These are displayed by well-ordered sharp peaks. It is noted that the peak decreases with an increase in temperature from 50 K to 2000 K. The Ti-Cl bond distance is predicted to be 1.43 Å which is lower compared to the 2.232 Å as reported theoretically for TiCl$_2$ [150]. This difference in bond lengths may be due to the interatomic potential parameters adopted, resulting in a strong force of attraction between Ti and Cl.

Likewise, the Cl-Cl interaction with a bond length of 2.38 Å showed a decreasing trend as the temperature is increased (Figure 6.5 (c)). The peak is highest at low temperatures (g(r) = 7.43 at 50 K) and decreases as temperature is increased (g(r) = 6.98 at 100 K). Also, the peak height is low with g(r) of 1.12 at high temperature (2000 K). The calculated bond length agrees well with the Cl-Cl theoretical prediction of ~3.90 Å as reported for LiCl

system [129]. Furthermore, the second peak indicates the second nearest neighbour atom bonded with Cl suggesting weak bonds at longer distances of 5.98 Å. It is clear from the RDF analysis that the interactions on TiCl and $TiCl_2$ are slightly different.
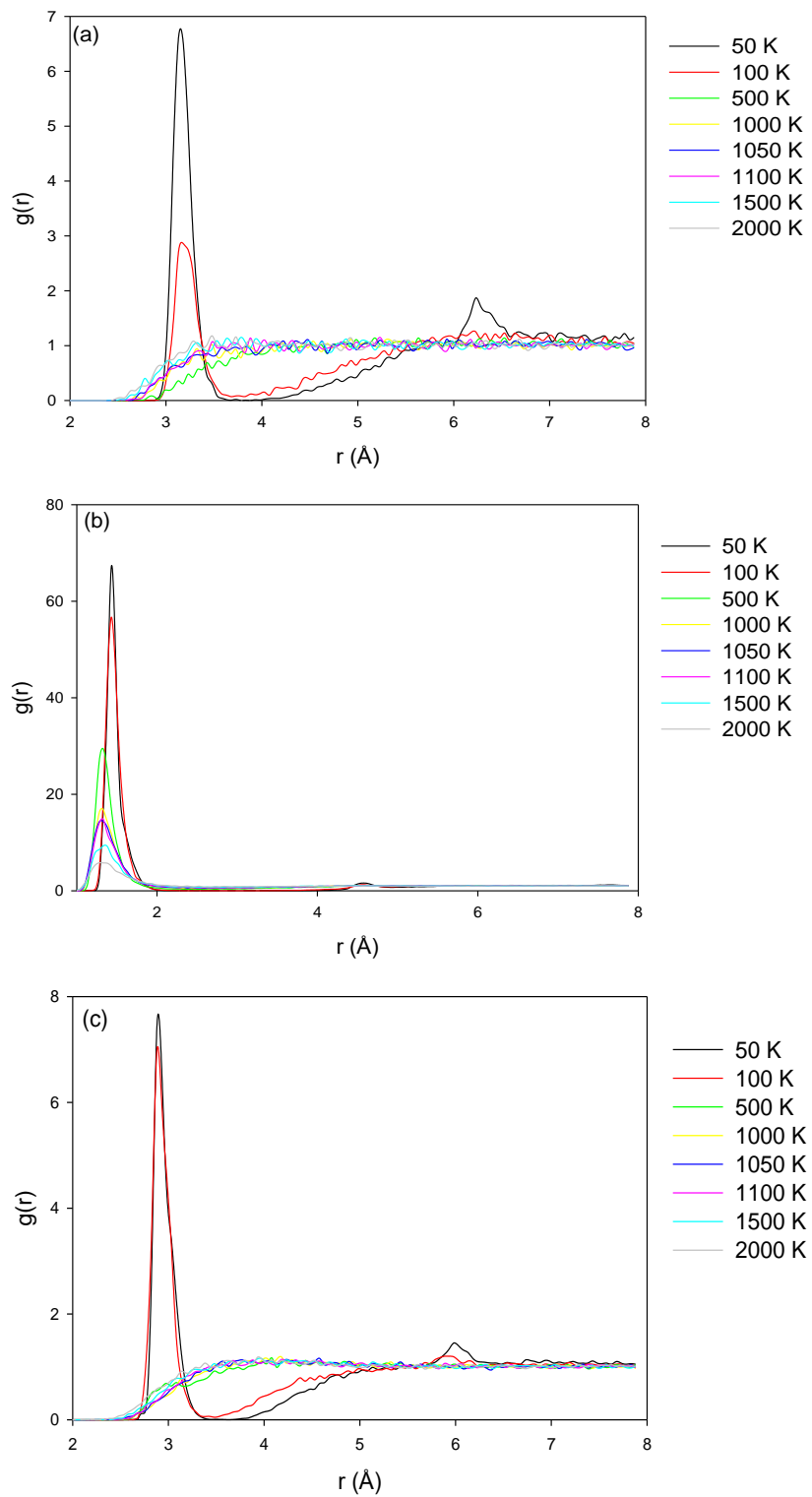
Figure 6.5. Radial distribution function for (a) Ti-Ti, (b) Ti-Cl and (c) Cl-Cl for the TiCl₂ structure (rigid ion model).

6.4. Temperature dependence of TiCl$_n$

In this section, we analyse the total energy of the TiCl and TiCl$_2$ structures at various temperatures. This is done to understand how temperature will influence the stability of the systems and to provide insight into the behaviour of the systems. It is clearly seen that the total energy of each atom increases as the temperature is increased, and this results in an increase in the movement of atoms in each structure. Figure 6.6 shows the total energy versus temperature graphs for TiCl and TiCl$_2$ structures.

Figure 6.6 (a) shows the total energy versus temperature graph for TiCl structure. It is observed that the graph increases linearly as the temperature is increased up to 2000 K. The TiCl structure showed stability at lower temperature and higher temperature range below 1000 K. It is clearly seen that the total energy increases as temperature increased, implying that the structure becomes less stable at higher temperatures. However, at 700 K we observe a kink in the total energy which suggests a possible phase transition from solid to liquid phase in agreement with the DC graphs where we observed the melting temperature at 700 K as discussed above in section 6.2 (Figure 6.2).

Figure 6.6 (b) shows the total energy versus temperature graph for the TiCl$_2$ structure. The graph shows a linear increase in total energy as the temperature is increased. We note positive total energy values above 800 K, which suggests that the structure is unstable at high temperatures. More importantly, we observe a possible phase transition at 400 K. This observation agrees well with the trend on the radial distribution function curves (Figure

6.4 and 6.5), where we observed a decrease in the peak height and broadening of the peaks as temperature increases suggesting a phase change.
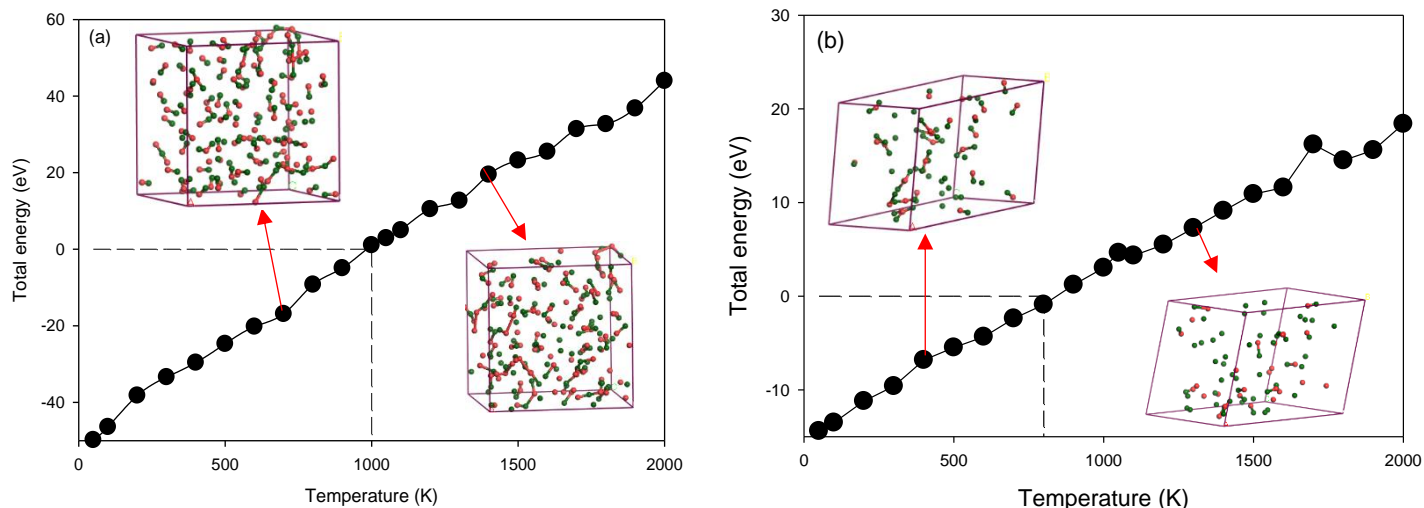
Figure 6.6. Total energy versus temperature graph for (a) TiCl and (b) $TiCl_2$ structures (rigid ion model). The dashed line indicates the stable region ($E_{tot}<0$).

Furthermore, we note that TiCl is more energetically favourable as the temperature is increased compared to the $TiCl_2$ structure. This is indicated by the low total energies depicted on the graph suggesting stability which is lowest for TiCl than $TiCl_2$. Therefore, we can deduce that the TiCl system is more stable and preferred since it displays the lowest energy.

6.5. Diffusion coefficient for $Ti_7/TiCl_n$ structures

This section focuses on the interaction of TiCl and $TiCl_2$ with the Ti_7 cluster. We evaluate the diffusion coefficient of $Ti_7/TiCl$ and $Ti_7/TiCl_2$ systems to check the motions of ions,

particularly, to gain an understanding of how the Ti_7 cluster interacts with the TiCl and $TiCl_2$ salt mediums. This is an aspect that is crucial to the growth of Ti metal during production processes.

Figure 6.7 depicts the diffusion coefficient for Ti_7/TiCl structure at temperatures from 50 K – 2000 K. We show the different interactions for Ti, Cl and Ti_7 cluster. The mobility of the Ti ions is detected from 50 K, where a linear increase in the diffusivity is observed until 200 K (Figure 6.7 (a)). A small kink at 400 K and 800 K corresponds to the transition into an α-Ti, which is a low-temperature phase of titanium. The kinks observed at 1050 K – 1400 K, may be due to the transition of hcp (α-Ti), fcc (ω-Ti) and bcc (β-Ti) phases. This agrees well with the available experimental data [44, 147]. At 1900 K, we observe an indication of phase transformation from solid to liquid, which is in agreement with the reported melting temperature of 1941 K [151].

In Figure 6.7 (b) we observe a linear increase in the diffusivity of the Cl ions from 50 K – 2000 K. A kink at 200 K correspond to a possible melting process in agreement with the Cl melting temperature of 172 K [148]. We also note that the Cl diffusivity is not favourable above 900 K which may suggest that the system is destroyed at that temperature range. Figure 6.7 (c) shows the diffusion coefficient of the titanium (Ti_7) cluster. The DC increases exponentially from 50 K – 2000 K. We note that the mobility of Ti_7 ions is detected at 700 K and increases up to 2000 K.

Figure 6.7 (d) shows a comparison between the diffusivity of Ti, Cl and Ti_7 at the temperature range of 50 K – 2000 K. The Ti and Cl diffusivity are nearly similar at 50 K – 2000 K, while the Ti_7 diffusivity increases at higher temperatures. A slight shift in the Ti_7 ions is observed at 700 K, and the DC increases until 2000 K, following a similar trend as discussed in Figure 6.7 (c). We note that the DC is promoted by Ti_7 cluster than Ti and Cl.
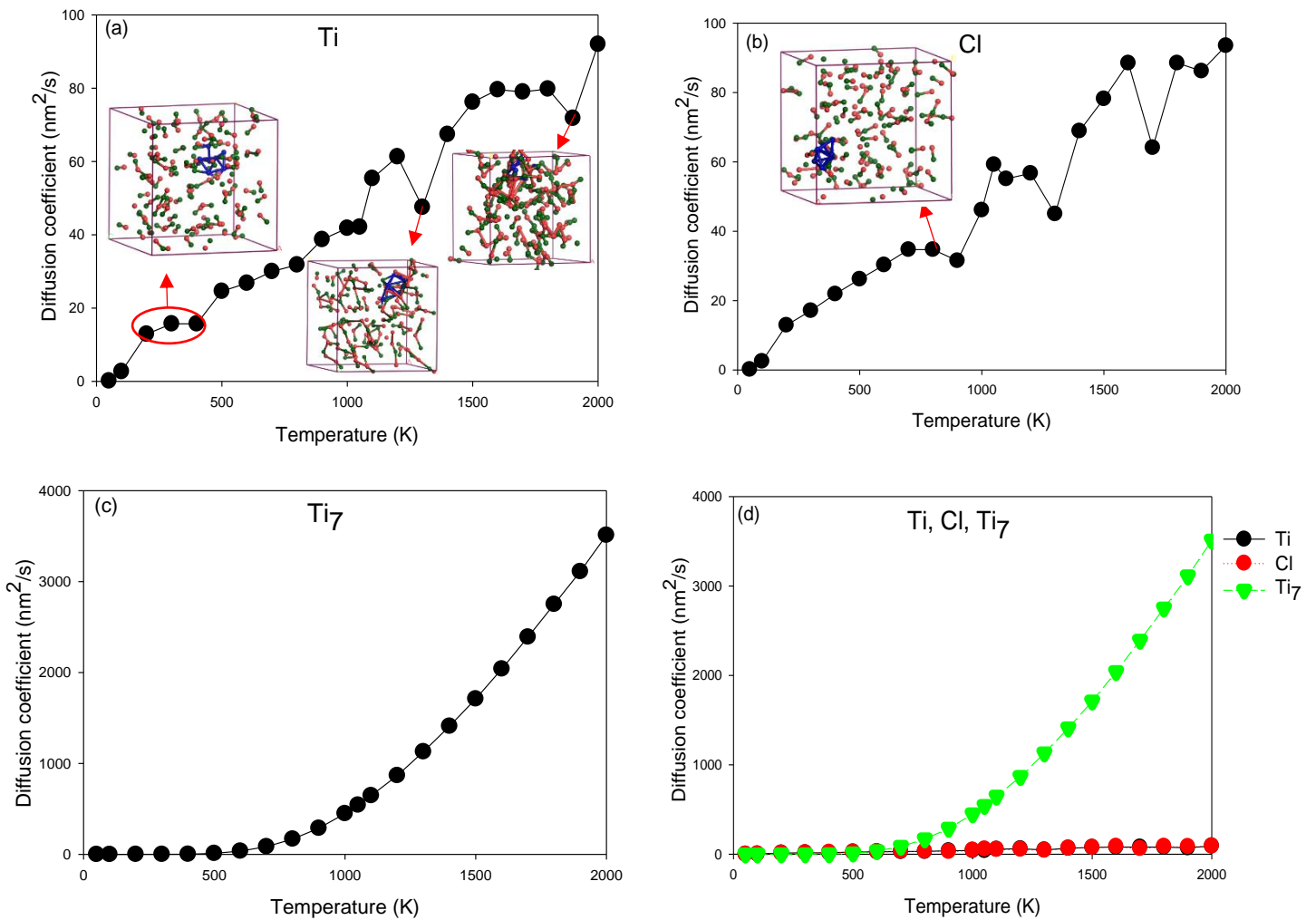
Figure 6.7. Diffusion coefficient for (a) Ti, (b) Cl, (c) Ti_7 and (d) comparison between the Ti, Cl, Ti_7 diffusions in Ti_7/TiCl structure (rigid ion model). The insert structures are shown for a specific temperature range.

Figure 6.8 depicts the diffusion coefficient for $Ti_7/TiCl_2$ structure at temperatures from 50 K – 2000 K. The diffusion coefficient for Ti in $Ti_7/TiCl_2$ system is shown in Figure 6.8 (a). At 400 K and 1000 K, we observed kinks suggesting the presence of a possible low-temperature phase of titanium α-Ti (hcp). Moreover, at 1000 K – 1800 K, we observe a kink corresponding to a possible phase transition from α-Ti to higher temperature β-Ti and ω-Ti in agreement with available experimental data [44, 147]. Comparingly, we observe a possible indication of melting temperature at 1600 K, which is lower than the reported Ti melting temperature of 1941 K [151]. This may be attributed to weak bonding between Ti and Cl (see snapshot).

In Figure 6.8 (b) we observe a linear increase in the diffusivity of the Cl ions from 50 K – 2000 K. At 400 K – 500 K, we observe a slow variation in the DC. The diffusion coefficient is not favourable above 500 K, and this agrees with the reported melting temperature of 172 K [148] for chlorine. This may suggest that at temperatures above 500 K, the system may have collapsed. The titanium cluster (Ti_7) graph indicated in Figure 6.8 (c), shows an exponential increase in diffusivity. Also, the mobility of Ti_7 ions is detected at 400 K and increases exponentially until 2000 K.

Figure 6.8 (d) shows a comparison between the Ti, Cl and Ti_7 diffusion coefficient at the temperature range of 50 K – 2000 K. At 50 K – 500 K, the Ti and Cl graphs display similar trend, where the diffusivity of Ti_7 is detected at 500 K. A shift in the Ti DC is observed at 600 K, and the graphs follow the same trend as discussed in Figure 6.8 (a) and (b). This observation clearly indicates that the Ti_7 cluster mobility is higher compared to Cl and Ti.
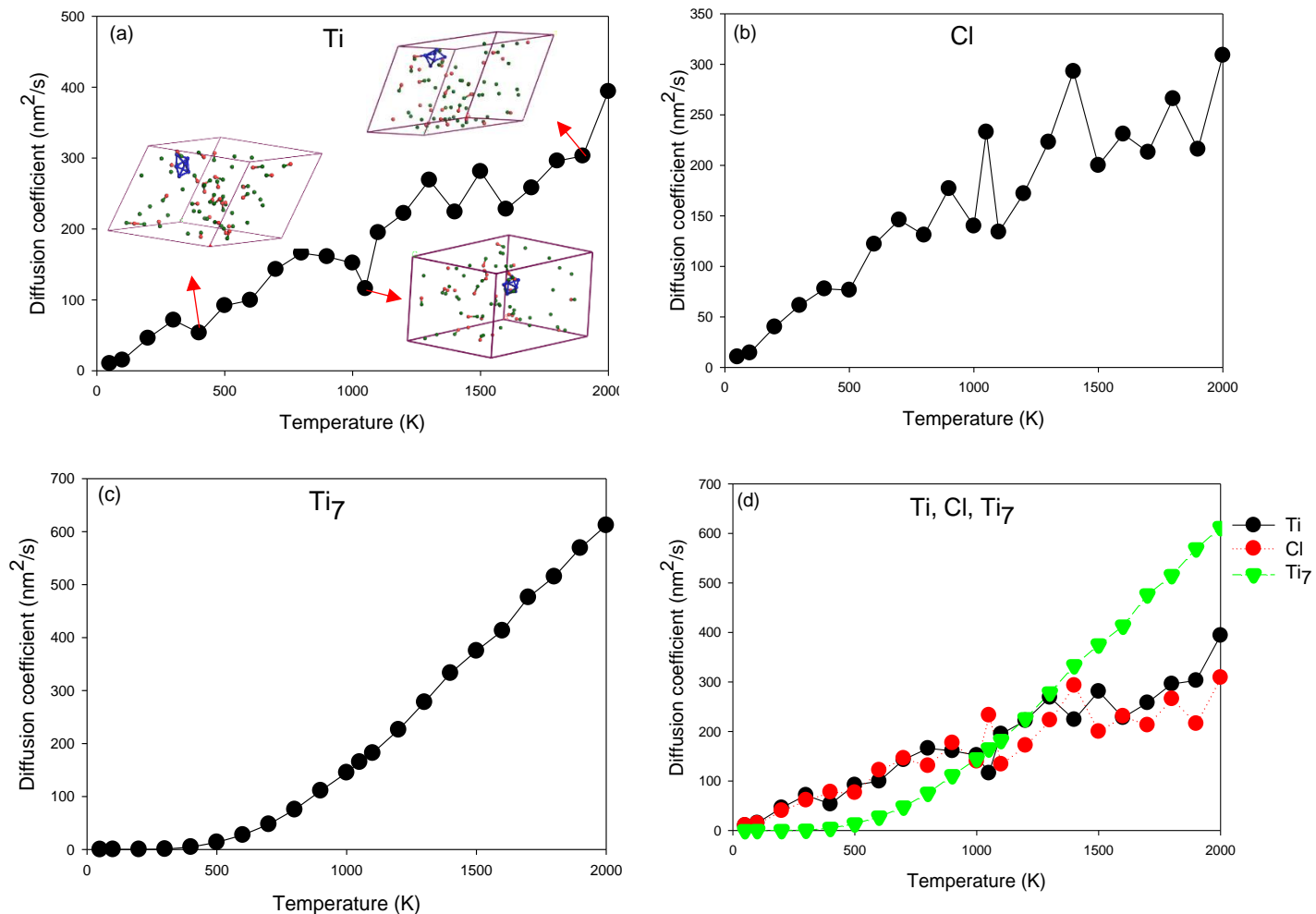
Figure 6.8. Diffusion coefficient for (a) Ti, (b) Cl, (c) Ti$_7$ and (d) comparison between the Ti, Cl, Ti$_7$ diffusions in Ti$_7$/TiCl$_2$ structure (rigid ion model).

The diffusion coefficients in the Ti$_7$/TiCl and Ti$_7$/TiCl$_2$ systems is higher than in the TiCl and TiCl$_2$ structures. This indicates that the cluster (Ti$_7$) promotes diffusivity in the systems differently. We also note that the Ti$_7$/TiCl has a higher diffusion coefficient than the Ti$_7$/LiCl system (chapter 5, section 5.4). This could be as a result of Ti and Li ions since Li has a lower molecular weight compared to Ti; thus, it will diffuse faster.

6.6. Radial distribution functions of interactions in Ti$_7$/TiCl and Ti$_7$/TiCl$_2$ systems

In this section, we discuss the interactions of titanium cluster (Ti$_7$) with TiCl and TiCl$_2$ mediums at varied temperatures from 50 K – 2000K. This is done to evaluate the interactions of the cluster (Ti$_7$) in TiCl and TiCl$_2$ (rigid ion model) at higher temperatures.

6.6.1. Ti$_7$/TiCl

Figure 6.9 shows the radial distribution function for Ti$_7$/TiCl (rigid ion model). In Figure 6.9 (a), the first peak corresponds to the Ti-Ti bond length (3.48 Å). This bond length agrees well with the Ti-Ti theoretical prediction of ~3.00 Å as reported for TiO$_2$ system [149]. The RDF peak is highest at low temperatures (g(r) = 8.13 at 50 K) and decreases as temperature is increased (g(r) = 4.05 at 100 K). At 2000 K, the peak height is reduced with g(r) of 1.24. The second peak (6.08 Å) shows that the interactions are weak at longer radial distances.

The Ti$_7$-Ti$_7$ interaction (Figure 6.9 (b)) however, is more orderly as the temperature increases with the bond length corresponding to 2.63 Å. At 50 K, the peak is at its highest (g(r) = 1440.00) and decreases as temperature increases (g(r) = 639.00 at 500 K). The peak height is low with g(r) of 1.51 at 2000 K. This value agrees well with the theoretically predicted Ti$_7$-Ti$_7$ bond length of 2.63 Å as reported for a capped octahedron Ti$_7$ cluster [55]. Furthermore, the second (2.93 Å) and third peaks (4.33 Å) corresponds to the second

nearest neighbour, and third nearest neighbour atoms bonded with Ti$_7$, suggesting weak interactions. A similar trend is observed for the Ti-Cl interaction (Figure 6.9 (c)), where the peak decreases with increase in temperature. The Ti-Cl bond distance is 1.33 Å which is lower compared to the experimental value of 2.264 Å as reported for TiCl [139].

Figure 6.9 (d) shows the Ti-Ti$_7$ interaction, and the first peak is observed at 0.13 Å and the highest g(r) = 1.99. The Cl-Ti$_7$ interaction (Figure 6.9 (e)) depicts the bond length corresponding to 0.18 Å and g(r) = 3.08. The sharp peaks at low radial distances suggest strong short-range interactions and well-defined structures. This is similar to the observations reported by Terban *et al.* [152] for the terbium (III) ions in layered nanocrystalline phosphate-phosphate.

Likewise, the Cl-Cl interaction shows a decreasing trend as the temperature is increased (Figure 6.9 (f)). The peak is highest at low temperatures (g(r) = 7.30 at 50 K) and decreases as temperature is increased (g(r) = 3.65 at 100 K). At 2000 K, the peak height is low with g(r) of 1.11. The Cl-Cl bond length corresponds to 3.08 Å, and this value agrees well with the theoretical Cl-Cl (~3.90 Å) prediction for LiCl system [129]. Furthermore, the bonds are weak at longer distances (5.38 Å and 8.58 Å) indicated by the second and third peaks corresponding to the second and third nearest neighbour atom bonded with Cl.
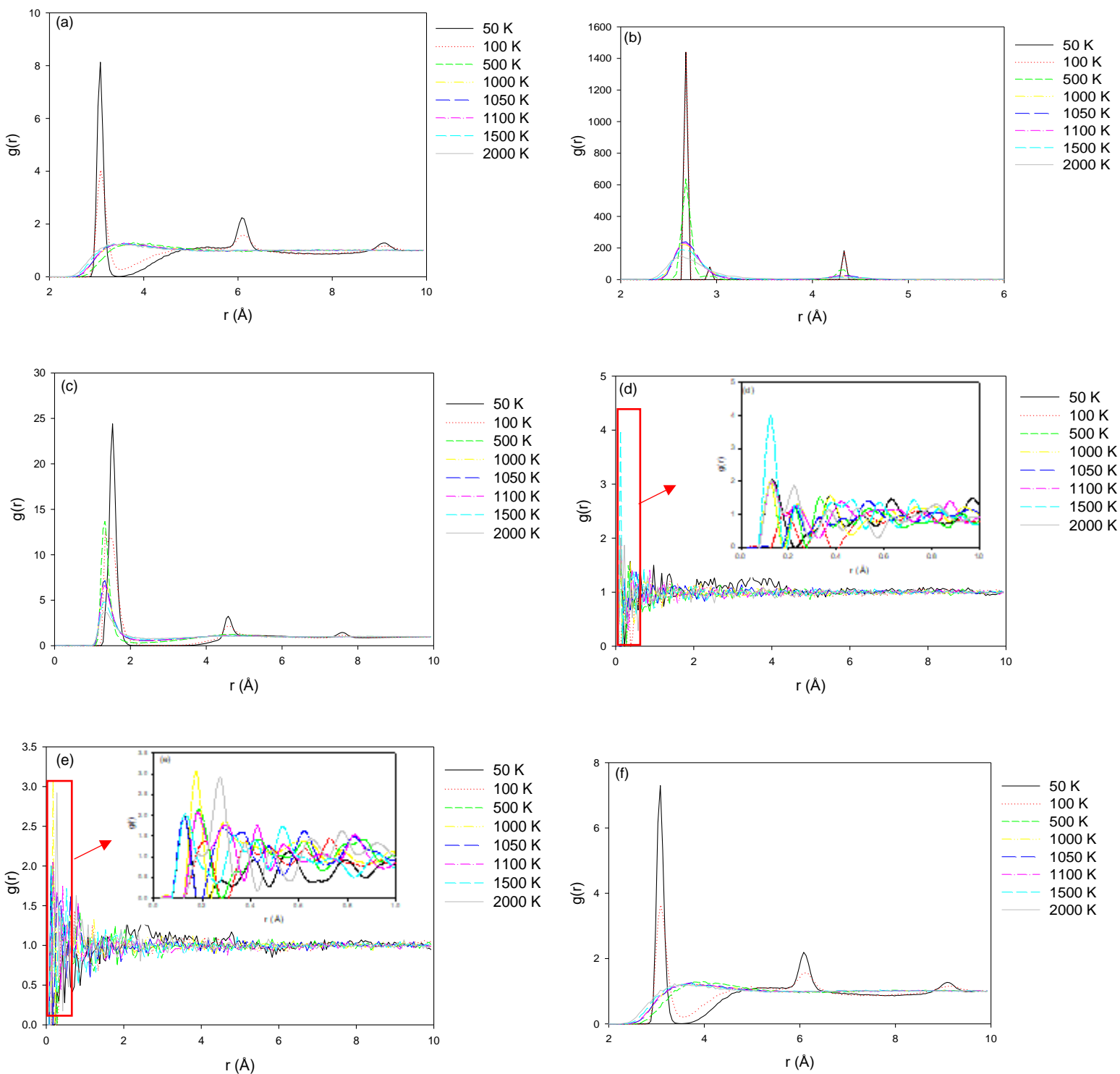
Figure 6.9. Radial distribution function for (a) Ti-Ti, (b) Ti$_7$-Ti$_7$, (c) Ti-Cl, (d) Ti-Ti$_7$, (e) Cl-Ti$_7$ and (f) Cl-Cl for the Ti$_7$/TiCl system (rigid ion model). The insert in (d) and (e) shows the enlarged scale of Ti-Ti$_7$ and Cl-Ti$_7$ peaks.

6.6.2. Ti$_7$/TiCl$_2$

Figure 6.10 shows the radial distribution functions for the interactions in Ti$_7$/TiCl$_2$ system (rigid ion model) at various temperature range. The Ti-Ti first peak (Figure 6.10 (a)) corresponds to a bond length of 3.18 Å. Similarly, to the above case, the peak is highest at low temperatures (g(r) = 8.05 at 50 K) and decreases as the temperature is increased (g(r) = 4.83 at 100 K). At 2000 K, the peak height is low with g(r) of 1.16. We observe a peak at 9.13 Å, which suggests weak interactions at long distances.

However, the Ti$_7$-Ti$_7$ cluster interaction (Figure 6.10 (b)) is more ordered as the temperature is increased with a bond length corresponding to 2.68 Å. At 50 K, the peak is at its highest point (g(r) = 1630.00) and decreases as the temperature is increased (g(r) = 1570 at 100 K). The peak is low at 2000 K with g(r) of 173.00. Also, the bond length is in better agreement with the theoretical prediction (2.65 Å) reported for bicapped trigonal bipyramid geometry of Ti$_7$ [55]. Furthermore, we observe that as the radial distance increases the interactions between atoms become weak, indicated by the second and third peaks (2.93 Å and 4.38 Å) in Figure 6.10 (b).

A similar trend is observed for the Ti-Cl interaction (Figure 6.10 (c)), where the peak decreases with increase in temperature. The Ti-Cl bond distance is 1.43 Å which is lower compared to 2.232 Å as reported theoretically for TiCl$_2$ [150]. Figure 6.10 (d) shows the Ti-Ti$_7$ interaction with the first peak corresponding to 0.23 Å bond length and the highest g(r) of 2.82. The Cl-Ti$_7$ interaction (Figure 6.10 (e)) depicts the bond length corresponding to

0.18 Å and g(r) = 2.33. The peaks reduce in amplitude as the radial distance increases, suggesting long-range order and slight broadening of the atom-pair correlation. This is similar to the observation reported by Terban *et al.* [152] for the terbium (III) ions in layered nanocrystalline phosphate-phosphate.

Similarly, the Cl-Cl strength decreases as the temperature is increased (Figure 6.10 (f)). The RDF peak is highest at low temperatures (g(r) = 7.48 at 50 K) and decreases as temperature is increased (g(r) = 6.61 at 100 K). At 2000 K, the peak height is low with g(r) of 1.09. It was also found that the Cl-Cl bond length corresponds to 2.93 Å in agreement with the theoretical prediction (~3.90 Å) reported for LiCl system [129]. The bonds are weak at longer distances (6.03 Å and 9.08 Å) corresponding to the second and third nearest neighbour atom bonded to Cl.
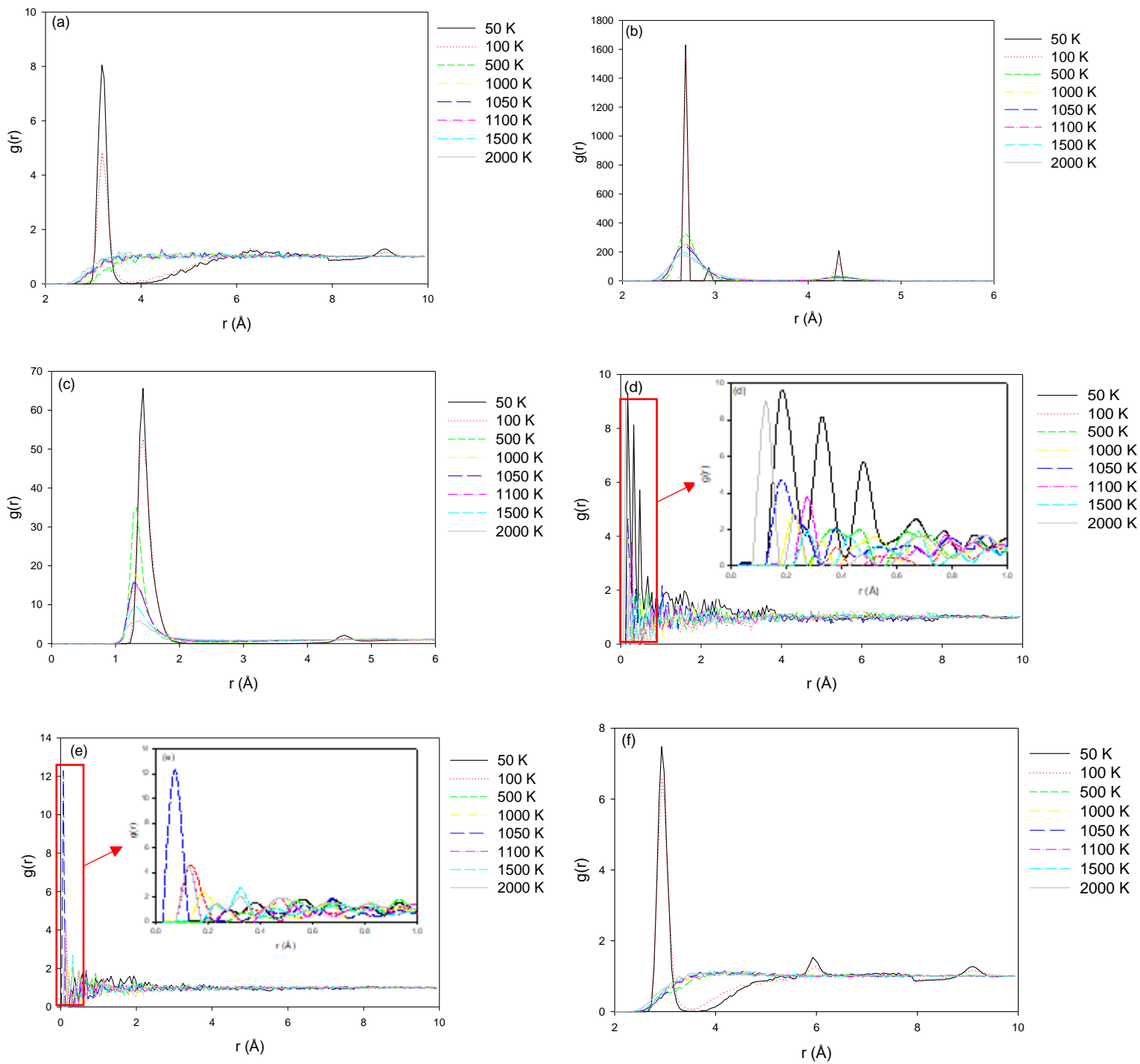
Figure 6.10. Radial distribution function for (a) Ti-Ti, (b) Ti$_7$-Ti$_7$, (c) Ti-Cl, (d) Ti-Ti$_7$, (e) Cl-Ti$_7$ and (f) Cl-Cl for the Ti$_7$/TiCl$_2$ system (rigid ion model). The insert in (d) and (e) shows the enlarged scale of Ti-Ti$_7$ and Cl-Ti$_7$ peaks.

The radial distribution functions show a decrease in peak height as the temperature is increased (Figure 6.9 and 6.10). We observed peaks corresponding to second and third nearest neighbour atoms bonded to the atoms in the systems. These peaks suggest that the bonds between interacting atoms are weak at long distances. As temperature increases, the second and third peaks are reduced ("flatten"). This is expected since an increase in the temperature of a system will result in atoms to gain more kinetic energy, thus a random distribution of atoms which would indicate a phase change [153]. Furthermore, we note that the Ti_7-Ti_7 interactions are more ordered/crystalline (sharp peaks), which suggests that the cluster retains its geometry at high temperature, as shown in Figure 6.11.

An atomic representation of the behaviour of atoms in Ti_7/TiCl and Ti_7/$TiCl_2$ systems (rigid ion model) is shown in Figure 6.11. The figure depicts a pictorial view of the observations made in the RDFs for (a) Ti_7/TiCl and (b) Ti_7/$TiCl_2$ systems in which we observe that the titanium cluster (Ti_7) retains its morphology while the Ti and Cl atoms become randomly distributed as temperature increases. This is shown by the sharp peaks in the Ti_7-Ti_7 interactions in the RDFs, as shown in Figure 6.9 (b) and 6.10 (b).

(a)

(b)
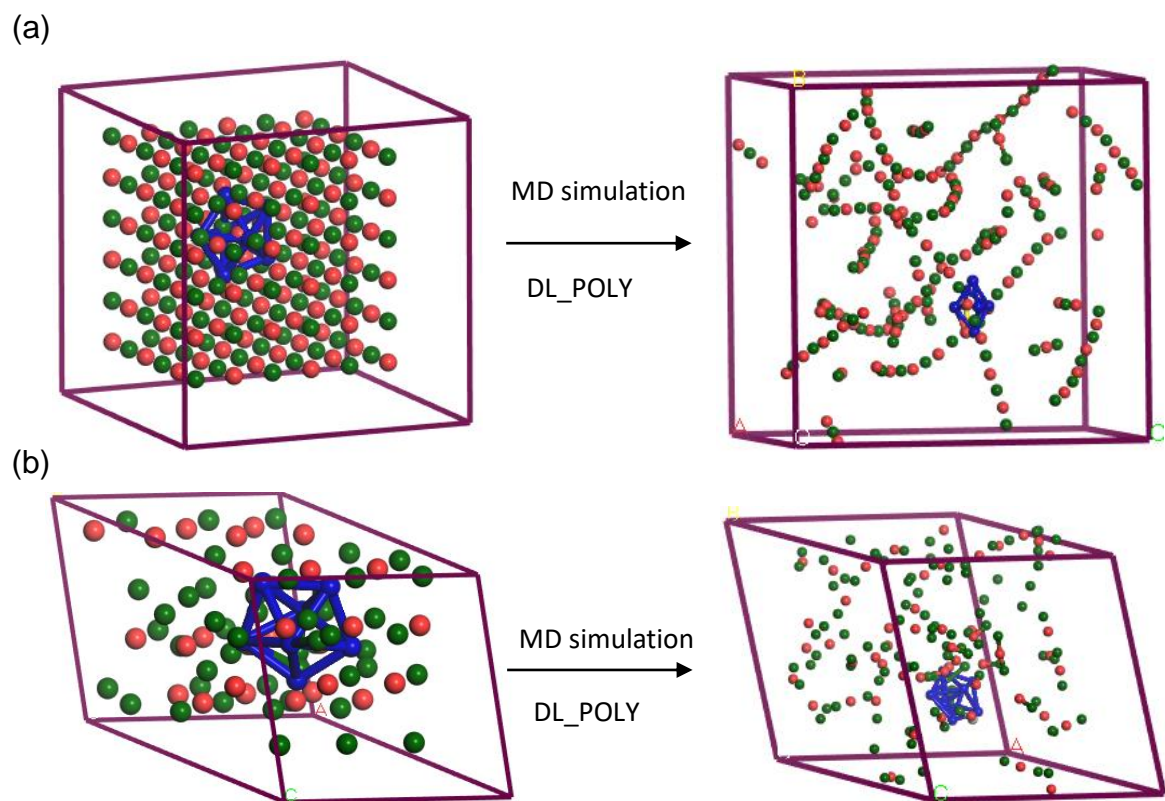
Figure 6.11. Interactions of Ti$_7$ in (a) TiCl and (b) TiCl$_2$ structures for rigid ion model at 50 K – 2000 K.

6.7. Entropy and Gibbs free energy

This section focuses on the thermodynamic properties, particularly the entropy and Gibbs free energy. According to the third law of thermodynamics, the entropy tends to zero at absolute temperature, and molecules are well arranged (perfect order) in the system [154]. We calculated the entropy to measure the randomness and atom disorder in order to understand how temperature influences the increase or decrease in the disorder of atoms in LiCl (rigid ion and shell models), TiCl and TiCl$_2$ systems (rigid ion model).

6.7.1. Entropy

Figure 6.12 depicts the entropy versus temperature graphs. In Figure 6.12 (a), we compare the variation of the LiCl structure using both the rigid ion and shell models. Note that the negative entropy indicates a decrease in disorder and the positive entropy indicates an increase in the disorder of atoms [154]. The rigid ion model shows an increase in the disorder of atoms between 500 K and 900 K. At 400 K and 500 K, the entropy is zero which suggests that the atoms are well arranged (ordered). The shell model, however, shows an increase in disorder in a small range between 500 K and 700 K. We also note that at 400 K the atoms are ordered for the shell model similar to the case of the rigid ion model.

Figure 6.12 (b) depicts the entropy versus temperature graphs for TiCl and $TiCl_2$ structures (rigid ion model). Both systems display ordering at lower temperatures below 400 K. However, the $TiCl_2$ show the degree of ordering at high temperatures between 1000 K and 1500 K. An increase in the disorder of atoms in TiCl is shown at 400 K, 900 K, 1200 K and 1900 K. The $TiCl_2$ structure shows the increase at 50 K, 400 K, 800 K, 900 K and 1800 K. The increase in disorder suggests a phase transition as atoms/molecules are free to move, e.g. in liquid/gas state than in the solid-state [154]. These findings confirm the trends observed in the DC and RDFs of the structures, where the diffusivity increases and peak size decreases with an increase in temperature.
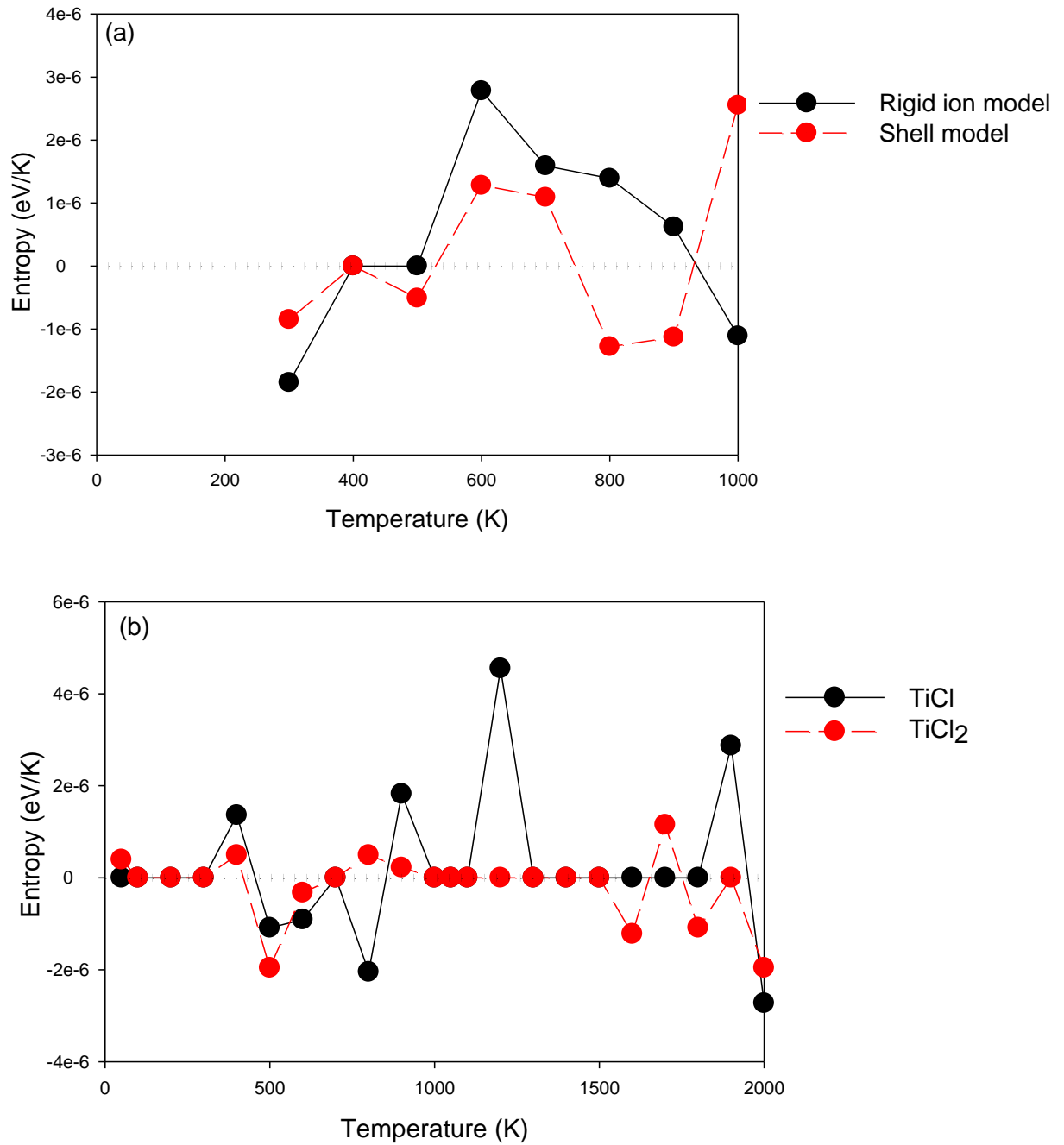
Figure 6.12. The entropy for the (a) LiCl (rigid ion and shell models) and (b) TiCl and TiCl$_2$ (rigid ion model) structures. The dotted line indicates zero entropy.

6.7.2. Gibbs free energy

We then characterised the systems by calculating the Gibbs free energy, defined as the energy that is associated with a chemical reaction and used to do work [155]. This was done to determine equilibrium conditions for the systems. The graphs show a linear increase in the Gibbs free energy with increasing temperature (Figure 6.13).

Figure 6.13 (a) compares the Gibbs free energy versus temperature for LiCl for rigid ion and shell models. We note that the Gibbs free energy values are negative for the LiCl shell model and positive for the rigid ion model. The observation suggests that reactions in LiCl (shell model) are spontaneous (exothermic behaviour) in the entire temperature range, indicating that reactions occur without the addition of energy.

Figure 6.13 (b) depicts the Gibbs free energy versus temperature graphs for TiCl and $TiCl_2$ structures (rigid ion model). The figure shows that the reactions in the TiCl and $TiCl_2$ structures are spontaneous (favourable) below 500 K and become less spontaneous as the temperature is increased above 500 K, suggesting an endothermic behaviour.
.
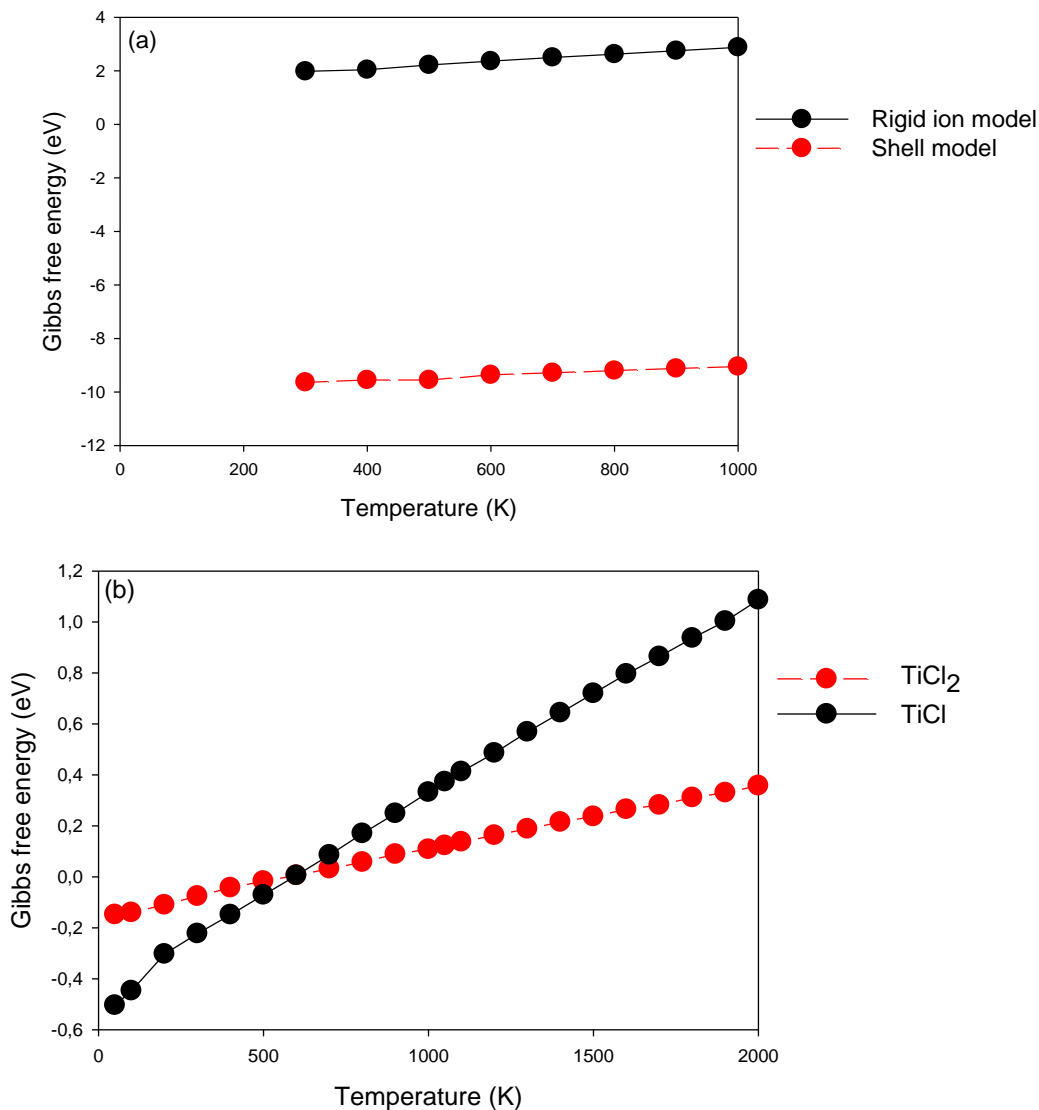
Figure 6.13. Gibbs free energy for (a) LiCl (rigid ion and shell models) and (b) TiCl and TiCl$_2$ (rigid ion model) structures.

These findings suggest that LiCl (shell model) is a favourable medium for investigating the evolution and growth of titanium and that TiCl and TiCl$_2$ (rigid ion model) are favourable mediums at low temperatures (< 500 K). Unfortunately, there is no experimental evidence available that we are aware of; hence the magnitude of errors between calculations and

experiments could not be given. The calculated results can be taken as a prediction study

for future investigation.

Chapter 7

Summary and conclusion

This dissertation provided an extensive study on the geometry, structural and transport properties (diffusion coefficient) for LiCl, Li_7/LiCl (rigid ion and shell models), TiCl, $TiCl_2$, $TiCl_4$, Ti_7/TiCl and Ti_7/$TiCl_2$ (rigid ion model) structures. The density functional theory-based code, CASTEP and FHI-aims were used to study the crystal structure and stability, while the molecular dynamic based-codes, GULP, $DMol^3$ and DL_POLY were used to study the temperature effect on the structures.

Firstly, the validation of the LiCl potential parameter calculations showed that the potential parameters adopted from the Catlow library were able to reproduce the LiCl structure to within an agreement of 1% with experimental data. The elastic constants accord well with experimental observations whilst still obeying the Cauchy relation, and the melting temperature also compares well with the experimental data. DL_POLY code was used to check if the LiCl structure (rigid ion and shell model) was suited for high temperature molecular dynamic simulations. Results from the MD calculations show that a unit cell of 216 atoms and a simulation time of 0.001 ps is enough to achieve adequately converged results with acceptable accuracy for the LiCl structure. The structural properties (RDFs) and transport properties (DC) are proportional to the temperature, and the predicted structural properties of the LiCl structure are in good agreement with the experimental results from published literature. More importantly, the LiCl results provided understanding

on the design and simulation of the desired properties of a medium required to evaluate the growth of titanium clusters.

Secondly, the Ti-Cl and Ti-Li interatomic potential parameters were successfully derived using the PBE-Sol approximation within the FHI-aims code, and the potential parameters were validated using the GULP code. The interatomic potential parameters were found to be valid for the system since they satisfied the sum of squares error function of close to zero. This suggested that the derived potential parameters could be used to describe the interactions of titanium clusters in TiCl environment.

The DL_POLY code was used to check the behaviour of the Ti_7 cluster in the LiCl environment. The titanium cluster was found to have a stable geometry of a pentagonal bipyramid which agreed well with the reported literature [52, 133]. Radial distribution graphs for the Ti_7/LiCl (rigid ion model and shell model) structure depicted a change in the morphology of the system for all interactions as the temperature is increased. This is confirmed by the diffusion coefficient graphs which suggested the melting temperature range of the LiCl structure at 700 K – 800 K for rigid ion model and a melting temperature range of 600 K – 700 K for the shell model. The increase in the diffusion of Cl ions above the melting temperature may be attributed to an increase in the mobility of ions as the temperature is increased. It was also observed that as temperature increases, the titanium cluster geometry could retain its morphology (does not change).

Thirdly, the stability of the titanium cluster (Ti_7) was further investigated using the density functional theory CASTEP and DMol^3 codes. It was observed that the pentagonal bipyramid geometry depicts low energies which suggest that the titanium cluster is stable at this geometry. The capped octahedron geometry is observed at high energies compared to the pentagonal bipyramid, which indicates that this is the least stable geometry for Ti_7 cluster.

Fourthly, the TiCl, $TiCl_2$ and $TiCl_4$ structures were validated by evaluating their change in bond lengths which are important to describe the various interactions. It was found that the equivalent Ti-Cl bond lengths for the structures are reasonable with respect to the experimental value. Furthermore, the elastic constants showed that the TiCl structure is elastically stable whilst the $TiCl_2$ and $TiCl_4$ structures are elastically unstable. However, the mechanical properties indicated that the $TiCl_2$ and $TiCl_4$ structures are mechanically stable (positive shear modulus).

The transferability of the Ti-Cl potential parameters was investigated through the structural and transport properties of the TiCl and $TiCl_2$ structures. The results were found to be comparable with previous theoretical findings. This indicated that the interatomic potential parameters were able to reproduce the bond distances, suggesting transferability.

The melting temperature was predicted from the diffusion coefficient graphs approximated to be 700 K for TiCl and around 800 K for $TiCl_2$. Furthermore, the decrease in the peak size ($g(r)$) observed in the RDFs for the $Ti_7/TiCl_n$ (n=1,2) systems indicate a phase

transition from solid to liquid as the temperature is increased. This is attributed to the random distribution of atoms owing to an increase in kinetic energy as the temperature is increased. Also, we note that the trend observed in the Ti_7/TiCl results is similar to the Ti_7/LiCl graph, which also suggests transferability.

Lastly, the entropy and Gibbs free energy for the LiCl (rigid ion and shell models), TiCl and $TiCl_2$ structures were calculated to evaluate the behaviour of atoms and the spontaneity of the structure. It was observed that the entropy in the structures alternate between a decrease in disorder and an increase in disorder. The increase in disorder suggests a phase transition as atoms/molecules are free to move, e.g. in liquid/ gas state than in the solid state. This finding agrees with the observations made on DC and RDFs. The Gibbs free energy calculations indicated that LiCl (shell model) is a favourable medium. In the case of $TiCl_n$, the evolution and growth of titanium clusters prefer $TiCl_2$ than TiCl at low temperatures (< 500 K) similar to LiCl (shell model), whereas at high temperature $TiCl_2$ is favourable. Moreover, these results may provide insight into understanding the reactions and interactions of titanium clusters with salt mediums in titanium production processes, which is most likely for the $TiCl_2$.

Recommendations and future work

The study of the evolution and growth of titanium clusters in salt mediums has not been systematically carried out, and this remains critical in considering alternative titanium production processes. It requires more understanding of the small clusters and the conditions for cluster growth. The geometry and growth for Ti_7 have been explored in the LiCl (rigid ion model and shell model) and $TiCl_{n=1,2}$ (rigid ion model) mediums using the MD approach. A similar approach could also be followed for the $TiCl_n$ shell model. There is a need to evaluate the behaviour at other salt mediums, with respect to the stable clusters (Ti_5, Ti_7, Ti_{13} and Ti_{19}). This approach will be expanded for the other special or stable titanium clusters such as Ti_5, Ti_{13} and Ti_{19}.

It is essential to study the temperature dependence of these clusters in different salt medium since literature reports that smaller Ti clusters exist at moderate temperatures [156]. As such, it is important to understand how these clusters behave when subjected to temperatures. Furthermore, the Ti_7 cluster formation and growth will also be evaluated for $TiCl_3$ and $TiCl_4$, to obtain the full spectrum (for $TiCl_n$, n=1-4). Calculations using the shell model are also necessary and their interaction with titanium cluster, $Ti_7/TiCl_n$. This will give more knowledge and understanding on the stepwise titanium production process. Thermodynamic properties will be determined, such as Gibbs free energy for each cluster at different salt mediums. The findings will provide sufficient knowledge on the effect of temperature as the number of clusters increases.

APPENDIX A.

The Ti and Cl interactions at different temperatures

(a)
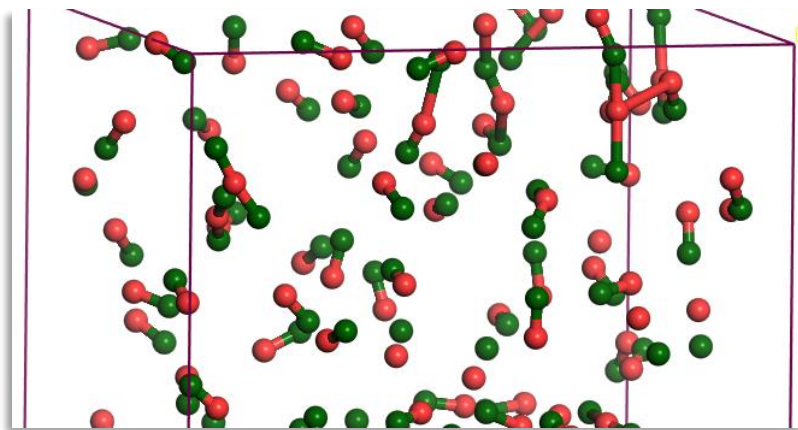
(b)
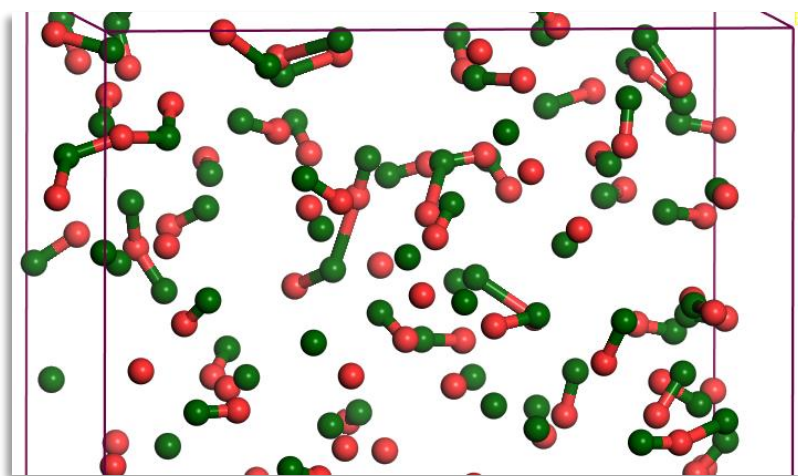
A.1. TiCl structure at (a) 500 K and (b) 900 K showing Ti bonding with Cl.

(a)
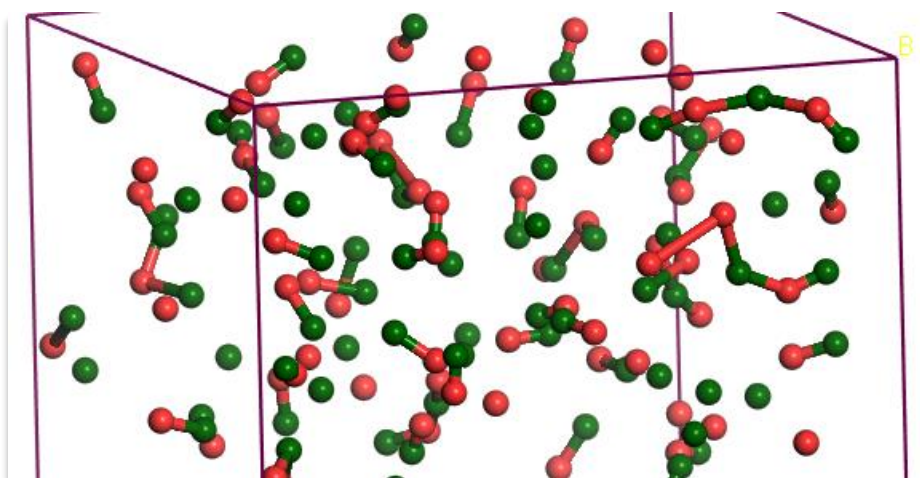
(b)
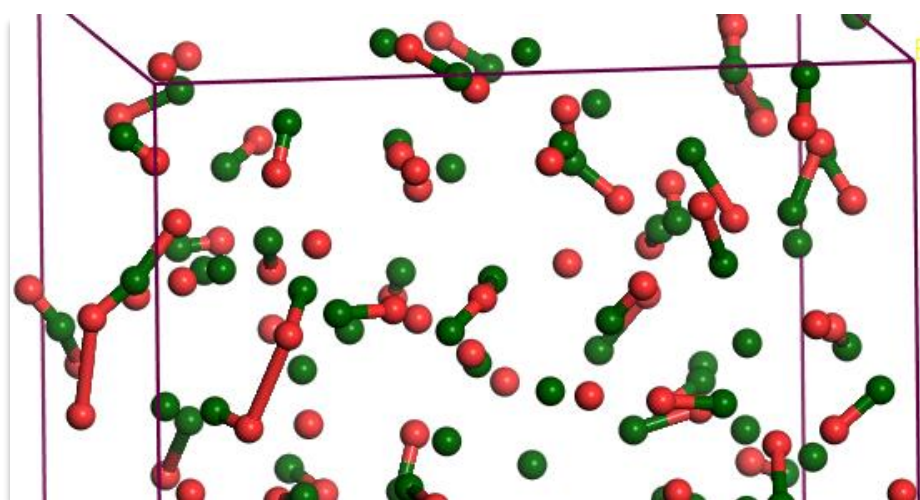
A.2. TiCl structure showing an increase in the bonding of Ti and Cl from (a) 1300 K to (b) 1900 K.

(a)
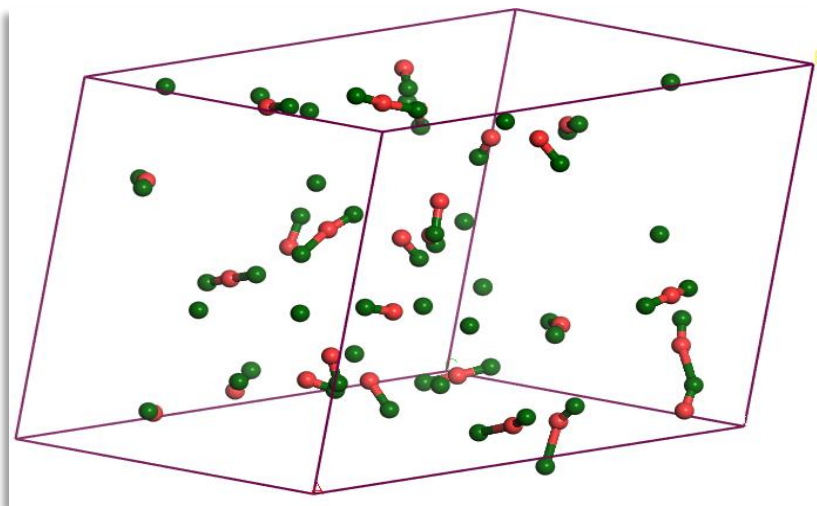
(b)
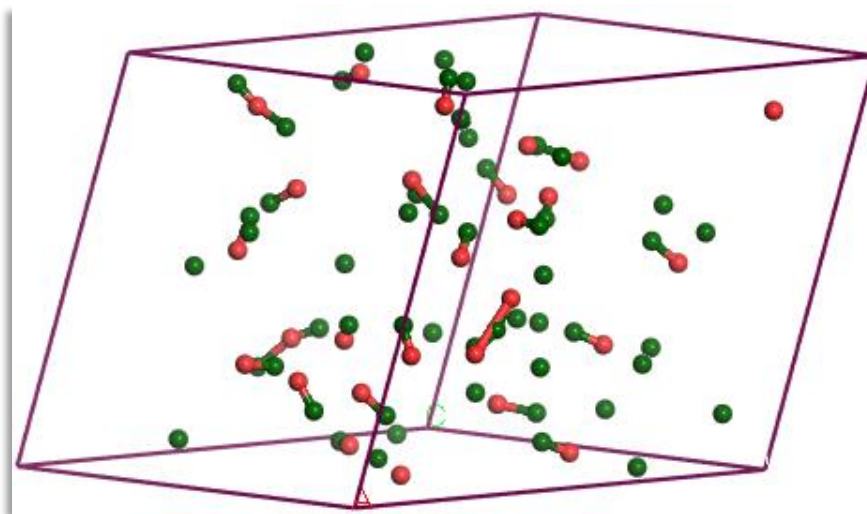
A.3. TiCl₂ structure at (a) 300 K and (b) 900 K showing an increase in the number of non-bonded Ti and Cl as temperature increases.
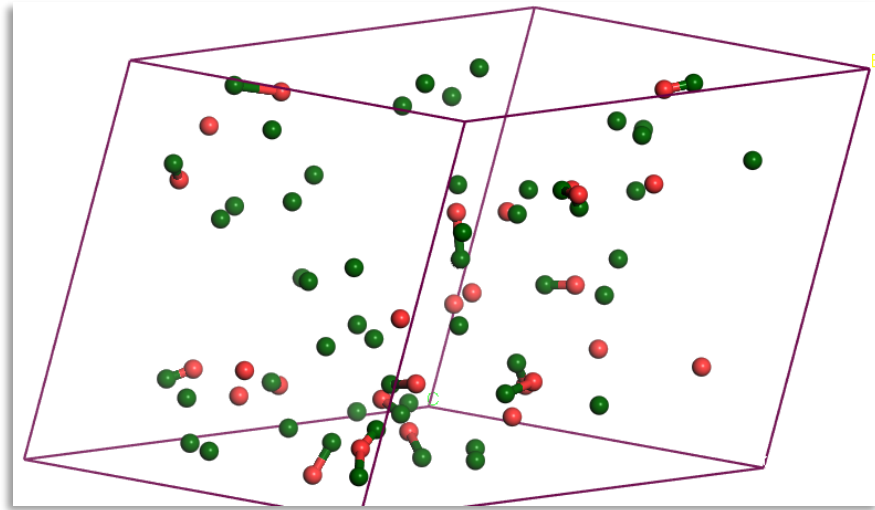
A.4. TiCl$_2$ structure at 1900 K showing the decrease in the bonding of Ti and Cl.

APPENDIX B.

Publications and Presentations at the Conferences

A.1 Presentations at Conferences

- Mazibuko A.F, Diale R.G, Chauke H.R and Ngoepe P.E, "First principle studies of palladium nanoparticles on titanium dioxide surfaces for catalytic applications" SAIP 2018, 25-29 June 2018, University of the Free state, Bloemfontein.

- Mazibuko A.F, Chauke H.R, Ngoepe P.E, Sokol A.A and Catlow C.R.A "Computational modelling studies of Ti-cluster formation in LiCl" Postgraduate research day, 20-21 September 2018, Fusion boutique hotel, Polokwane.

- Mazibuko A.F, Chauke H.R, Ngoepe P.E, Sokol A.A and Catlow C.R.A "Interatomic potential parameters for Li-Cl-Ti interaction" CoSAami conference, 23-26 October 2018, Riverside sun hotel, Vanderbijlpark.

- Mazibuko A.F, Chauke H.R, Ngoepe P.E, Sokol A.A and Catlow C.R.A "Computational modelling studies of Ti-cluster formation in LiCl" CHPC 2018 conference, 1-6 December 2018, Century City Conference Centre, Cape Town.

- Mazibuko A.F, Chauke H.R, Ngoepe P.E, Sokol A.A and Catlow C.R.A "Structural analysis of Ti_7/LiCl" SAIP 2019 conference, 8-12 July 2019, Protea Hotel by Marriott Polokwane Ranch Resort, Polokwane.

- Mazibuko A.F, Chauke H.R, Ngoepe P.E, Sokol A.A and Catlow C.R.A "Temperature dependence of Ti_{13}/LiCl: A molecular dynamics study" Postgraduate

research day, 19-20 September 2019, Protea Hotel by Marriott Polokwane Ranch Resort, Polokwane.

- Mazibuko A.F, Chauke H.R, Ngoepe P.E, Sokol A.A and Catlow C.R.A "Molecular dynamics study of the influence of temperature on Ti_7/LiCl structure" CHPC 2019 conference, 1-5 December 2019, Birchwood, Johannesburg.

A.2 Publications

- Mazibuko A.F, Chauke H.R, Ngoepe P.E, Sokol A.A and Catlow C.R.A "Interatomic potential parameters for Li-Cl-Ti interaction" IOP Conference Series Materials Science and Engineering 430(1): 012016 October 2018.

- Mazibuko A.F, Diale R.G, Chauke H.R and Ngoepe P.E, "First principle studies of palladium nanoparticles on titanium dioxide surfaces for catalytic applications" in The Proceedings of SAIP2018, the 63rd Annual Conference of the South African Institute of Physics, edited by Prof. Japie Engelbrecht (NMMU), pp. 37-43. ISBN: 978-0-620-85406-1. Available online at http://events.saip.org.za

References

[1]   R. Motsie, "An overview of South Africa's titanium mineral concentrate industry Report R71," Directorate: Mineral Economics, Mineralia Centre, 2008.

[2]   Z.Z. Fang, J.D. Paramore, P. Sun, K.S.R. Chandran, Y. Zhang, Y. Xia, F. Cao, M. Koopman and M. Free, "Powder metallurgy of titanium-past, present and future," *International Materials Reviews,* **63**, p. 407, 2018.

[3]   A.F. Mazibuko, H.R. Chauke, P.E. Ngoepe, A.A. Sokol and C.R.A. Catlow, "Interatomic potential parameters for Li-Cl-Ti interaction," *IOP Conference Series: Materials Science and Engineering,* **430**, p. 1, 2018.

[4]   H. Fujii and T. Maeda, "Titanium alloys developed by Nippon Steel & Sumitomo metal corporation," *Nippon Steel & Sumitomo Metal Technical Report 106*," p. 16, 2014.

[5]   E. Mastrocinque, "Laser welding of Ti6Al4V alloy disk laser: Analysis and optimization," PhD Thesis, 2011.

[6]   E.R. Poulsen and J.A. Hall, "Extractive metallurgy of titanium: A review of the state of the art and evolving production techniques," *Journal of Metals,* p. 60, 1983.

[7]   A. Fuwa and S. Takaya, "Producing titanium by reducing $TiCl_2$-$MgCl_2$ mixed salt with magnesium in the molten state," *Journal of the Minerals, Metals and Materials Society,* p. 56, 2005.

[8] O. Taked and T.H. Okabe, "A new high speed titanium production by subhalide reduction process," *Light metals Proceedings of the 2005 TMS annual meeting,* p. 1139, 2005.

[9] T. Noda, "Titanium from slag in Japan," *Journal of Metals,* **17**, p. 25, 1965.

[10] E. Platacis, I. Kaldre, E. Blumbergs, L. Goldšteins and V. Serga, "Titanium production by magnesium thermal reduction in the electroslag process," *Scientific Reports*, 9, p. 1, 2019.

[11] M. Jackson and K. Dring, "A review of advances in processing and metallurgy of titanium alloys," *Materials Science and Technology*, **22**, p. 881, 2006.

[12] F. Seon and P. Nataf, "Production of Metals by Metallorthermia", US Patent 4725312, 16 February 1988.

[13] D.S. van Vuuren, "Direct titanium powder production by metallothermic processes," *Titanium Powder Metallurgy,* p. 69, 2015.

[14] D.S. van Vuuren, S.J. Oosthuizen and M.D. Heydenrych, "Titanium production via metallothermic reduction of $TiCl_4$ in molten salt: Problems and products," *The Journal of The Southern African Institute of Mining and Metallurgy,* **111**, p. 141, 2011.

[15] H.-S. Shin, J.-M. Hur, S.M. Jeong and K.Y. Jung, "Direct electrochemical reduction of titanium dioxide in molten lithium chloride, " *Journal of Industrial and Engineering*, **18**, p. 438, 2012.

[16] O. Takeda and T.H. Okabe, "High-speed titanium production by magnesiothermic reduction of titanium trichloride," *Materials Transactions,* **47**, p. 1145, 2006.

[17] D.S. van Vuuren, "Keynote address: Titanium-an opportunity and challenge for South Africa," *The Journal of The Southern African Institute of Mining and Metallurgy,* p. 1, 2009.

[18] A. Fernando, K.L.D.M. Weerawardene, N.V. Karimova and C.M. Aikens, "Quantum mechanical studies of large metal, metal oxide, and metal chalcogenide nanoparticles and clusters," *Chemical Reviews,* **115**, p. 6112, 2015.

[19] S. Plimpton, "Fast parallel algorithms for short-range molecular dynamics," *Journal of Computational Physics,* **117**, p. 1, 1995.

[20] V. Blum, R. Gehrke, F. Hanke, P. Havu, V. Havu, X. Ren, K. Reuter and M. Scheffler, "Ab initio molecular simulations with numeric atom-centred orbitals," *Computer Physics Communications,* **180**, p. 2175, 2009.

[21] J.D. Gale, "GULP: A computer program for the symmetry-adapted simulation of solids," *Journal of Chemical Society,* **93**, p. 629, 1997.

[22] I.T. Todorov, W. Smith, K. Trachenko and M.T. Dove, "DL_POLY_3: New dimensions in molecular dynamics simulations via massive parallelism," *Journal of Materials Chemistry*, **16**, p. 1911, 2006.

[23] W. Smith and I.T. Todorov, "A short description of DL_POLY," *Molecular Simulation,* **32**, p. 935, 2006.

[24] S. Jiao and H. Zhu, "Novel metallurgical process for titanium production," *Journal of Materials Research*, **21**, p. 2172, 2006.

[25] V.A.R. Henriques, "Titanium production for aerospace applications," *Journal of Aerospace Technology and Management,* **1**, p. 7, 2009.

[26] J.C. White and O.L. Oden, "Continuous production of granular Ti, Zr and Hf or their alloy products," US Patent 5259862, 9 November 1993.

[27] C.H. Winter, "Production of Metals," US Patent 2607674, 19 August 1952.

[28] H. Agripa and I. Botef, "Modern production methods for titanium alloys: A review," 24 August 2019. [Online]. Available: https://www.intechopen.com/books/titanium-alloys-novel-aspects-of-their-manufacturing-and-processing/modern-production-methods-for-titanium-alloys-a-review. [Accessed 18 November 2019].

[29] V.I. Evdokimov and V.A. Krenev, "Magnesium reduction of titanium tetrachloride," *Inorganic Materials,* **38**, p. 490, 2002.

[30] W. Zhang, Z. Zhu and C.Y. Cheng, "A literature review of titanium metallurgical processes," *Hydrometallurgy,* **108**, p. 177, 2011.

[31] G.Z. Chen, D.J. Fray and T.W. Farthing, "Direct electrochemical reduction of titanium dioxide to titanium in molten calcium chloride," *Nature*, **407**, p. 361, 2000.

[32] S.J. Oosthuizen, "In search of low cost titanium: The Fray Farthing Chen (FFC) cambridge process," *The Journal of The Southern African Institute of Mining and Metallurgy,* **111**, p. 199, 2011.

[33] D. Hu, A. Dolganov, M. Ma, B. Bhattacharya, M.T. Bishop and G.Z. Chen, "Development of the Fray-Farthing-Chen cambridge process: Towards the sustainable production of titanium and its alloys," *The Journal of The Minerals, Metals & Materials Society,* **70**, p. 129, 2018.

[34] B. Zhang, C. Li and S. Shan, "Thermodynamic calculation of self-diffusion in sodium chloride," *Physics and Chemistry of Minerals*, **43**, p. 371, 2016.

[35] L.G. Harrison, J.A. Morrison and R. Rudham, "Chloride ion diffusion in sodium chloride," *Transactions of the Faraday Society,* **54**, p. 106, 1958.

[36] K. Sommer and B. Friedrich, "Titanium molten salt electrolysis-latest developments," *European Metallurgical Conference*, p. 1, 2005.

[37] J. Haidar, "Method and apparatus for forming titanium-aluminium based alloys. International Patent Publication," United States Patent WO2009129570, 29 October 2009.

[38] R.A. Guidotti and P. Masset, "Thermally activated ("thermal") battery technology. Part I: An overview," *Journal of Power Sources,* **161**, p. 1443, 2006.

[39] P. Masset and R.A. Guidotti, "Thermal activated ("thermal") battery technology. Part II: Molten salt electrolytes," *Journal of Power Sources,* **164**, p. 397, 2007.

[40] A.R. Kamali, D.J. Fray and C. Schwandt, "Thermokinetic characteristics of lithium chloride," *Journal of Thermal Analysis and Calorimetry,* **104**, p. 619, 2011.

[41] K. Nitsch, M. Dušek, M. Nikl, K. Polák, M. Rodová, "Ternary alkali lead chlorides: Crystal growth, crystal structure, absorption and emission properties," *Progress in Crystal Growth and characterization of Materials,* **30**, p. 1, 1995.

[42] M.V. Smirnov, I.V. Korzun and V.A. Oleynikova, "Hydrolysis of molten alkali chlorides, bromides and iodides," *Electrochimica Acta,* **33**, p. 781, 1988.

[43] W.G. Wyckoff, Crystal structures. 2nd ed., New York: Wiley, 1963.

[44] C. Leyens and M. Peters, Titanium and titanium alloys: Fundamentals and applications, Germany: Wiley, 2003.

[45] M. Mikami, S. Nakamura, O. Kitao H. Arakawa and X. Gonze, "First principle study of titanium dioxide: Rutile and anatase," *Japanese Journal of Applied Physics,* **39**, p. L847, 2000.

[46] A. Kale and K. Bisaka, "Fluid bed chlorination pilot plant at Mintek," *The Journal of The Southern African Institute of Mining and Metallurgy,* **111**, p. 193, 2010.

[47] H. Bordbar, H. Abedini and A.A. Yousefi, "Parameters affecting reaction rate and conversion of TiO_2 chlorination in a fluidized bed reactor: Experimental and modelling approach," *Transactions of nonferrous Metals Society of China,* **28**, p. 2114, 2018.

[48] J. Gambogi, "Titanium, 2007 Minerals year book," US Geological Survey, U.S Government printing office, Washington DC, p.195, 2009.

[49] A. Stwerka, Guide to the elements, London: Oxford university press, 1998.

[50] J. Whitehead, Titanium compounds (Inorganic), Hoboken: John Wiley and Sons, 1983.

[51] G.L. Estiu and M.C. Zerner, "Interplay between geometric and electronic structure and the magnetism of small Pd clusters," *Journal of Physical Chemistry,* **98**, p. 4793, 1994.

[52] T. Lazauskas, A.A. Sokol, J. Buckeridge, C.R.A. Catlow, S.G.E.T. Escher, M.R. Farrow, D. Mora-Fonz, V.W. Blum, T.M. Phaahla, H.R. Chauke, P.E. Ngoepe and S.M. Woodley, "Thermodynamically accessible titanium clusters Ti_n (n=2-32)," *Physical Chemistry Chemical Physics,* **20**, p. 13962, 2018.

[53] P. Nava, M.Sierka and R. Ahlrichs, "Density functional study of palladium clusters," *Physical Chemistry Chemical Physics,* **5**, p. 3372, 2003.

[54] J.A. Alonso, "Electronic and atomic structure, and magnetism of transition-metal clusters," *Chemical Reviews,* **100**, p. 637, 2000.

[55] J. Zhao, Q. Qui, B. Wang, J. Wang and G. Wang, "Geometric and electronic properties of titanium clusters studied by ultrasoft pseudopotential," *Solid State Communications,* **118**, p. 157, 2001.

[56] H. Sun, Y. Ren, Z. Wu and N. Xu, "Density functional calculation of the growth, electronic and bonding properties of titanium clusters Ti_n (n=2-20)," *Computational and Theoretical Chemistry,* **1062**, p. 74, 2015.

[57] B. Lee and G.W. Lee, "Comparative study of Ti and Ni clusters from first principles," *Journal of Chemical Physics,* **127**, p. 164316, 2007.

[58] J. Medina, R. deCoss, A. Tapia, and G. Canto, "Structural, energetic and magnetic properties of small Ti_n (n = 2–13) clusters: A density functional study," *European Journal of Physics,* **76**, p. 427, 2010.

[59] S.-Y. Wang, W. Duan, D.-L. Zhao, and C.-Y. Wang, "First-principles study of the stability of the icosahedral Ti_{13}, Ti^-_{13}, and Ti^+_{13} clusters," *Physical Review B,* **65**, p. 165424, 2002.

[60] S.-Y. Wang, J.-Z. Yu, H. Misuzeki, J.-A. Yan, Y. Kawazoe and C.-Y. Wang, "First-principles study of the electronic structures of icosahedral Ti_n (n=13,19,43,55) clusters," *Journal of Chemical Physics,* **120**, p. 8463, 2004.

[61] M.A. Duncan, Advances in metal and semiconductor clusters: Cluster materials, London: Elsevier, 1998.

[62] H. Wu, S.R. Desai and L.S. Wang, "Electronic structures of small titanium clusters: Emergence and evolution of the 3d band," *Physical Review Letters,* **76**, p. 212, 1996.

[63] F. Aguilera-Granja, J.L. Rodríguez-López, K. Michaelian, E.O. Berlanga-Ramírez, A. Vega, "Structure and magnetism of small rhodium clusters," *Physical Review B,* **66**, p. 224410, 2002.

[64] H. Berry, B. Wang and Q. Zhang, "The behaviour of magnetic properties in the clusters of 4d transition metals," *Molecules,* **23**, p. 1896, 2018.

[65] D. Kaiming, Y. Jinlong, X. Chuanyun and W. Kelin, "Magnetic properties of M_{13} clusters (M=Y, Zr, Nb, Mo and Tc)," *Physical Review B,* **54**, p. 11907, 1996.

[66] V. Kumar and Y. Kawazoe, "Atomic and electronic structures of niobium clusters," *Physical Review B,* **65**, p. 125403, 2002.

[67] L.M. Molina, M.J. López, A. Rubio, L.C. Balbás and J.A. Alonso, "Pure and mixed Pb clusters of interest for liquid ionic alloys," *Advances in Quantum Chemistry,* **33**, p. 329, 1998.

[68] B. Wang, J. Zhao, X. Chen, D. Shi and G. Wang, "Atomic structures and covalent-to-metallic transition of lead clusters Pb_n (n= 2–22)," *Physical Review A,* **71**, p. 033201, 2005.

[69] M.G. Mulaudzi, "Ab initio study of structural stability and electronic properties of $ZrO_{2-x}S_x$ for $0 \leq x \leq 2$," MSc Dissertation, 2015.

[70] S.J. Clark, M.D. Segall, C.J. Pickard, P.J. Hasnip, M.J. Probert, K. Refson and M.C. Payne, "First principles methods using CASTEP," *Zeitschrift für Kristallographie,* **220**, p. 567, 2005.

[71] M.D. Segall, P.J.D. Lindan, M.J. Probert, C.J. Pickard, P.J. Hasnip, S.J. Clark and M.C. Payne, "First-principles simulation: Ideas, illustrations and CASTEP code," *Journal of Physics: Condensed Matter,* **14**, p. 2717, 2002.

[72] B. Delley, D.E. Ellis, A.J. Freeman, E.J. Baerends and D. Post, "Binding energy and electronic structure of small copper particles," *Physical Review B.,* **27**, p. 2132, 1983.

[73] B. Delley, "An all-electron numerical method for solving the local density functional for polyatomic molecules," *The Journal of Chemical Physics,* **92**, p. 508, 1990.

[74] J. Xiang, X.H. Yan, Y.L. Mao, Y. Xiao and S.H. Wei, "Structural, electronic and magnetic properties of small Ti_nAl (n=1-8) clusters," *International Journal of Modern Physics C,* **15**, p. 775, 2004.

[75] R.E. Watson, G.W. Fernando, M. Weinert and J.W. Davenport, "First principles calculations: The elemental transition metals and their compounds," *Journal of Phase Equilibria,* **13**, p. 224, 1992.

[76] J. Kotz, P. Treichel and J. Townsend, Chemistry and chemical reactivity, Boston: Cengage Learning, 2008.

[77] J.T. Fulton, The neurons and neural system: A 21st century paradigm, Indiana: Trafford Publishing, 2016.

[78] L.-F. Huang, B. Grabowski, E. McEniry, D.R. Trinkl and J. Neugebauer, "Importance of coordination number and bond length in titanium revealed by electronic structure investigations," *Physica Status Solidi B,* **252**, p. 1907, 2015.

[79] A.E. Mattsson, P.A. Schultz, M.P. Desjarlais, T.R. Mattsson and K. Leung, "Designing meaningful density functional theory calculations in materials science-a primer," *Modelling Simulation in Materials Science and Engineering,* **13**, p. R1, 2005.

[80] P. Hohenberg and W. Kohn, "Inhomogeneous electron gas," *Physical Review B,* **136**, p. 864, 1964.

[81] W. Kohn and L.J. Sham, "Self-consistent equations including exchange and correlation effects," *Physical Review A,* **140**, p. 1133, 1965.

[82] M.P. Allen, "Introduction to molecular dynamics simulation," *Computational soft matter,* **23**, p. 1, 2004.

[83] J.C. Slater, "A simplification of the Hartree-Fock method," *Physical Review,* **81**, p. 385, 1951.

[84] G.E.W. Bauer, "General operator ground-state expectation values in the Hohenberg-Kohn-Sham density-functional formalism," *Physical Review B,* **27**, p. 5912, 1983.

[85] R.K. Pathak, "Statistical electron angular correlation coefficients for atoms within the Hohenberg-Kohn-Sham theory," *Physical Review A,* **31**, p. 2806, 1985.

[86] R. LeSar, Introduction to computational materials science: Fundamentals to applications, New York: Cambridge University Press, 2013.

[87] J.P. Perdew, K. Burke and M. Ernzerhof, "Generalized gradient approximation made simple," *Physical Review Letters,* **77**, p. 3865, 1996.

[88] J.P. Perdew, J.A. Chevary, S.H. Vosko, K. A. Jackson, M.R. Pederson, D.J. Singh and C. Fiolhais, "Atoms, molecules, solids and surfaces: Application of the generalized gradient approximation for exchange and correlation," *Physical Review B,* **46**, p. 6671, 1992.

[89] S. Kurth, J.P. Perdew and P. Blaha, "Molecular and solid-state tests of density functional approximations: LSD, GGAs, and meta-GGAs," *International Journal of Quantum Chemistry,* **75**, p. 889, 1999.

[90] J.P. Perdew, A. Ruzsinszky, G.I. Csonka, O.A. Vydrov, G.E. Scuseria, L.A. Constantin, X. Zhou and K. Burke, "Restoring the density-gradient expansion for exchange in solids and surface," *Physical Review Letters,* **100**, p. 136406, 2008.

[91] A. Patra, J.E. Bates, J. Sun and J.P. Perdew, "Properties of real metallic surfaces: Effects of density functional semilocality and van der Waals nonlocality," *Proceedings of the National Academy of Sciences,* **114**, p. E9188, 2017.

[92] M.C. Payne, M.P. Teler, D.C. Allan, T.A. Arias and J.D. Joannopoulos, "Iterative minimization techniques for ab initio total-energy calculations: Molecular dynamics and conjugate gradients," *Reviews of Modern Physics,* **64**, p. 1045, 1992.

[93] M.L. Cohen and V. Heine, "The fitting of pseudopotentials to experimental data and their subsequent application," *Solid State Physics,* **24**, p. 37, 1970.

[94] M.T. Yin and M.L. Cohen, "Theory of ab initio pseudopotential calculations," *Physical Review B,* **25**, p. 7403, 1982.

[95] I.J. Esekon, "Application of the quantum espresso code to study the structural and electronic properties of titanium dioxide: A DFT study," MSc Dissertation, 2016.

[96] L. Kleinman and D.M. Bylander, "Efficacious form for model pseudopotentials," *Physical Review Letters,* **48**, p. 1425, 1982.

[97] D. Vanderbilt, "Soft self-consistent pseudopotentials in a generalized eigenvalue formalism," *Physical Review B,* **41**, p. 7892(R), 1990.

[98] D.J. Chadi and M.L. Cohen, "Special points in the Brillouin zone," *Physical Review B,* **8**, p. 5747, 1973.

[99] J.D. Joannopoulos and M.L. Cohen, "Electronic charge densities for ZnS in the wurtzite and zincblende structures," *Journal of Physics C: Solid State Physics,* **6**, p. 1572, 1973.

[100] H.J. Monkhorst and J.D. Pack, "Special points for Brillouin-zone integrations," *Physical Review B,* **13**, p. 5188, 1976.

[101] P. Kratzer and J. Neugebauer, "The basics of electronic structure theory for periodic systems," *Frontiers in Chemistry,* **7**, p. 106, 2019.

[102] J.D. Gale and A.L. Rohl, "The general utility lattice program (GULP)," *Molecular Simulation,* **5**, p. 291, 2003.

[103] J.D. Gale, "Empirical potential derivation for ionic materials," *Philosophical Magazine B,* **73**, p. 3, 1996.

[104] L. Verlet, "Computer 'experiments' on classical fluids. I. Thermodynamical properties of Lennard-Jones molecules," *Physical Review*, **159**, p. 98, 1967.

[105] B.J. Alder and T.E. Wainwright, "Phase transition for a hard sphere system," *The Journal of Chemical Physics,* **27**, p. 1208, 1957.

[106] M.P. Allen and D.J. Tildesley, Computational simulation of liquids, New York: Oxford University Press, 1987.

[107] N. W. Ashcroft and N.D. Mermin, On introductory concepts, Philadelphia: Saunders College Publishing, 1976.

[108] R.A. Buckingham, "The classical equation of state of gaseous helium, neon and argon," *Proceedings of the Royal Society A: Mathematical, Physical and Engineering Sciences,* **168**, p. 264, 1938.

[109] C.R.A. Catlow, K.M. Diller and M.J. Norgett, "Interionic potentials for alkali halides," *Journal of Physics C: Solid State Physics,* **10**, p. 1395, 1977.

[110] P.M. Morse, "Diatomic molecules according to the wave mechanics. II. vibrational levels.," *Physical Review,* **34**, p. 57, 1929.

[111] C.R.A. Catlow and M.J. Norgett, "UKAEA report AERE-M2936," United Kingdom Atomic Energy Authority, 1978.

[112] I.D. Faux, "The polarization catastrophe in defect calculations in ionic crystals," *Journal of Physics C: Solid State Physics,* **4**, p. L211, 1971.

[113] B.G. Dick Jr. and A.W. Overhauser, "Theory of the dielectric constants of alkali halide crystals," *Physical Review,* **112**, p. 90, 1958.

[114] R.E. Taylor, C.Y. Ho, T.H.K. Barron, A. Cezairliyan, P.S. Gaal, T. Hahn, C.Y. Huang, R.K. Kirby, H.A. McKinstry, S.T. McKinstry, A.P. Miiller, B.D. Rothrock, G. Ruffino,

C.A. Swenson and G.K. White, Thermal expansion of solids, Ohio: ASM International, 1998.

[115] A.D.B. Woods, W. Cochran and B.N. Brockhouse, "Lattice dynamics of alkali halide crystals," *Physical Review,* **119**, p. 980, 1960.

[116] A.B.R. Touré, E. Mele and J.K. Christie, "Atomic-scale clustering inhibits the bioactivity of fluoridated phosphate glasses," *Biomedical Glasses,* **5**, p. 76, 2019.

[117] V.I. Lebedev, "Difference analogues of orthogonal decompositions of basic differential operators and some boundary value problems. I," *USSR Computational Mathematics and Mathematical Physics,* **4**, p. 449, 1964.

[118] X. Ren, P. Rinke, V. Blum, J. Wieferink, A. Tkatchenko, A. Sanfilippo, K. Reuter and M. Scheffler, "Resolution-of-identity approach to Hartree–Fock, hybrid density functionals, RPA, MP2 and GW with numeric atom-centered orbital basis functions," *New Journal of Physics*, **14**, p. 053020, 2012.

[119] S. Haussühl, "Thermo-elastiche konstanten der alkalihalogenide vom NaCl-Typ," *Zeitschrift für Physik,* **159**, p. 223, 1960.

[120] M. Grimsditch, P. Loubeyre and A. Polian, "Brillouin scattering and three-body forces in argon at high pressures," *Physical Review B,* **33**, p. 7192, 1986.

[121] H. Shimizu, M. Ohnishi and S. Sasaki, "Cauchy relation in dense H_2O ice VII," *Physical Review Letters,* **74**, p. 2820, 1995.

[122] N. Gnanasankaran, S. Natarajan, K. Alagarsamy and K. Iyakutti, "A case study of the application of COTS components in a molecular dynamics software," *Lecture notes on Software Engineering,* **1**, p. 141, 2013.

[123] H.J. Hou, F.J. Kong, J.W. Yang, S.Q. Wan and S.X. Yang, "Ab initio investigation on the elastic, dynamical and thermodynamic properties of LiCl," *Physica B Condensed Matter,* **428**, p. 5, 2013.

[124] B.B. Karki, L. Stixrude, S.J. Clark, M.C. Warren and G.J. Ackland, "Elastic properties of orthorhombic $MgSiO_3$ perovskite at lower mantle pressures," *American Mineralogist,* **82**, p. 51, 1997.

[125] R.M. Wentzcovitch, N.L. Ross and G.D. Price, "Ab initio study of $MgSiO_3$ and $CaSiO_3$," *Physics of the Earth and Planetary Interiors,* **90**, p. 101, 1995.

[126] J.O. Hirschfelder, C.F. Curtiss and R.B. Bird, Molecular theory of gases and liquids, New York: Wiley, 1954.

[127] A.M. Brown and M.F. Ashby, "Correlations for diffusion constants," *Acta Metallurgica,* **28**, p. 1085, 1980.

[128] M. Prencipe, A. Zupan, R. Dovesi, E. Apra and V.R. Saunders, "Ab initio study of the structural properties of LiF, NaF, KF, LiCl, NaCl and KCl," *Physical Review B,* **51**, p. 3391, 1995.

[129] A. Bengston, H.O. Nam, S. Saha, R. Sakidja and D. Morgan, "First-principles molecular dynamics modeling of the LiCl–KCl molten salt system," *Computational Materials Science,* **83**, p. 362, 2014.

[130] A.K. Sinha and P. Duwez, "Radial distribution function of amorphous Ni-Pt-P alloys," *Journal of Physics and Chemistry of Solids*, **32**, p. 267, 1971.

[131] K.P. Huben and G. Herzberg, Molecular spectra and molecular structure constants of diatomic molecules, New York: Von Nostrand-Reinhold, 1979.

[132] T. Mohoric, J. Hribur-lee and V. Vlachy, "Effects of the translational and rotational degrees of freedom on the hydration of simple solutes," *The Journal of Chemical Physics,* **140**, p. 184510, 2014.

[133] H. Sutherland-Cash, D.J. Wales and D. Chakrabarti, "Free energy basin-hopping," *Chemical Physics Letters,* **625**, p. 1, 2015.

[134] B. Douglas and S.M. Ho, Structure and chemistry of crystalline solids, Berlin: Springer Science & Business Media, 2007.

[135] M. Born, "On the stability of crystal lattices. I," *Mathematical Proceedings of the Cambridge Philosophical Society,* **36**, p. 160, 1940.

[136] N.M. Harrison and V.R. Saunders, "The structural properties of β-MgCl$_2$: An ab initio study," *Journal of Physics: Condensed Matter,* **4**, p. 3873, 1992.

[137] S. Pothoczki and L. Pusztai, "Molecular liquid TiCl$_4$ and VCl$_4$: Two substances, one structure?," *Journal of Molecular Liquids,* **145**, p. 38, 2009.

[138] M. Doverstål, L. Karlsson, B. Lindgren, U. Sassenberg, "The $^3\Delta_u - X^3\Delta_g$ Band System of Jet-Cooled Ti$_2$," *The Journal of Physical Letters,* **270**, p. 273, 1997.

[139] A. Maeda, T. Hirao, P.F. Bernath and T. Amano, "Submillimeter-wave spectroscopy of TiCl in the ground electronic state," *Journal of Molecular Spectroscopy,* **210**, p. 25, 2001.

[140] C.A.L. Becker, C.J. Ballhausen and I. Trabjerg, "Investigation of the electronic structure of TiCl$_4$," *Theoretica Chimica Acta,* **13**, p. 355, 1969.

[141] N.C. Baenziger and R.E. Rundle, "The structure of TiCl$_2$," *Acta Crystallographica,* **1**, p. 274, 1948.

[142] A. Dawson, A. Parkin, S. Parsons, C.R. Pulham and A.L.C. Young," Titanium (IV) chloride at 150 K," *Acta Crystallographica Section E*, **58**, p. i95, 2002.

[143] M. Born and K. Huang, Dynamics theory of crystal lattices, Oxford: Clarendon Press, 1954.

[144] Z.-J. Wu, E.-J. Zhao, H.-P. Xiang, X.-F. Hao, X.-J. Liu and J. Meng, "Crystal structures and elastic properties of superhard IrN_2 and IrN_3 from first principles," *Physical Review B,* **76**, p. 054115, 2007.

[145] J.F. Nye, Physical properties of crystals, Oxford: Clarendon Press, 1985.

[146] S.F. Pugh, "XCII. Relations between the elastic moduli and the plastic properties of polycrystalline pure metals," *Philosophical Magazine,* **45**, p. 823, 1954.

[147] C.-E. Hu, Z.-Y. Zeng, L. Zhang, X.-R. Chen, L.-C. Cai and D. C.-E. Hu, Z.-Y. Zeng, L. Zhang, X.-R. Chen, L.-C. Cai and D. Alfè, "Theoretical investigations of the high pressure structure, lattice dynamics, phase transition, and thermal equation of state of titanium metal," *Journal of Applied Physics,* **107**, p. 093509, 2010.

[148] C. Chapman and M. Sheehan, Catalyst: A framework for success. 2, Oxford: Heinemann Publishers, 2003.

[149] C.F.A. Negre, V.C. Fuertes, M.B. Oviedo and F.Y. Oliva, "Quantum dynamics of light-induced charge injection in a model dye-nanoparticle complex," *Journal of Physical Chemistry C,* **116**, p. 14748, 2012.

[150] S.G. Wang and W.H.E. Schwarz, "Density functional study of first row transition metal dihalides," *The Journal of Chemical Physics,* **109**, p. 7252, 1998.

[151] V.N. Moiseyev, Titanium alloys: Russian aircraft and aerospace applications, Florida: CRC Press, 2005.

[152] M.W. Terban, C. Shi, R. Silbernagel, A. Clearfield and S.J.L. Billinger, "Local environment of terbian (III) ions in layered nanocrystalline zirconium (IV) phosphate-phosphate ion exchange materials," *Inorganic Chemistry,* **56**, p. 8837, 2017.

[153] W.L. Bragg and E.J. Williams, "The effect of thermal agitation on atomic arrangement in alloys," *Proceedings of the Royal Society A,* **145**, p. 699, 1934.

[154] D.K. Jha, Textbook of thermodynamics, New Delhi: Discovery Publishing House, 2004.

[155] P. Perrot, A to Z of thermodynamics, New York: Oxford University Press, 1998.

[156] S.H. Wei, Z. Zeng, J.Q. You, X.H. Yan and X.G. Gong, "A density-functional study of small titanium clusters," *Journal of Chemical Physics,* **113**, p. 11127, 2000.